High Order Fluctuation Splitting Schemes for Hyperbolic Conservation Laws

by

Netsanet Zerihun Mebrate

Submitted in accordance with the requirements
for the degree of Doctor of Philosophy.

The University of Leeds
School of Computing

January 2007

Abstract

This thesis presents the construction, the analysis and the verification of a new form of higher than second order fluctuation splitting discretisation for the solution of steady conservation laws on unstructured meshes. This is an alternative approach to the two existing higher than second order fluctuation splitting schemes, which use submesh reconstruction (developed by Abgrall and Roe) and gradient recovery (developed by Caraeni) to obtain the local higher degree polynomials used to evaluate the fluctuation. The new higher than second order approach constructs the polynomial interpolant of the values of the dependent variables at an appropriate number of carefully chosen mesh nodes.

As they stand, none of the higher than second order methods can guarantee the absence of spurious oscillations from the flow without the application of an additional smoothing stage. The implementation of a technique that removes unphysical oscillations (devised by Hubbard) as part of the new higher than second order approach will be outlined. The design steps and theoretical bases are discussed in depth.

The new higher than second order approach is examined and analysed through application to a series of linear and nonlinear scalar problems, using a pseudo-time-stepping technique to reach steady state solution on two-dimensional structured and unstructured meshes. The results demonstrate its effectiveness in approximating the linear and nonlinear scalar problems.

This thesis also addresses the development and examination of a multistage high order (in space *and* time) fluctuation splitting scheme for two-dimensional unsteady scalar advection on triangular unstructured meshes. The method is similar in philosophy to that of multistep high order (in space *and* time) fluctuation splitting scheme, for the approximation of time-dependent hyperbolic conservation laws. The construction and implementation of the high order multistage time-dependent method are discussed in detail and its performance is illustrated using several standard test problems. The multistage high order time-dependent method is evaluated in the context of existing fluctuation splitting approaches to modelling time-dependent problems and some suggestions for their future development are made. Results presented indicate that the multistage high order method can produce a slightly more accurate solution than the multistep high order method.

Acknowledgements

There are lots of people I would like to thank for a huge variety of reasons.

It is difficult to overstate my gratitude to my PhD supervisor, Dr M. E. Hubbard. I could not have imagined having a better adviser and mentor for my PhD, and without his inspiration, knowledge, perceptiveness and his great efforts to explain things clearly I would have been lost. I owe also my sincere thanks to my second supervisor Prof. P.K. Jimack, for his unstinting commitment to helping see this project through to its final completion, and his equally generous and wise guidance during its development;

The Scientific Computation group within the School of Computing at Leeds have been extremely supportive, and has gone some way towards cementing my faith in academia. I am indebted to D. Hart for managing to read the whole thing so thoroughly and giving me valuable comments. A big thank you to Dr M. A. Walkley, Dr C. E. Goodyer, Dr Dan Liu and Dr G. Romanazzi for those scientific and friendly discussions, which inspired me to become a better scientist. They have also contributed to improve the form of my thesis and I sincerely thank them for that.

This thesis is dedicated to my parents Zerihun and Lemlem, my brothers Abiy and Biruh and my sister Bailsabe, without whom none of this would have been possible. Their endless love, passion and support as well as their sharing in both happiness and sadness have motivated my every effort and inspiration in producing this thesis. It is also dedicated to those who stand up for the truth and make it their business to do so. In remembrance of S.Desalegn and all those who lost their lives. To all the prisoners of conscience since November 1st 2005, imprisoned solely on account of their non-violent opinions and activities, Prof. Mesfin, Dr B. Nega, H. Shawel, B. Mideksa and all the human rights defenders, your sacrifice will not be in vain.

Declarations

Some parts of the work presented in this thesis have been published in the following articles:

M. E. Hubbard and N. Z. Mebrate., "Very High Order, Non-Oscillatory Fluctuation Distribution Schemes", *4th ICCFD conference*, Ghent, Belgium, July 10-14 (2006).

Contents

1 Introduction **1**

1.1 Multidimensional Fluctuation Splitting Schemes 1
1.2 The Fluctuation Splitting Schemes 4
1.3 Contribution 6
1.4 Overview of the Thesis 7

2 Multidimensional Fluctuation Splitting Schemes **10**

2.1 Multidimensional Fluctuation Splitting Schemes 10
2.2 Fluctuation Splitting Framework 10
2.2.1 Linear and Nonlinear Schemes 14
2.2.2 Properties of Fluctuation Splitting Schemes 14
2.3 Finite Volume Schemes 18
2.4 Finite Element Schemes 22
2.5 Fluctuation Splitting Methods 25
2.5.1 The N scheme 25
2.5.2 The LDA Scheme 28
2.5.3 The PSI Scheme 29
2.6 Results 30
2.7 Nonlinear Burgers' equation 32

3 High Order Fluctuation Splitting Schemes **45**

3.1 Introduction 45
3.2 Abgrall-Roe Scheme 46
3.2.1 The Problem 48
3.3 Caraeni's scheme 49
3.4 The Additional Neighbouring Nodes Scheme 50
3.5 Modified Scheme 56
3.5.1 Modified Third Order Abgrall-Roe Scheme 62

3.5.2 Caraeni's Scheme 69
3.5.3 The Positive Additional Neighbouring Nodes Scheme 70
3.6 Burgers' Equation 71
3.7 Results 73
3.7.1 Nonlinear Burgers' Equation 78

4 Fluctuation Splitting Schemes for Unsteady Problems 100
4.1 Fluctuation Splitting Schemes for Unsteady Problems 100
4.2 Space-Time Framework 100
4.3 Petrov-Galerkin Formulation 103
4.4 Dual time-stepping technique 104
4.5 The N scheme 104
4.6 The LDA scheme 106
4.7 The PSI scheme 107
4.8 Multistep Fluctuation Splitting Schemes 107
4.9 Multistage Fluctuation Splitting Schemes 109
4.10 Numerical Results 112

5 Conclusions and Future Prospects 128
5.1 Achievements 129
5.2 Future Prospects 130
5.3 Applications 131

Bibliography 133

List of Figures

2.1 The inward scaled normals. 12
2.2 Median dual cell shaded around vertex i. 13
2.3 One target downstream vertex, denoted by node i_2 16
2.4 Two target downstream vertices, denoted by nodes i_2 and i_3 16
2.5 Upwind finite volume scheme on median dual cell. 19
2.6 The distribution target regions for upwind fluctuation splitting scheme (right), and upwind finite volume scheme (left) : For vector $\vec{\lambda}$ shown, the finite volume is targeted to two vertices i_2 and i_3 while the fluctuation splitting scheme is one-target to vertices i_3. 21
2.7 A three point stencil indicated by filled circle, and outermost points indicated by full circle 26
2.8 Geometry on the N scheme for two target case 27
2.9 The LDA scheme for two positive inflow parameters 28
2.10 A genuinely unstructured triangular mesh, which has 3806 vertices and 7370 cells, used for the advection equation with discontinuous solution and with cosine squared profile on a nonuniform advection field 35
2.11 The mesh type A, which was used for the advection equation with smooth solution (for determining the order of accuracy) on a nonuniform advection field. 36
2.12 The mesh type B, which was used for the advection equation with smooth solution (for determining the order of accuracy) on a nonuniform advection field. 37
2.13 Test case A, solution for N (top), PSI (middle), LDA (bottom) schemes for the square wave case. 38
2.14 Test case B, solution for N (top), PSI (middle), LDA (bottom) schemes for the cosine squared case. 39
2.15 Convergence histories for test cases A (top left), B (top right) and C (bottom), on mesh shown in Figure **??**. 40

2.16 Numerical error for grid type A (left), and for grid type B (right) : L_1 error where the solid line without a marker is slope 2. 41
2.17 Numerical error for grid type A (left), and for grid type B (right) : L_2 error where the solid line without a marker is slope 2. 41
2.18 Numerical error for grid type A (top right), and for grid type B (top left) : L_∞ error where the solid line without a marker is slope 2. 42
2.19 A genuinely unstructured triangular mesh, used for the test case which deals with discontinuous solution for Burgers' equation. 43
2.20 Solutions to the Burgers' equation test case, showing the isolines of the exact (top left) and N (top right), LDA (bottom left) and PSI (bottom right) solutions. 44

3.1 Sub-triangles of p^1 and p^2 interpolation. 47
3.2 Definition of nodes in a high order triangular cell for Caraeni's scheme . . 50
3.3 The nodes over which the high order polynomial representation of the dependent variables will be fitted. 51
3.4 The stencil over which quadratic polynomial will be fitted 52
3.5 The cells that will be added to the stencil at the boundary cell 54
3.6 The additional neighbouring nodes scheme's choice of the closest neighbouring nodes 55
3.7 The limiting procedure for a general case along a cell edge 57
3.8 The limiting procedure for subtriangle reconstruction 65
3.9 The high order reconstruction points of the Abgrall-Roe scheme. 65
3.10 The limiting procedure for Caraeni's scheme gradient recovery 69
3.11 The quadrature points used in integration along each cell edge 71
3.12 The mesh used for the advection results obtained with submesh reconstruction schemes. 79
3.13 Solutions for the Abgrall-Roe scheme applied to the circular advection square wave test case A (top) and cosine squared test case B (bottom). . . 80
3.14 Solution for Caraeni's scheme applied to the circular advection square wave test case A (top) and cosine squared test case B (bottom). 81
3.15 Solution for ANN scheme applied to the circular advection square wave test case A (top) and cosine squared test case B (bottom). 82
3.16 Solutions for the Abgrall-Roe PSI scheme applied to the circular advection square wave test case A (top) and cosine squared test case B (bottom). 83

3.17 Solution for the Caraeni PSI scheme applied to the circular advection square wave test case A (top) and cosine squared test case B (bottom). . . 84
3.18 Solution for ANN PSI scheme applied to the circular advection square wave test case A (top) and cosine squared test case B (bottom). 85
3.19 Test case A, square wave at outflow (top left), zoom around the maximum (top right) and zoom around all the positive high order schemes (bottom). Solid line is exact solution. 86
3.20 Test case B, cosine squared profile at outflow (top left), zoom around the maximum (top right) and zoom around all the positive high order schemes (bottom). Solid line is exact solution. 87
3.21 Test case C, smooth profile at outflow (top left), zoom around the maximum (top right) and zoom around all the positive high order schemes (bottom). Solid line is exact solution. 88
3.22 Numerical error for grid type A (left), and for grid type B (right) : L_1 error where the solid line without a marker is slope 2. 89
3.23 Numerical error for grid type A (left), and for grid type B (right) : L_2 error where the solid line without a marker is slope 2. 89
3.24 Numerical error for grid type A (left), and for grid type B (right) : L_∞ error where the solid line without a marker is slope 2. 90
3.25 Convergence histories for test cases A (top left), B (top right), C (bottom), on meshes shown in Figures **??** and **??**. 91
3.26 Solution for third order ANN PSI scheme (top) and fourth order ANN PSI scheme (bottom) applied to the circular advection square wave test case A. 92
3.27 Solution for third order ANN PSI scheme (top) and fourth order ANN PSI scheme (bottom) applied to cosine squared profile, test case B. 93
3.28 Test case A, square wave at outflow (left), zoom around the maximum (right), for third order and fourth order modified ANN PSI schemes. Solid line is exact solution. 93
3.29 Test case B, cosine squared profile at outflow (left), zoom around the maximum (right), for third order and fourth order modified ANN PSI schemes. Solid line is exact solution. 94
3.30 Test case C, smooth profile at outflow (left), zoom around the maximum (right), for third order and fourth order modified ANN PSI schemes. Solid line is exact solution. 94

3.31 Numerical error for third order and fourth order ANN PSI schemes on grid type A : L_1 error (top left), L_2 error (top right) and L_∞ error (bottom) where the solid line without a marker is slope 3. 95
3.32 A submesh created from a coarser mesh to give a similar number of unknowns as that of genuinely unstructured triangular mesh shown in Figure **??**, and used for the test case which deals with a discontinuous solution for Burgers' equation. 96
3.33 Isolines of the AR scheme (left) and AR PSI scheme (right) solutions. . . 96
3.34 Isolines of the ANN PSI scheme (left) and Caraeni PSI scheme (right) solutions. 97
3.35 Plot of the solutions across the fan, $y = 0.25$, (left) and the zoom around the corner (right). Solid line is exact solution. 97
3.36 Plot of the solutions across the fan, $y = 0.25$, (left) and the zoom around the bottom corner (right). Solid line is exact solution. 98
3.37 Plot of the solutions across the fan, $y = 0.25$, (left) and the zoom around the top corner (right) for the high order positive schemes. Solid line is exact solution. 98
3.38 Plot of the solutions across the shock,$y = 0.75$, (left) and the zoom around the corner (right). Solid line is exact solution. 99
3.39 Plot of the solutions across the shock, $y = 0.75$, (left) and the zoom around the corner (right) for the high order positive schemes. 99

4.1 Prismatic element $\mathscr{P}$. 102
4.2 Space time mesh for prismatic element $\mathscr{P}_\xi$. 108
4.3 The mesh A, used for the rotating advection results. 116
4.4 The mesh B, used for the rotating advection results. 117
4.5 Solution for the rotating cosine hill after one revolution on mesh type A, for exact (top), N (second from top), PSI (third from top) and LDA (bottom) schemes. 118
4.6 Solution for the rotating cosine hill after one revolution on mesh type A, for second order multistep (top), third order multistep (second from top), second order multistage (third from top) and third order multistage (bottom), schemes. 119
4.7 Solution for the rotating cosine hill after one revolution on mesh type B, for Exact (top), N (second from top), PSI (third from top) and LDA (bottom) schemes. 120

4.8 Solution for the rotating cosine hill after one revolution on mesh type B, for second order multistep (top), third order multistep (second from top), second order multistage (third from top) and third order multistage (bottom), schemes. 121
4.9 Solution for the rotating cylinder after one revolution on mesh type A, for N (top), PSI (middle) and LDA (bottom) schemes, where the solid line without a marker is the exact solution. 122
4.10 Solution for the rotating cylinder after one revolution on mesh type A, for second order multistep (top), third order multistep (second from top), second order multistage (third from top) and third order multistage (bottom), schemes. The solid line without a marker is the exact solution. 123
4.11 Solution for the rotating cylinder after one revolution on mesh type B, for N (top), PSI (middle) and LDA (bottom) schemes, where the solid line without a marker is the exact solution. 124
4.12 Solution for the rotating cylinder after one revolution on mesh type B, for second order multistep (top), third order multistep (second from top), second order multistage (third from top) and third order multistage (bottom), schemes. The solid line without a marker is the exact solution. 125
4.13 Numerical error for grid type A (top right), and for grid type B (top left) : for L_1 error. 126
4.14 Numerical error for grid type A (top right), and for grid type B (top left) : for L_2 error. 126
4.15 Numerical error for grid type A (top right), and for grid type B (top left) : for L_∞ error. 127

List of Tables

2.1 Oscillation and accuracy measures. Mesh type A, shown in Figure **??**, was used for accuracy. The finest mesh used has 33153 vertices while the coarsest mesh used has 561 vertices. The genuinely unstructured triangular mesh shown in Figure **??** was used for test cases A and B. 34

2.2 Accuracy measures on grid type B, shown in Figure **??**. 34

3.1 Oscillation and accuracy measures. Mesh type A was used for accuracy. The first two columns have been obtained on the 3806 node and subdivided 984 node meshes shown in Figures **??** and **??** respectively. 74

3.2 Accuracy measures on grid type B. 74

3.3 Accuracy measures on grid type A. 74

4.1 Minimum and maximum solutions for the rotating cosine hill and rotating cylinder test cases, using mesh type A. 115

4.2 Minimum and maximum solutions for the rotating cosine hill and rotating cylinder test cases, using mesh type B. 115

4.3 Accuracy measures for rotating cosine hill, using mesh type A. 116

4.4 Accuracy measures for rotating cosine hill, using mesh type B. 116

Chapter 1

Introduction

1.1 Motivation

The field of computational fluid dynamics has been developing and maturing over the last 35 years, due to the enormous growth in computing power both in speed and memory, coupled with rapid advances in algorithmic efficiency. This growth has enabled a substantially increase in the complexity of the flow configurations that are possible. However, to fully exploit this computational potential, new models are continuously being required to deliver more accurate, efficient, flexible and robust solutions for more and more complex and realistic configurations.

It is widely thought that the use of unstructured grids is preferable for discretising complex geometries and flow patterns compared to structured and multi-block structured grid techniques. This is because structured grids are deemed to be restrictive from the geometrical point of view and a multi-block structured approach takes a lot of time to generate (especially in 3D) [81]. However, the unstructured grid technique not only gives greater flexibility for discretising complex domains, but also enables straightforward implementation of solution-dependent local refinement and adaptation in order to enhance the solution simulation and reduce the number of cells or nodes needed to achieve a specified accuracy [12, 14].

In general the use of unstructured grid techniques and their ability to enhance solution accuracy through adaptive procedures have proved to be such a great advantage that the

design of new numerical algorithms for the simulations of complex flows in complex domains are largely aimed at formulations which are well suited to unstructured grids [13].

The mathematical model for the fluid mechanics equations is given by conservation laws [54]. For example, hyperbolic systems of partial differential equations can be used to model the conservation of some quantities over a given region of space and time. The normal design procedure of fluid flow simulations then begins by studying simple conservation laws, given that one is provided with prior information on the properties of the exact solution. Throughout this thesis, the numerical tests that are used to compare and verify the various numerical schemes are based on simple conservation laws with exact solutions.

Despite the advantages of numerical methods for conservation laws on unstructured grids, the development of efficient and robust unstructured grid algorithms is a considerable ongoing challenge, because the necessity for more accurate, robust and flexible numerical methods for the analysis of complex systems is what pushes forward the construction of new techniques [64]. This effort in developing modern numerical methods also needs to adhere to three main design constraints, namely accuracy, stability and efficiency.

Accuracy

Increasingly accurate approximations are sought using decreasingly expensive reconstruction steps, while at the same time making sure that the scheme is less sensitive to the grid structure. This is specially important for unstructured grids, since they can be highly irregular (particularly in 3D).

Stability

Stability is often associated with conditions that restrict unbounded oscillations. Conservation laws can support weak solutions containing discontinuities, and numerical methods should be able to deal with discontinuities without polluting the solution with unbounded spurious oscillations. Generally, the stability of the method should not depend on some parameter which could be difficult to optimise in a universal way.

Efficiency

Efficiency deals with the simplicity and compactness of the numerical methods, where compactness refers to using information associated with the closest grid en-

tities to compute the values of the unknowns. This generally facilitates for a fast and efficient implementation.

Present day numerical methods on unstructured grids, such as finite volume schemes, have been accepted as some of the most flexible, robust and reliable solution algorithms for the analysis of hyperbolic systems of conservation laws. However, on unstructured grids the modern finite volume schemes for multiple space dimensions are understood to have shortcomings, as they heavily rely on extending their one-dimensional formulation in perpendicular directions to mesh edges (in their two-dimensional formulation) or mesh faces (in three dimensions), which leads to numerical methods which are sensitive to the orientation of the grid [64]. This reliance on the mesh directions often particularly hinders the accuracy of the scheme on unstructured grids. Moreover, the naive interpretation of the physics of the underlying fluid flow misinterprets many multidimensional flow features, which also reduces accuracy as it generates additional numerical dissipation [72]. The attempts to design more accurate multidimensional finite volume schemes, using ENO/WENO techniques [77, 78], and improved high order finite volume schemes on unstructured grids [15] were not able to completely fix these deficiencies.

However, another promising way of developing a genuinely multidimensional numerical method is the fluctuation splitting approach, which builds on the fluctuation-signal formulation of the one-dimensional finite volume method [75] and the residual distribution approach of Ni [59]. The advantage of the fluctuation splitting approach is that it can imitate the evolution of the linearly (or higher degree polynomial) varying solution within each grid cell. In other words, it can reproduce exactly solutions which can be represented exactly by the type of interpolation used for the unknowns on the grid. This makes this method well designed to work on unstructured grids. Moreover, compared to finite volume schemes, fluctuation splitting schemes discard the discontinuous representation of the dependent variable in favour of a continuous, piecewise polynomial approximation which is closer in approach to the finite element schemes [47, 48, 52]. This design gives the fluctuation splitting approach the ability to imitate the evolution of the continuously varying solution.

This close link between the fluctuation splitting schemes and finite element schemes, especially the increasingly popular discontinuous Galerkin approach [23], was initially overlooked, but it has now turned out to be important for development of the fluctuation splitting schemes. In particular, the discontinuous Galerkin finite element scheme uses a stabilisation mechanism based on finite volume-like numerical fluxes, which reduces the residual character (discrete finite element space). Even so, the design of non-oscillatory discontinuous Galerkin finite element schemes uses either the finite volume limiter (which

reduces their accuracy) or discontinuity capturing operators [36, 48]. This does not guarantee local monotonicity and depends on the fine tuning of constants which are difficult to determine naturally. However, fluctuation splitting schemes which are based on representing the dependent variables in a similar way to the finite element scheme, allows the design of nonlinear schemes with a true fluctuation property as well as guaranteeing (by construction) the preservation of the local monotonicity of the approximation.

1.2 The Fluctuation Splitting Schemes

Historically, the fluctuation splitting schemes were introduced in the early eighties by Roe [75], in an upwind context using a reinterpretation of Roe's flux difference splitting finite volume scheme. Roe then continued to develop this approach by generalising the fluctuation splitting scheme in 2D in 1986 [71], to a form initially termed "multidimensional upwind scheme". This ideal of developing discretisations that exploit the multidimensional structure of the governing equations was later discussed extensively in [74], which also helps to clarify the fluctuation splitting schemes' relationship with finite volume and finite element schemes. The close link with finite elements has informed and helped most recent fluctuation splitting developments, for example in the context of time-dependent problems and diffusive fluxes (as in the Navier-stokes equations) [30].

Fluctuation splitting schemes, otherwise referred to as residual distribution schemes, approach the approximation of nonlinear systems of conservation laws on unstructured grids by splitting it into two stages. First, decomposing a conservatively linearised form of each fluctuation into its fundamental components, each having its own special type of signal. Second, distributing these distinct components to the grid nodes [29, 64, 65, 83]. This approach gives the fluctuation splitting scheme flexibility in propagating the discrete signals in any direction over the grid, making it a genuinely multidimensional upwind method. This quality has also been proved to allow higher accuracy than finite volume schemes of similar order [69]. For steady state problems, the methods are now being applied in industry [30], as relatively accurate and robust varieties of the fluctuation splitting schemes now exist. Generally, second order accurate methods at steady state are deemed accurate enough for simulating complex flows in the presence of discontinuities, without introducing unphysical oscillations into the flow. The so-called PSI scheme [32] is the most commonly used second order accurate fluctuation splitting scheme at steady state, being both positive (to prohibit unphysical oscillations) and linearity preserving (for accuracy). This scheme will differ from the N scheme due to the distribution of the simplified components, which is the second stage of the fluctuation splitting scheme.

More recently, the construction of fluctuation splitting schemes which are higher than second order accurate for both steady and time-dependent problems has received more focus by researchers. This is mainly because, for the steady state problem, simple experiments on scalar advection show that the strong performance of the very high order schemes in being able to reduce the error, compensates for the complexity that is involved in obtaining the very high order approximation [82]. For time-dependent problems, the approximation of the discrete forms of both spatial and temporal derivative terms requires very high order accuracy, so that the overall degree of accuracy is maintained over a long time [3, 6, 27].

For time-dependent simulations, fluctuation splitting schemes are still an expanding research topic, even though real progress has been seen in the last few years. The main framework for the construction of higher than first order accurate fluctuation splitting schemes was started by observing the equivalence of fluctuation splitting schemes to the mass-lumped Petrov-Galerkin finite element formulation [22, 56]. This is mainly because in their basic formulation fluctuation splitting schemes cannot be more than first order accurate in time-dependent computation, due to an inconsistency in the spatial discretisation of the time derivative term. However, high order accuracy in time can be obtained using a consistent mass matrix [6, 68], which has proved to be successful in the construction of second order accurate scheme.

For the achievement of higher than second order accuracy, Caraeni and Fuchs presented a new approach in which the time derivative is consistently included in the definition of the fluctuation [17, 19, 21, 57]. They did this by creating a quadratic representation within each grid cell using local gradient reconstruction of the dependent variable at the grid nodes, which can be found easily from the surrounding data. Another alternative, developed by Abgrall and Roe [8] and Andrianov and Mezine [3, 4], uses additional nodes created by uniformly subdividing the global grid to store and update the values of the dependent variables before distributing it to the resulting subtriangles.

However, the above approaches were found to be non-positive from the various numerical experiments that were undertaken and these results were further substantiated by the theoretical investigation that was carried out [41]. This meant that unphysical oscillations occur in regions where the solution gradient changes rapidly, and for time-dependent simulation even schemes which are positive at steady state, lose that property when the time derivative is integrated consistently in space. Moreover, these shortcomings are further complicated when one considers nonlinear systems [17]. Subsequently, a new technique was devised for the steady state problems by Hubbard [41], which imposes positivity on the above two higher than second order schemes for steady state problems, and has been

shown to achieve a positive and linearity preserving scheme with higher than second order accuracy.

1.3 Contribution

The research carried out in this project deals with the construction of new numerical algorithms within the fluctuation splitting framework and applying them to scalar equations, based on which a more complicated computational method for complex fluid flow can be built. The contributions and new developments that are presented are based on three key elements.

1. The development of a new, higher than second order fluctuation splitting scheme, which uses additional neighbouring nodes. Currently there are two types of methods that achieve higher than second order fluctuation splitting schemes, as mentioned in Section 1.2, employing submesh reconstruction [8] and gradient recovery [17] to obtain higher degree polynomials, which are then used to construct the fluctuation. The new additional neighbouring nodes fluctuation splitting scheme constructs the high order fluctuation by using extra information about the dependent variables stored at neighbouring nodes in addition to the regular cell nodes. The additional grid nodes are chosen by carefully picking an appropriate number of nodes from the immediate neighbouring cells, to construct the polynomial interpolant of the values at the dependent variables. The solution is then stored and updated at the regular cell nodes with the distribution of the fluctuation carried out on the regular cells. The advantage of using the additional neighbouring nodes fluctuation splitting scheme over submesh reconstruction is that it requires less storage. It also avoids the complexity involved in approximating solution gradients to higher order accuracy on structured or unstructured grids.

2. The very high order fluctuation splitting scheme presented by Abgrall and Roe [8], was found to be not positive from the various numerical experiments that were undertaken and these results were further substantiated by the theoretical investigation that was carried out by Hubbard [41]. These findings also indicated the source of the non-positivity of the very high order scheme as well as raising the need for constructing a very high order scheme that would combine both positivity and linearity preservation properties. In the same paper a method for imposing positivity on existing high order schemes was presented, providing a framework for imposing

positivity on the additional neighbouring nodes fluctuation splitting scheme. In this thesis a positive additional neighbouring nodes scheme will be constructed.

3. The development of a multistage time-dependent fluctuation splitting scheme. This work is concerned with the construction of a high order (in space *and* time) fluctuation splitting scheme for two-dimensional unsteady scalar advection on triangular meshes. The method has been developed as a complement to the high order discretisation of the steady state by Abgrall and Roe [8], and the unsteady high order multistep space-time discretisation of Abgrall, Andrianov and Mezine [3]. The construction of this technique was carried out by combining a positive Runge-Kutta time-stepping [79] for the time derivative with a continuous piecewise quadratic representation of the dependent variable which, when combined, lead to a high order space-time fluctuation. A low order (N scheme) space-time fluctuation is used to assist in stabilising the solution by combining it with the high order (Abgrall-Roe scheme) fluctuation within each stage of the Runge-Kutta method to reduce the occurrence of unphysical oscillations. The performance of this method has been illustrated using several standard test problems. The advantage of the multistage fluctuation splitting scheme over the multistep fluctuation splitting scheme [3], is that it does not require the storage of additional information at previous time levels and it is not as difficult to preserve the positivity of the spatial discretisation [41].

1.4 Overview of the Thesis

The organisation of this thesis starts by going through the existing fluctuation splitting methods, pointing out the contributions and new developments in the fluctuation splitting framework. The contributions of this research work will be outlined, and various tests and comparisons of existing and new fluctuation splitting schemes will be discussed. Since the first introduction of fluctuation splitting schemes, they have been proved to be accurate and robust enough to give a real alternative to finite volume [25, 81] and finite element schemes [5] for the computation of both steady and unsteady flows on unstructured meshes. Chapter 2 deals with the concepts of fluctuation splitting schemes, and the design criteria to be satisfied by the advection schemes, i.e. continuity, positivity, linearity preservation, multidimensional upwinding, conservation and compactness. It will show the close link between fluctuation splitting schemes and upwind finite volume schemes, as well as Petrov-Galerkin finite element schemes. It will also describe two linear schemes, the N scheme which satisfies positivity at the expense of high order accuracy, the LDA

scheme which satisfy linearity preservation at the expense of spurious oscillations near discontinuities. Finally the nonlinear PSI scheme, which satisfies both positivity and linearity preservation, is presented.

Chapter 3 discusses the very high order fluctuation splitting scheme presented by Abgrall and Roe [8], and outlines the theoretical reasons why this approach cannot guarantee the absence of spurious oscillations from the flow. This chapter will also discuss in detail the new approach devised by Hubbard [41] which showed how to achieve a positive and linearity preserving higher than second order fluctuation splitting scheme. The scheme which has been developed is based on acquiring an exact limited very high order cell fluctuation and distributing this to the appropriate vertices of the cell, as determined by comparing the distribution coefficients of the limited very high order scheme and those of the N scheme [32]. It will also be shown that encouraging results have been obtained for simple steady state advection problems and for Burgers' equation.

The methods that form the basis of this approach are the Abgrall-Roe scheme, which uses submesh reconstruction [8], and Caraeni's method, which uses gradient recovery [17] to obtain the high degree polynomials that will be used to evaluate the fluctuation. A third new alternative approach which will give higher than second order accuracy at steady state, called the additional neighbouring nodes scheme will also form the basis of the above approach and will also be presented in this chapter. This new addition to the existing two high order fluctuation splitting schemes is one of the new contributions of this thesis and offers an alternative approach to constructing the polynomial from the values of the dependent variables at an appropriate number of carefully chosen grid nodes. The high order fluctuations are then calculated using the extra information about the dependent variables stored at the neighbouring nodes in addition to the regular cell nodes. These values are then stored and updated at the regular cell nodes using the distribution of the fluctuation carried out on the regular cells.

The numerical experiments undertaken on the scalar advection equation clearly showed the advantage of using the very high order schemes compared to the PSI scheme, which is only second order [32, 81]. This is mainly because of the strong performance of the very high order schemes in being able to reduce the unphysical errors, and this characteristic being able to provide a counterbalance to the complexity that is involved in obtaining the very high order approximation [8].

Chapter 4 is concerned with the construction of a multistage high order (in space *and* time) fluctuation splitting scheme for two-dimensional unsteady scalar advection on triangular meshes. The method has been constructed as a complement to the high order discretisation of the steady state by Abgrall and Roe [8], and the unsteady high order

multistep space-time discretisation of Abgrall, Andrianov and Mezine [3].

This chapter will begin by outlining the space-time framework and the design properties to be satisfied by the different schemes. The description of the space-time variants of the N, PSI and LDA schemes, as well as the construction steps of the higher than second order multistep method will also be presented. The implementation of the multistage method, which is also a new contribution of this thesis, will be discussed in detail and some illustrative computational examples and analysis will be given at the end.

Chapter 5 summarises the research presented and its main achievements by recalling the results and ideas presented. Moreover, the way forward together with some possible routes and ideas for extending and improving the work presented will also be outlined.

Chapter 2

Multidimensional Fluctuation Splitting Schemes

2.1 Introduction

In this chapter the fluctuation splitting schemes which are the subject of this work will be introduced. A clear definition for this approach will be given as well as showing the close link between the fluctuation splitting schemes and both the upwind finite volume and finite element schemes. Currently the fluctuation splitting approach for simulating complex steady state fluid flow are judged to give a real alternative to both finite volume and finite element schemes [64]. Illustrative numerical examples are given at the end of this chapter to experimentally show the difference between the various fluctuation splitting schemes that will be presented.

2.2 Fluctuation Splitting Framework

Many partial differential equation models with a physical motivation derive from conservation laws. This philosophy of the physical theory is rooted in the understanding that quantities (such as charge, energy, momentum etc) are conserved. In general a conservation law is simply the mathematical formulation of the basic fact that the rate at which a quantity (u) changes in a given domain must equal the rate at which the quantity flows into

or out of the domain plus the rate at which the quantity is created or destroyed within the domain. This thesis considers the numerical approximation of solutions to the following conservation law

$$\frac{\partial u}{\partial t} + \nabla \cdot \vec{f} = 0 \, , \tag{2.1}$$

One of the most common partial differential equations, which models the transport of a substance that is present in very small concentrations within the fluid is the advection equation. It is generally used to model transport of the conserved quantity through the domain [11]. Assuming the domain contains no sources and that the conserved quantity is being transported by some velocity (e.g. dust particles carried by wind, chemical concentration carried by fluid motion, boats drifting downstream etc) it is possible to introduce a constitutive law relating the flux and that quantity

$$\vec{f} = u \, \vec{\lambda} \, , \tag{2.2}$$

where $\vec{\lambda}$ is the advection velocity carrying quantity (u) through the domain. Substituting the advection constitutive equation (2.2) into the conservation law (2.1) to obtain

$$\frac{\partial u}{\partial t} + \nabla \cdot (u \, \vec{\lambda}) = 0 \, , \tag{2.3}$$

and now applying the product rule it is possible to expand (2.3), to obtain the general advection equation

$$\frac{\partial u}{\partial t} + u \, \nabla \cdot \vec{\lambda} + \vec{\lambda} \cdot \nabla u = 0 \, . \tag{2.4}$$

One common assumption to be made is that the velocity field is constant everywhere in the domain which leads to $\nabla \cdot \vec{\lambda} = 0$. Another common assumption that could be made is for incompressible flows, which is expressed mathematically by the constraint $\nabla \cdot \vec{\lambda} = 0$, because in this case the velocity field may vary spatially but the divergence of the velocity is zero everywhere. In these cases equation (2.4) simplifies to

$$\frac{\partial u}{\partial t} + \vec{\lambda} \cdot \nabla u = 0 \, . \tag{2.5}$$

This is called the advection equation form of the conservation law and the approximation of this scalar advection equation on an unstructured discretisation of the space-time domain $\Omega \times [0,t]$ can be done using fluctuation splitting schemes. Ω is the spatial domain and $\vec{\lambda}$ is the appropriate advection velocity associated with the conservation law.

Fluctuation splitting schemes use a continuous piecewise polynomial representation

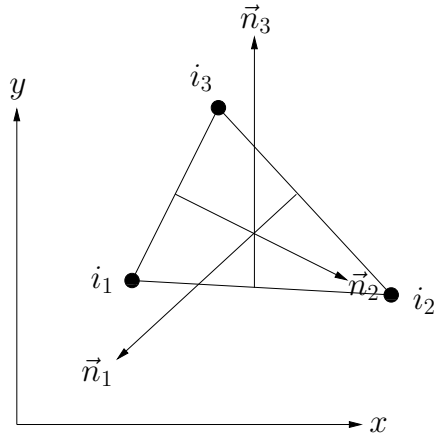

Figure 2.1: The inward scaled normals.

of the solution variables, and the methods are designed to imitate the evolution of the polynomial varying solution within each grid cell [32, 65]. The high accuracy and genuinely multidimensional characteristics of the fluctuation splitting schemes make them very efficient when compared to the finite volume schemes [25]. Compared to finite element schemes, fluctuation splitting schemes give increased reliability because they lead to parameter-free non-oscillatory schemes [27]. Moreover, they are also able to take advantage of the geometric flexibility enjoyed by unstructured grid methods [32].

The fluctuation associated with the scalar advection equation (2.5), is a cell based quantity which is given by

$$\phi^T = -\int_\Omega \vec{\nabla}\cdot\vec{f}^h \,\mathrm{d}\Omega = -\int_\Omega \vec{\lambda}\cdot\nabla u \,\mathrm{d}\Omega = \oint_{\partial\Omega} u\vec{\lambda}\cdot\vec{n}\,\mathrm{d}\Gamma \tag{2.6}$$

where $\vec{f}^h$ is a continuous interpolant of the flux $\vec{f}$, a function of the solution variable u, and T represents a triangular mesh cell. The basic steps in applying the fluctuation splitting schemes are as follows :

1. Evaluate the fluctuation ϕ^T using an conservative linearisation [32], so that the integration in Equation (2.6) is carried out exactly, giving

$$\phi^T = -S_T\widetilde{\vec{\lambda}}\cdot\nabla u = -\sum_{l=1}^{3} k_l u_l \;, \qquad k_l = \frac{1}{d}\widetilde{\vec{\lambda}}\cdot\vec{n}_l \;, \tag{2.7}$$

   where $\vec{n}_l$ is the inward pointing normal scaled by the length of the edge l of the cell, as depicted in Figure 2.1, and k_l is called the inflow parameter for a d-dimensional space, in which $\widetilde{\ }$ depicts an appropriately linearised quantity and S_T is the cell area.

2. Distribute the appropriate amount of ϕ^T to each vertex of the cell. If ϕ_i^T is used to

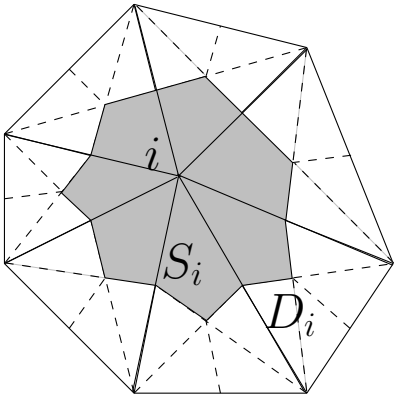

Figure 2.2: Median dual cell shaded around vertex i.

denote the contribution of the fluctuation to node $i \in T$, then by construction, these must satisfy

$$\sum_{i \in T} \phi_i^T = \phi^T \tag{2.8}$$

for conservation. The distribution coefficients β_i^T determine the appropriate proportion of the fluctuation ϕ^T to be sent from cell T to node i, and are given by

$$\beta_i^T = \phi_i^T / \phi^T \ . \tag{2.9}$$

Conservation is therefore achieved as long as

$$\sum_{i \in T} \beta_i^T = 1 \ , \tag{2.10}$$

i.e., the whole of each fluctuation is sent to the nodes within a cell. This ensures that the local fluctuations satisfy (2.8).

3. Gather the contributions of the elements at the vertices and use an appropriate time integration, e.g. a forward Euler discretisation of the time derivative, which gives an iterative update of the nodal solution values of the form

$$u_i^{n+1} = u_i^n - \frac{\Delta t}{S_i} \sum_{T \in \cup D_i} \beta_i^T \phi^T \ . \tag{2.11}$$

where Δt is the time-step and S_i is the median dual cell area around node i, one third of the total area of the triangles having i as a vertex, see Figure 2.2.

For solving steady state problems, the time derivative term is included as a scheme for

iterating to the steady state. However, for dealing with time dependent problems, the time derivative term is necessary and it must be integrated in a manner which is consistent with the underlying representation of u if the order of accuracy for the steady state approach is to be maintained [3]. This will be explained further in Chapter 3.

2.2.1 Linear and Nonlinear Schemes

In order to identify and define the two subclasses of linear schemes, substitute (2.7) in to (2.11) to obtain

$$u_i^{n+1} = u_i^n - \frac{\Delta t}{S_i} \sum_T \beta_i^T \left(\sum_{j=1}^{3} k_j u_j^n \right) . \tag{2.12}$$

It follows that one can write the scheme as

$$u_i^{n+1} = \sum_{l \in D_i} c_l u_l^n , \tag{2.13}$$

with $\sum_l c_l = 1$ required for consistency. Two classes of schemes can be defined from the above scheme: linear schemes, for which c_l are independent of u, and nonlinear schemes, for which c_l depend on u.

Moreover the linear schemes can be subdivided into two subclasses using (2.12). One can have a linear scheme with distribution coefficient β_i^T independent of u, or it is also possible to have a linear scheme for which $\phi_i^T = \beta_i^T \phi^T$ is linear in u or depend on u and $\beta_i^T \propto \frac{1}{\phi^T}$. This definition will be very helpful in identifying the various fluctuation splitting schemes that will be presented in this chapter.

2.2.2 Properties of Fluctuation Splitting Schemes

The different schemes, corresponding to different ways of computing the distribution coefficients used in (2.11), have been designed to satisfy several properties. These design criteria are positivity, continuity, linearity preservation, multidimensional upwinding, conservation and compactness.

Positivity

The positivity property guarantees that there are no numerical oscillations, by ensuring that the scheme satisfies a maximum principle which prohibits the occurrence of new extrema in the solution [32, 65, 81]. A scheme of the form (2.13) is globally positive when

$$c_l \geq 0, \ \ \forall l \ . \tag{2.14}$$

This guarantees that every solution value at the new time level $(n+1)$ can be written as a convex combination of the values at the old time level. This ensures that the resulting scheme can capture discontinuities like shocks and slip lines without undershoots and overshoots. In general this property ensures that no extrema are created, since

$$\min_l u_l^n \leq \sum_l c_l u_l^n \leq \max_l u_l^n \ . \tag{2.15}$$

Requiring that the condition (2.14) is obeyed for each particular cell, is known as the local positivity condition. This condition will also be grid independent making it easy to impose.

Continuity

The continuity of a scheme is required to obtain a smooth convergence to the steady state solution [32, 65]. A scheme is continuous if the contributions to the nodes, $\beta_i^T \phi^T$, depend continuously on both the solution u and the advection velocity $\vec{\lambda}$. Discontinuous schemes introduce switches which hamper convergence towards steady state solutions, a behaviour known as limit cycling [32]. This is because the contributions to the nodes discontinuously change from one iteration to the next. Therefore it is desirable that the contributions to the nodes using the distribution coefficients β_i^T are continuous functions in both the advection and solution gradient directions.

Linearity Preservation

The ability of a numerical scheme to reproduce exactly at least a linearly varying solution is called linearity preservation [46, 65, 81]. This condition requires that, for an arbitrary triangular mesh, the scheme preserves the exact steady state solution when this is a linear function of the space coordinates. The test for this property is done by using an explicit scheme of the form (2.11), which will be linearity preserving if and only if, for any triangle T, the coefficients β_i^T are bounded as ϕ^T tends to zero [32].

A relaxed version of this property avoids defining the distribution coefficients explicitly [9]. For example, to get second order accuracy at steady state, the local

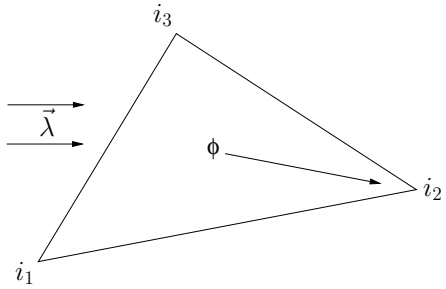

Figure 2.3: One target downstream vertex, denoted by node i_2

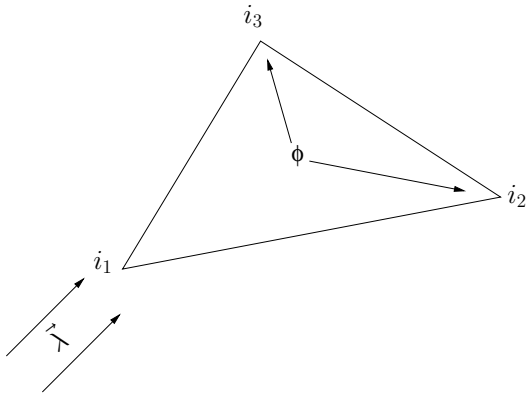

Figure 2.4: Two target downstream vertices, denoted by nodes i_2 and i_3

fluctuations, ϕ_i^T are required to satisfy the property [9]

$$\phi_i^T(u^h) = O(h^3) \tag{2.16}$$

where u^h is a piecewise polynomial interpolant on the mesh and h is the maximum diameter of the triangles T. It is now possible to see that the total fluctuation evaluated for u^h satisfies

$$\phi^T = O(h^3) \tag{2.17}$$

so that the boundedness of $\beta_i^T = \frac{\phi_i^T}{\phi^T}$ is true for (2.16). This is an alternative way of ensuring the linearity preservation condition to asking the boundedness of β_i^T's. It is worth noting that linearity preservation and positivity are incompatible for linear schemes according to Godunov's theorem [38], which states that a linear scheme of the form (2.13) cannot be both locally positive and linearity preserving.

Multidimensional Upwinding

The multidimensional upwind design property is one which ensures that the fluctuation is distributed only to the downstream vertices of the cell according to the

direction of the flow velocity. There are two possible combinations of inflow and outflow faces of a triangular cell for scalar advection in two dimensions. These correspond to one inflow face, as shown in Figure 2.3, and two inflow faces, shown in Figure 2.4. In general, the multidimensional upwind property will be satisfied if

$$\beta_l^T = 0 \qquad if \qquad k_l \leq 0, \tag{2.18}$$

which means that nothing will be distributed to the upstream nodes; all the fluctuation will be distributed to the downstream nodes, as illustrated in Figures 2.3 and 2.4. Here the inward scaled normals satisfy

$$\vec{n}_{i_1} + \vec{n}_{i_2} + \vec{n}_{i_3} = 0 \ , \tag{2.19}$$

and, as a consequence, the inflow parameters $k_i = \frac{1}{2}\vec{\lambda} \cdot \vec{n}_i$ satisfy

$$k_{i_1} + k_{i_2} + k_{i_3} = 0 \ . \tag{2.20}$$

Now looking at Figures 2.3 and 2.4, it is possible to explain (2.18). For the one inflow case, it is obvious as only one of the inflow parameters k_i is positive. This means that $k_{i_2} > 0$ and k_{i_1}, $k_{i_3} \leq 0$ so $\phi_{i_2}^T = \phi^T$ and $\phi_{i_1}^T = \phi_{i_3}^T = 0$. For two target triangles, two of the k_i's are positive, i.e. k_{i_2},$k_{i_3} > 0$ and $k_{i_1} \leq 0$, which means that the fluctuation must be split between the two downstream nodes i_2 and i_3. Overall the multidimensional upwind scheme minimises the amount of crosswind diffusion within the class of upwind schemes and consequently gives an accurate result if the flow is not aligned with the grid [81].

Conservation As already mentioned in (2.10), conservation is ensured by making sure that the whole fluctuation is distributed to the nodes of the mesh [32]. As a consequence this property guarantees correct discontinuity capturing.

Compactness Computations are performed on each vertex using only its direct neighbours. For a given grid point i in Figure 2.2, the stencil only contains the vertices of all the neighbouring triangles with shared vertex i. Such compactness is ensured by restricting the distribution of the fluctuation to within its cell. This property is an aid for a fast and efficient implementation and easy parallelisation [31, 32].

2.3 Finite Volume Schemes

Finite volume schemes are techniques which are obtained from a direct discretisation of a system of conservation laws written in integral form. This method can be defined on an arbitrary mesh, and a large number of options are available for the definition of the control volumes (an arbitrary spatial region) on which the conservation laws are expressed and the subsequent evaluation of the fluxes through the control surface (the boundaries of the control volume). The fluxes are approximated by means of a numerical flux function, which could be obtained from the approximate cell averages or by a suitable reconstruction including neighbouring cell averages as well. In addition, by direct discretisation of the integral form of the conservation laws, the method ensures that the basic quantities conserved at the analytical level remain conserved at the discrete level. This is an essential attribute for compressible fluid flow, since the correct approximation of a discontinuous solution can only be obtained by using this principle [12, 15]. It is possible to show the correspondence between any finite volume scheme which is based on the median dual cells [12, 15, 16, 28, 54, 84], and some fluctuation splitting schemes. The analysis below follows that of [2], to show that the first order upwind finite volume scheme on the median dual grid could be formulated as a fluctuation splitting scheme. For the scalar conservation law (2.3), consider a fluctuation in a triangle T, which is equivalent to the integral representing the flux balance over the triangle, which can be defined as

$$\phi^T = \int_T \nabla \cdot \vec{f} \, \mathrm{d}\Omega = - \oint_{\partial T} \vec{f} \cdot \vec{n} \, \mathrm{d}\Gamma \, , \tag{2.21}$$

where the flux vector for linear convection case can be expressed as $\vec{f} = \vec{\lambda} u$, thanks to the consistency property of the upwind finite volume flux, and $\vec{n}$ is the inward pointing normal to the cell boundary. Now consider the numerical flux function $H(u_L, u_R, \vec{n})$, corresponding to the first order upwind differencing which can be written as

$$H(u_L, u_R, \vec{n}) = \frac{\vec{f}(u_R) \cdot \vec{n} + \vec{f}(u_L) \cdot \vec{n}}{2} - \frac{1}{2} \left| \left(\frac{\partial \vec{f}}{\partial u} \right)_{\bar{u}} \cdot \vec{n} \right| (u_R - u_L). \tag{2.22}$$

where $\bar{u}$ is an average state between u_L and u_R, satisfying

$$\left(\frac{\partial \vec{f}}{\partial u} \right)_{\bar{u}} (u_R - u_L) = \vec{f}(u_R) - \vec{f}(u_L) \, , \tag{2.23}$$

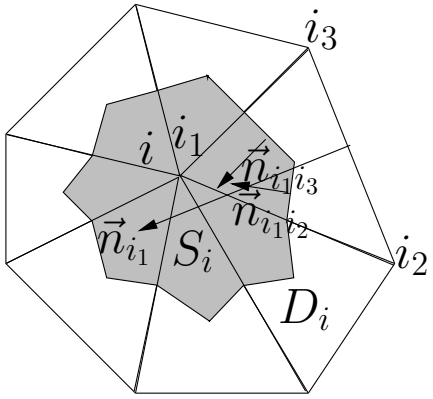

Figure 2.5: Upwind finite volume scheme on median dual cell.

Now, using the fact that $\frac{1}{2}(z-|z|) = min(z,0)$, for an arbitrary z, with the flux vector, already defined as $\vec{f} = \vec{\lambda}u$, it is possible to express the numerical flux function (2.22) as

$$\begin{aligned} H(u_L,u_R,\vec{n}) &= \frac{1}{2}((\vec{\lambda}\cdot\vec{n})u_R + (\vec{\lambda}\cdot\vec{n})u_L) - \frac{1}{2}\left|\left(\frac{\vec{\lambda}u_R - \vec{\lambda}u_L}{(u_R-u_L)}\right)\cdot\vec{n}\right|(u_R-u_L) \\ &= \frac{1}{2}\left(\vec{\lambda}\cdot\vec{n}(u_R) + \vec{\lambda}\cdot\vec{n}(u_L) - \left|\vec{\lambda}\cdot\vec{n}\right|(u_R-u_L)\right) \\ &= \vec{\lambda}\cdot\vec{n}(u_L) + \frac{1}{2}\vec{\lambda}\cdot\vec{n}(u_R-u_L) - \frac{1}{2}\left|\vec{\lambda}\cdot\vec{n}\right|(u_R-u_L) \\ &= \vec{\lambda}\cdot\vec{n}(u_L) + \frac{1}{2}\left(\vec{\lambda}\cdot\vec{n} - \left|\vec{\lambda}\cdot\vec{n}\right|\right)(u_R-u_L) \\ &= \vec{\lambda}\cdot\vec{n}(u_L) + \min(\vec{\lambda}\cdot\vec{n},0)(u_R-u_L) \\ &= \vec{\lambda}\cdot\vec{n}(u_L) + (\vec{\lambda}\cdot\vec{n})^-(u_R-u_L)\ . \end{aligned} \tag{2.24}$$

Hence, the upwind finite volume semidiscrete equation associated with node i becomes (see Figure 2.5)

$$S_i\frac{du_i}{dt} = \oint_{\partial S_i}\vec{f}\cdot\vec{n}\,\mathrm{d}\Gamma = -\sum_{T\in D_i}\left[H(u^n_{i_1},u^n_{i_2},\vec{n}_{i_1 i_2}) + H(u^n_{i_1},u^n_{i_3},\vec{n}_{i_1 i_3})\right]\ , \tag{2.25}$$

when summing over all the cells in D_i (see Figure 2.5). Substituting (2.24) in to (2.25) finally allows the upwind finite volume scheme to be defined by the split fluctuation [66]

$$
\begin{aligned}
S_i \frac{u_i^{n+1}-u_i^n}{\Delta t} &= -\sum_{T\in D_i}\left[(\vec{\lambda}\cdot\vec{n}_{i_1i_2}+\vec{\lambda}\cdot\vec{n}_{i_1i_3})u_{i_1}^n+(\vec{\lambda}\cdot\vec{n}_{i_1i_2})^-(u_{i_2}^n-u_{i_1}^n)+(\vec{\lambda}\cdot\vec{n}_{i_1i_3})^-(u_{i_3}^n-u_{i_1}^n)\right] \\
&= -\sum_{T\in D_i}\left[(\vec{\lambda}\cdot\vec{n}_{i_1i_2})^-(u_{i_2}^n-u_{i_1}^n)+(\vec{\lambda}\cdot\vec{n}_{i_1i_3})^-(u_{i_3}^n-u_{i_1}^n)\right] \\
&= -\sum_{T\in D_i}\left[(K_{i_1i_2})^-(u_{i_2}^n-u_{i_1}^n)+(K_{i_1i_3})^-(u_{i_3}^n-u_{i_1}^n)\right] \\
&= -\sum_{T\in D_i}\beta_i^{FV}\phi^T \qquad (2.26)
\end{aligned}
$$

because $\sum_{T\in D_i}(\vec{n}_{i_1i_2}+\vec{n}_{i_1i_3})=0$. For this expression to become equivalent to that of a fluctuation splitting scheme, one has to recall the definition of the fluctuation in a triangle T (2.21)

$$
\begin{aligned}
\phi^T &= \frac{1}{2}\left(\vec{f}(u_{i_2}^n)+\vec{f}(u_{i_3}^n)\right)\cdot\vec{n}_{i_1}+\frac{1}{2}\left(\vec{f}(u_{i_1}^n)+\vec{f}(u_{i_3}^n)\right)\cdot\vec{n}_{i_2}+\frac{1}{2}\left(\vec{f}(u_{i_1}^n)+\vec{f}(u_{i_2}^n)\right)\cdot\vec{n}_{i_3} \\
&= \left(\vec{\lambda}u_{i_2}^n+\vec{\lambda}u_{i_3}^n\right)\cdot(\vec{n}_{i_1i_2}+\vec{n}_{i_1i_3})+\left(\vec{\lambda}u_{i_1}^n+\vec{\lambda}u_{i_3}^n\right)\cdot(-\vec{n}_{i_1i_2}+\vec{n}_{i_2i_3}) \qquad (2.27) \\
&+ \left(\vec{\lambda}u_{i_1}^n+\vec{\lambda}u_{i_2}^n\right)\cdot(-\vec{n}_{i_1i_3}-\vec{n}_{i_2i_3}) \\
&= (\vec{\lambda}\cdot\vec{n}_{i_1i_2})[u_{i_2}^n-u_{i_1}^n]+(\vec{\lambda}\cdot\vec{n}_{i_1i_3})[u_{i_3}^n-u_{i_1}^n]+(\vec{\lambda}\cdot\vec{n}_{i_2i_3})[u_{i_3}^n-u_{i_2}^n] \qquad (2.28)
\end{aligned}
$$

because $\vec{n}_{i_1i_2}+\vec{n}_{i_1i_3}=\frac{1}{2}\vec{n}_{i_1}$, as shown in Figure 2.5, with similar expressions derived for $\vec{n}_{i_2}$ and $\vec{n}_{i_3}$. Having in mind the distribution coefficient definition (2.9) for fluctuation splitting schemes, if each term is taken separately in the above equation, for example looking at the flux in the direction $\vec{n}_{i_1i_2}$ it is possible to construct an upwind scheme by formulating the distribution to node i_1 or i_2, by looking at the sign of $\vec{\lambda}\cdot\vec{n}_{i_1i_2}$. This leads to a distribution coefficient,

$$\beta_{i_1}^{FV}=\frac{1}{\phi^T}\sum_{i_l\neq i_1}(\vec{\lambda}\cdot\vec{n}_{i_1i_l})^-(u_{i_l}^n-u_{i_1}^n)\ . \qquad (2.29)$$

It is possible to see that (2.26) is formulated as fluctuation splitting scheme (2.11)

$$\beta_{i_1}^{FV}=\phi_i^T/\phi^T\ , \qquad (2.30)$$

which finally leads to the upwind finite volume - fluctuation splitting scheme defined by the split fluctuations [66]

$$\phi_{i_l}^T = \sum_{i_l \neq i_1} (\vec{\lambda} \cdot \vec{n}_{i_1 i_l})^- (u_{i_l}^n - u_{i_1}^n). \tag{2.31}$$

Moreover the scheme will be positive for (2.26), if the nodal time restriction reads

$$\Delta t \leq \frac{S_{i_1}}{-(K_{i_1 i_2})^- - (K_{i_1 i_3})^-}. \tag{2.32}$$

This is more constraining than most of the fluctuation splitting schemes which will be discussed later in this chapter. Another of the shortcomings of the finite volume scheme is the fact that it is not a multidimensional upwind scheme as defined in Section 2.2.2, so it lacks one of the major advantages of fluctuation splitting schemes over flux-based methods. This general statement becomes clear when one looks at Figure 2.6, showing the distribution target regions for the velocity $\vec{\lambda}$. When the fluctuation splitting scheme is one target to vertex i_3 for the velocity $\vec{\lambda}$ drawn in the figure, the upwind finite volume is two target to vertices i_2 and i_3, making it more diffusive [66], as the distribution is not restricted to the downstream vertex only, compared to the one target distribution by the upwind fluctuation splitting scheme. For varying $\vec{\lambda}$ in general, the upwind finite volume scheme is always two target except when the velocity $\vec{\lambda}$ is pointing to the vertex and is in alignment with one of the medians of the triangle which point towards the vertex from which the median originates from. However, the upwind nature of the fluctuation splitting scheme, indicated by the shaded regions, is defined by the edges as outlined in (2.18). It determines the distribution targets by the signs of the inflow parameters k_{i_1}, k_{i_2} and k_{i_3} respectively.

Overall it is possible to see that the upwind finite volume scheme operating on median dual cells with numerical flux function of the type (2.22) can be recast into a fluctuation splitting formalism.

2.4 Finite Element Schemes

Finite element schemes are variational based techniques for solving partial differential equations [40, 76]. They are a technique in which a given domain is represented as a collection of simple sub-domains, called finite elements, on which it is possible to systematically construct the approximation functions needed in a variational or weighted residual approximation of the solution to a problem. In this method, the approximation

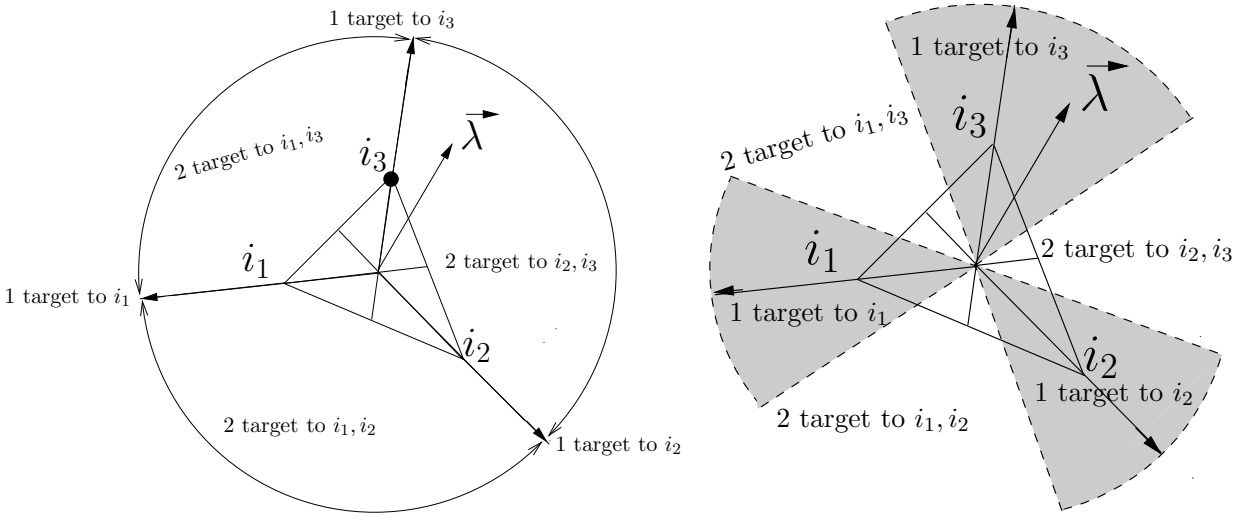

Figure 2.6: The distribution target regions for upwind fluctuation splitting scheme (right), and upwind finite volume scheme (left) : For vector $\vec{\lambda}$ shown, the finite volume is targeted to two vertices i_2 and i_3 while the fluctuation splitting scheme is one-target to vertices i_3.

functions are typically piecewise polynomials.

The basic components in developing the finite element model are as follows [40].

1. Weak formulation of the differential equation over an element.

2. Finite element interpolation of the primary variables of the weak formulation.

3. Finite element formulation over a typical element.

The weak formulation itself involves a three step procedure, which in general cases allows the definition of an equivalent integral formulation, involving the identification of primary variables (i.e. variables that are required to be continuous throughout the domain, including the nodes at which cells are connected). The finite element model interpolation functions are developed on the basis of continuity, completeness, and linear independence. The finite element method is devised by substituting appropriate interpolations of the primary variable into the weak form of the differential equation.

The analysis below follows that of [22,30,35,45,65], to equate the fluctuation splitting schemes with mass-lumped Petrov-Galerkin and Galerkin finite element schemes. The fluctuation splitting scheme is linked with the Galerkin finite element scheme [30] in the context of central schemes obtained by distributing the fluctuation to the nodes of a cell equally. On the other hand the fluctuation splitting scheme can also have equivalence with Petrov-Galerkin finite element schemes [36, 47–50, 52], if the weight functions are designed to satisfy some of the properties outlined earlier in this chapter [30, 34]. The weighting function will be associated with node i of cell T denoted here by ω_i^T.

First, consider the Petrov-Galerkin finite element scheme for steady advection equation (2.5), for which the discretisation can be written as

$$\sum_T \int_T \omega_i^T \vec{\lambda} \cdot \nabla u^h \, \mathrm{d}\Omega \; = \; 0 \, , \tag{2.33}$$

where u^h is a piecewise linear solution representation. From (2.5) it is possible to define ϕ^T as

$$\phi^T = \Omega_T \vec{\lambda} \cdot \nabla u^h \, , \tag{2.34}$$

where Ω_T is the area of the triangle T. This is because, for constant advection velocity and the linear approximation of u^h, $\vec{\lambda} \cdot \nabla u^h$ will be constant over T and equate to $\frac{\phi^T}{\Omega_T}$. For reasons that will become clear later in this section, the Galerkin scheme can be written as

$$\sum_T \frac{1}{3} \phi^T \; = \; 0. \tag{2.35}$$

This is equivalent to a steady state approximation of the advection equation with a linearity preserving fluctuation splitting scheme, with distribution coefficients

$$\beta_{i_1}^T = \frac{1}{3} \, . \tag{2.36}$$

For constant advection speed it is just a centred fluctuation splitting scheme and equivalent to the Galerkin finite element scheme. Now, to support this claim let us look at how (2.35) was obtained by simplifying (2.33) given (2.34). For constant advection velocity $\vec{\lambda}$ and $\vec{\lambda} \cdot \nabla u^h$ constant over T, (2.33) gives

$$\sum_T \int_T \omega_i^T \, \mathrm{d}\Omega \, \frac{\phi^T}{\Omega_T} \; = \; 0 \, . \tag{2.37}$$

Note that this only holds in the constant coefficient case, and in general the fluctuation splitting and Galerkin finite element schemes give different discrete equations, because the integrals (2.33) do not reduce to (2.37) all the time. However for Galerkin and Petrov-Galerkin discretisations to be equivalent to the fluctuation splitting discretisation (2.8), the weighting function ω_i^T must satisfy

$$\int_T \omega_i^T \, \mathrm{d}\Omega = \; \beta_i^T \Omega_T \, . \tag{2.38}$$

Now by substituting (2.38) in to (2.37)

$$\sum_{T \in \cup D_i} \beta_i^T \ \phi^T \ = \ 0, \tag{2.39}$$

it is possible to see that the fluctuation splitting scheme reduces to a pure Galerkin finite element scheme, for equidistribution of the fluctuation over all vertices of the cell (2.35).

It is now very useful to gain more understanding of the association between the weighting function ω_i^T and the distribution coefficient β_i^T, by defining the weight function. In order to do this, it is appropriate to write the solution in finite element terms, assuming a continuous numerical approximation of u in space and given $\{u_i(t) = u(x_i, y_i, t)\}_{i \in T}$

$$u^h(x,y,t) = \sum_{i \in T} \psi_i(x,y) u_i(t) \ . \tag{2.40}$$

where ψ_{i_1} denotes the continuous nodal basis function. To define the relation between the weighting function ω_i^T and the basis function ψ_i, an SUPG-like weight function [59, 63] is chosen

$$\omega_i^T = \psi_i + \alpha_i^T \gamma^T \ . \tag{2.41}$$

where α_i^T is the upwind bias coefficient contribution of cell T to node i and γ^T is the piecewise constant function equal to 1 on cell T and 0 elsewhere. Substituting this in to the previous equation (2.38) gives

$$\frac{1}{\Omega_T} \int_T \psi_i + \alpha_i^T \ \mathrm{d}\Omega = \ \beta_i^T, \tag{2.42}$$

and hence

$$\beta_i^T = \frac{1}{d+1} + \alpha_i^T \ , \tag{2.43}$$

where d denotes a d-dimensional space. Using the above equation and (2.41), it is possible to associate the weighting function ω_i^T with the distribution coefficient β_i^T,

$$\omega_i^T = \psi_i + \left(\beta_i^T - \frac{1}{d+1} \right) \gamma^T \ . \tag{2.44}$$

From the above equation it is clear to see that the Galerkin finite element scheme with the weighting functions identical to the nodal basis functions $(\psi_i = \omega_i)$ and $\gamma^T = 1$, and for equidistribution of the fluctuation over all vertices of the cell leads to a distribution coefficient $\beta_i^T = \frac{1}{d+1}$ outlined in (2.36) for two dimensions , which is nothing else but the centred fluctuation splitting scheme given in (2.35). On the other hand, because Petrov-Galerkin finite element schemes don't have identical weighting and nodal basis

functions, their distribution coefficients and weighting functions have the more general forms given in (2.42) and (2.44). Moreover because of this relation, it is sometimes possible to view fluctuation splitting schemes as a particular class of Petrov-Galerkin finite element scheme, giving this approach a different viewpoint to the discontinuous model used in the finite volume method.

2.5 Fluctuation Splitting Methods

2.5.1 The N scheme

The linear positive N scheme, designed by Roe [71] for solving the advection equation, is the most successful first order scheme, and currently forms the principal component in the construction of linearity preserving, nonlinear, positive discretisations. This scheme is a first order fluctuation splitting formulation of the positive multidimensional upwind method which gives the lowest numerical dissipation among first order schemes [46, 62, 71, 81]. In two dimensions the triangular mesh cells do not always have a unique (only one target) downstream node so an alternative, two target, distribution must be devised, as shown in Figure 2.4. If a mesh cell does have a one target downstream node, then a single target distribution will be used.

In the one target case in two dimensions, the whole fluctuation is distributed to a single downstream vertex, as illustrated in Figure 2.3. This locally satisfies the positivity, upwind, conservation and linearity preservation property, making it an appropriate choice in these situations [32]. In order to show this, assume node i_2 is the downstream vertex, as in Figure 2.3, so that from (2.7) and (2.11) the local update takes the form

$$S_{i_2} u_{i_2}^{n+1} = S_{i_2} u_{i_2}^n - \Delta t (k_{i_1} u_{i_1}^n + k_{i_2} u_{i_2}^n + k_{i_3} u_{i_3}^n) \tag{2.45}$$

where Δt is the time-step. u_{i_1} and u_{i_3} are left unchanged by the activity within this cell. This scheme is positive if $S_{i_2} - k_{i_2}\Delta t \geq 0$, which is true as long as $\Delta t < \frac{S_{i_2}}{k_{i_2}}$. The distribution is optimal, in the sense that it allows the largest possible time-step as well as satisfying positivity. It is also linearity preserving since the distribution coefficients ($\beta_{i_1}^T = 0, \beta_{i_2}^T = 1$ and $\beta_{i_3}^T = 0$) are independent of the data, so it preserves the exact steady state solution when this is piecewise linear in space [32]. Conservation is automatically guaranteed as $\sum_{j\in T} \beta_j^T = 1$, and it is upwind because $\beta_{i_1}^T$, $\beta_{i_3}^T = 0$, for k_{i_1}, $k_3 < 0$, which means that nothing is distributed to the downstream nodes. Note that for the one target case in two dimensions all the fluctuation splitting schemes are identical.

In the two target case the N scheme differs from the other fluctuation splitting schemes

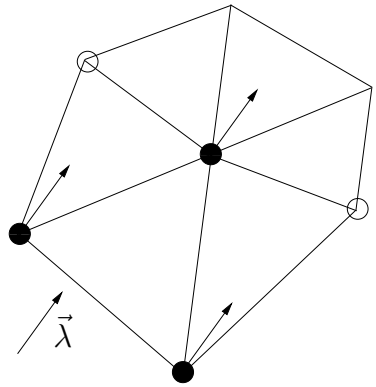

Figure 2.7: A three point stencil indicated by filled circle, and outermost points indicated by full circle

(defined later in this chapter) in its distribution coefficients. Since the N scheme is required to be positive, it cannot be linearity preserving because it is linear, according to Godunov's theorem [32, 46]. In order to show this assume, as in Figure 2.4, that the two inflow sides are given by k_{i_2},$k_{i_3} \geq 0$. No contribution will be sent to the upstream vertex because of the upwind condition, i.e.

$$\beta_{i_1}^T = 0 \qquad \text{and} \qquad \beta_{i_2}^T + \beta_{i_3}^T = 1 \; . \tag{2.46}$$

The scheme for the local update reads

$$\begin{aligned} S_{i_1} u_{i_1}^{n+1} &= S_{i_1} u_{i_1}^n \\ S_{i_2} u_{i_2}^{n+1} &= S_{i_2} u_{i_2}^n - \Delta t k_{i_2} (u_{i_2}^n - u_{i_1}^n) \\ S_{i_3} u_{i_3}^{n+1} &= S_{i_3} u_{i_3}^n - \Delta t k_{i_3} (u_{i_3}^n - u_{i_1}^n) \end{aligned} \tag{2.47}$$

This is a locally positive scheme as long as the time-step satisfies [32]

$$\Delta t \leq \min \left(\frac{S_{i_2}}{k_{i_2}}, \frac{S_{i_3}}{k_{i_3}} \right) \; . \tag{2.48}$$

Note that this is less restrictive than the constraint mentioned in Section 2.3, (2.32) for the upwind finite volume scheme because

$$\Delta t \leq \frac{S_{i_1}}{-(K_{i_1 i_2})^- - (K_{i_1 i_3})^-} \leq \frac{S_{i_1}}{k_{i_1}} \; , \tag{2.49}$$

where $K_l = \vec{\lambda} \cdot \vec{n}_l$, and $k_l = \frac{1}{d} \vec{\lambda} \cdot \vec{n}_l$. Condition (2.48) ensures local positivity, as it is derived using only the contribution of a single triangle, and it is slightly more restrictive than necessary when the overall nodal scheme is considered. This means that a less restrictive

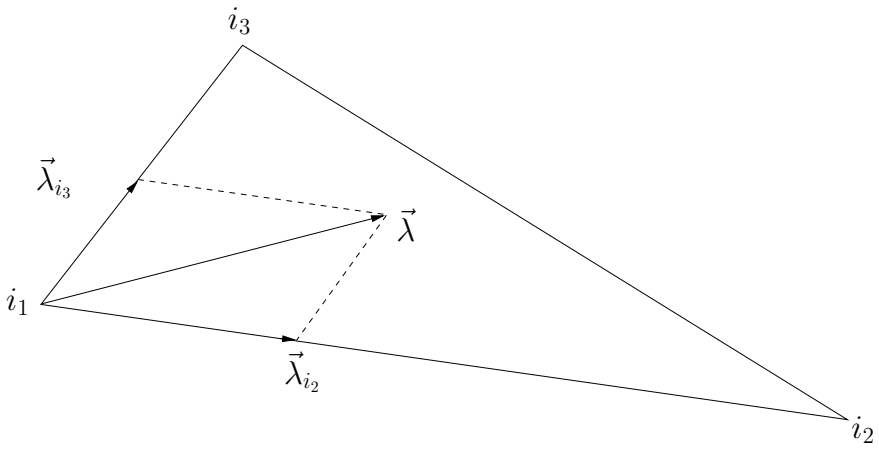

Figure 2.8: Geometry on the N scheme for two target case

condition for positivity can be used to obtain the limit on the time-step. For the scheme in (2.45) and (2.47) positivity can be based on the nodal update (2.11), so the time-step restriction at node i becomes [32, 81]

$$\Delta t \leq \frac{S_i}{\sum_T \max(0, k_i^T)} \,. \tag{2.50}$$

This can be shown to be the largest possible time-step for which a linear fluctuation splitting scheme can be positive. Another reason to call (2.45) and (2.47) the optimal positive scheme is that it has the most narrow stencil, hence its name, the Narrow (N) scheme. This was achieved by eliminating the contribution from the outermost points of the stencil, as shown in Figure 2.7.

The fluctuation distribution for the N scheme can be understood by considering the velocity $\vec{\lambda}$ to be decomposed, as shown in Figure 2.8, into the sum of components parallel to edges $i_1 i_2$ and $i_1 i_3$ so that,

$$\vec{\lambda} = \vec{\lambda}_{i_2} + \vec{\lambda}_{i_3} \,. \tag{2.51}$$

Given k_l, defined in (2.7), the fluctuation due to $\vec{\lambda}_{i_2}$ can be shown to be

$$\begin{aligned}
\phi_{i_2}^N &= -\frac{1}{2}(\vec{\lambda}_{i_2} \cdot \vec{n}_{i_2})(u_{i_2}^n - u_{i_1}^n) - \frac{1}{2}(\vec{\lambda}_{i_2} \cdot \vec{n}_{i_3})(u_{i_3}^n - u_{i_1}^n) \\
&= -\frac{1}{2}(\vec{\lambda}_{i_2} \cdot \vec{n}_{i_2})(u_{i_2}^n - u_{i_1}^n) \\
&= -\frac{1}{2}(\vec{\lambda} \cdot \vec{n}_{i_2})(u_{i_2}^n - u_{i_1}^n) \\
&= -k_{i_2}(u_{i_2}^n - u_{i_1}^n)
\end{aligned} \tag{2.52}$$

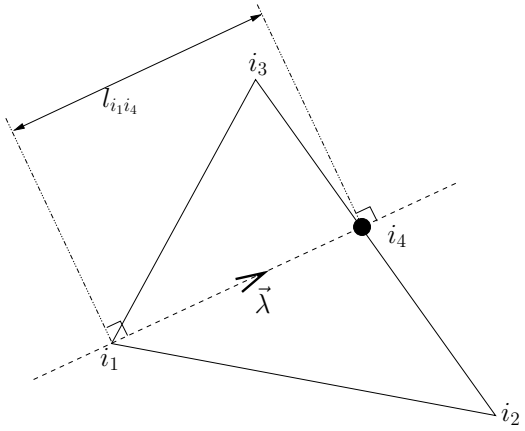

Figure 2.9: The LDA scheme for two positive inflow parameters

because $\vec{\lambda}_{i_2} \cdot \vec{n}_{i_3} = 0$, i.e. for $\vec{\lambda}_{i_2}$ only edge $\overline{i_1 i_3}$ is an inflow side. The second velocity component leads to

$$\phi_{i_3}^N = -k_{i_3}(u_{i_3}^n - u_{i_1}^n) \; . \tag{2.53}$$

Now, the two target N scheme (2.47) sends the whole of the fluctuation due to $\vec{\lambda}_{i_2}$ to vertex i_{i_2} and that of $\vec{\lambda}_{i_3}$ to vertex i_{i_3}, thereby reducing to upwind along the inflow edges of the cell.

2.5.2 The LDA Scheme

The LDA (Low Diffusion A) scheme satisfies linearity preservation at the price of spurious oscillations near discontinuities and other sharp changes in solution gradient [32]. As with the N scheme, the LDA scheme satisfies positivity, upwind, conservation and linearity preservation property for one inflow side triangles as shown in Figure 2.3, because it uses the same distribution as (2.45). However for two inflow side triangles the schemes differ. The geometrical interpretation of this scheme is shown in Figure 2.9 where it is assumed that k_{i_2} and k_{i_3} are both positive and k_{i_1} is negative. Its distribution coefficients are given by

$$\beta_{i_2}^{LDA} = \frac{k_{i_2}}{k_{i_2} + k_{i_3}} = \frac{|T_{i_4 i_3 i_1}|}{|T|}, \qquad \beta_{i_3}^{LDA} = \frac{k_{i_3}}{k_{i_1} + k_{i_2}} = \frac{|T_{i_2 i_4 i_1}|}{|T|} \; . \tag{2.54}$$

where

$$|T_{i_4i_3i_1}| = \frac{l_{i_1i_4}k_{i_2}}{||\vec{\lambda}||}, \quad |T_{i_2i_4i_1}| = \frac{l_{i_1i_4}k_{i_3}}{||\vec{\lambda}||}, \qquad \text{and} \quad |T| = |T_{i_4i_3i_1}| + |T_{i_2i_4i_1}|\,, \tag{2.55}$$

$|T_{i_4i_3i_1}|$ and $|T_{i_2i_4i_1}|$ are the areas of the sub-triangle $T_{i_4i_3i_1}$ and $T_{i_2i_4i_1}$. Consequently $|T|$ is the total area of T, and can also be written as

$$|T| = \frac{l_{i_1i_4}(k_{i_2} + k_{i_3})}{||\vec{\lambda}||}. \tag{2.56}$$

It is now possible to write a general distribution coefficient by substituting (2.56) and (2.55) in to (2.54), giving

$$\beta_i^{LDA} = \frac{k_i^+}{\sum_{j\in T} k_j^+} \tag{2.57}$$

where k^+ refers to the positive part of k. Note that if only one inflow parameter k_i is positive, the LDA and the N scheme are identical. However, if two inflow parameters are positive, the schemes differ.

2.5.3 The PSI Scheme

The nonlinear PSI (Positive Streamwise Invariant) scheme is one of the most successful fluctuation splitting schemes constructed. This is because of its positivity and linearity preserving properties as well as its compactness [66]. The name Positive Streamwise Invariant refers to the fact that it was designed to enforce invariance of the solution along streamlines when each and every cell is considered individually. The PSI scheme can be obtained from the N scheme using a form of limiter (usually minmod limiter) [4, 8, 46, 62, 65]. The philosophy behind this scheme is to only apply the limiter to the two target case, as indicated in Figure 2.4, because in the one target case the N scheme contributions are both positive and linearity preserving. The two target PSI scheme satisfies all of the properties outlined in Section 2.2.2. The linearity preservation is obtained by limiting the distribution coefficients of the N scheme. The PSI scheme's distribution coefficients can be written as

$$\beta_i^{PSI} = \frac{(\beta_i^N)^+}{\sum_{j\in T}(\beta_j^N)^+}\,, \tag{2.58}$$

where $()^+$ denotes the positive part of the distribution coefficient within the bracket, and

$$\beta_i^N = \frac{\phi_i^N}{\phi^T} \ . \tag{2.59}$$

Here ϕ_i^N refers to the contribution made by the cell to node i by the N scheme and ϕ^T is the cell fluctuation, from expressions (2.52) and (2.53). Linearity preservation is guaranteed because $\beta_i^{PSI} \in [0,1]$ is bounded. This gives zero cross diffusion on a triangular grid. The PSI scheme is also globally positive; it automatically inherits this property from the N scheme because $|\beta_i^{PSI}| \leq |\beta_i^N|$.

2.6 Results

A genuinely unstructured triangular mesh, which has 3806 vertices and 7370 cells, shown in Figure 2.10, is used to obtain the results shown in Figures 2.13 and 2.14. Uniform structured triangular meshes, like the ones shown in Figures 2.11 and 2.12, are used to provide errors for the advection problem which will be shown below. Starting from the finest mesh to the coarsest, the meshes used have 525825, 131841, 33153, 8385, 2145 and 561 vertices. To obtain solutions to the inviscid Burgers' equation a genuinely unstructured triangular mesh, which has 1926 vertices and 3690 cells, shown in Figure 2.19, will be used.

Test case A

First consider a problem which will be referred to as test case A. The initial equation is given as

$$x\frac{\partial u}{\partial x} - y\frac{\partial u}{\partial x} = 0 \qquad\qquad (x,y) \in [-1,1] \times [0,1] \ . \tag{2.60}$$

This problem models a steady state clockwise circular advection around the point $(0,0)$, with velocity, $\vec{\lambda} = (y,-x)^T$. The initial profile is given as

$$u(x,0) = \begin{cases} 0 & \text{if } x \notin [0.35, 0.65] \\ 1 & \text{if } x \in [0.35, 0.65] \ . \end{cases} \tag{2.61}$$

The genuinely unstructured triangular mesh shown in Figure 2.10 is used to obtain all the results for this test case. This test case is appropriate for illustrating the positivity of the scheme. The result for this test case are shown in Figure 2.13. In the figure the N scheme is shown to have a significant level of numerical diffusion,

while the PSI scheme is shows a significant improvement over the N scheme. For the PSI scheme there are still no oscillations and much less numerical diffusion. The LDA scheme is shown to have a significant amount of oscillation which is visible at the discontinuities. All the schemes converge quickly to steady state as shown in Figure 2.15. The convergence monitor which was used is the root mean square (RMS) of the fluctuation of the solution, at each time step given as

$$RMS = \sqrt{\frac{\sum_{i=1}^{N_n}(u_i^{n+1} - u_i^n)}{N_n}} \tag{2.62}$$

Test case B

Now consider a problem which will be referred to as test case B. The initial profile is given as

$$u(x,0) = \begin{cases} 0 & \text{if } x \notin [0.35, 0.65] \\ \cos^2 \frac{10\pi(x+1/2)}{3} & \text{if } x \in [0.35, 0.65] \end{cases} \tag{2.63}$$

and it uses exactly the same genuinely unstructured triangular mesh as in the previous test case A, with the same steady state clockwise circular advection, around the point $(0,0)$, with velocity $\vec{\lambda} = (y, -x)^T$. Test case B is appropriate for determining the scheme's ability to maintain a smooth peak without artificially steepening the profile. All the schemes converge to the steady state as shown in Figure 2.15. The results for this test case are shown in Figure 2.14. The N scheme can be seen to have a significant level of numerical diffusion, but it does not show any sign of oscillation. The same figure shows that the PSI scheme, gives an improvement in accuracy over the N scheme, because of its nonlinear positive and linearity preserving property, while also giving a smooth profile. The LDA scheme, also shown in the same figure, shows some oscillation visible at the outflow boundary in correspondence with its non-positive property.

Test case C

Now consider a problem which will be referred to as test case C, which uses exactly the same velocity field but with smoother solution profile, given as

$$u(x,0) = \begin{cases} G(x) & \text{for } -0.75 \leq x \leq -0.25 \\ 0 & \text{otherwise} \end{cases} \tag{2.64}$$

in which

$$G(x) = \begin{cases} g(4x+3) & \text{if } -0.75 \leq x \leq -0.5 \\ g(-4x-1) & \text{if } -0.5 \leq x \leq -0.25 \end{cases} \tag{2.65}$$

where

$$g(x) = x^5(70x^4 - 315x^3 + 540x^2 - 420x + 126)\ . \tag{2.66}$$

This test case is appropriate for determining the order of accuracy of the schemes in the presence of turning points, because the exact solution to this problem, $u(x,y) = G(r)$ for $0.25 \leq r = \sqrt{x^2+y^2} \leq 0.75$, with zero elsewhere, has continuous fourth derivative. A series of uniform structured triangular meshes like the ones shown in Figures 2.11 and 2.12, were used to provide errors for the advection problem given above. Starting from the finest mesh to the coarsest, the meshes used have 33153, 8385, 2145 and 561 vertices.

All the oscillation and accuracy measures are outlined in Table 2.1 and Figures 2.16, 2.17 and 2.18 for mesh type A, as well as Table 2.2 and Figures 2.16, 2.17 and 2.18 for mesh type B. For the N and PSI schemes, the measured order of accuracy reported in the tables are within the standard and expected values for all the schemes presented. However, the LDA scheme clearly exhibits higher than second order accuracy for the smooth test case. That was not expected, even though the LDA scheme is a linearity preserving scheme which gives it high accuracy. The PSI scheme gives a slope between 1.8 and 2, which is what is normally measured on a uniform structured mesh for a nonlinear positive and linearity preserving scheme. The N scheme give a slope which is slightly under one, as it does not satisfy linearity preservation, which is essential to obtaining a high order of accuracy. In general, very similar conclusions have been obtained by looking at the L_1 and L_2 errors. It's also possible to see the accuracy improve as the mesh is refined for L_∞ norm. For all the accuracy results, grid type A gives a slightly better accuracy than grid type B, maybe because the grid is well suited to represent the solution because of the angle present (connectivity is favourably inclined) in the cell edges of the mesh, especially in the outflow half.

2.7 Nonlinear Burgers' equation

A two-dimensional variant of Burgers' equation, used here to exemplify a nonlinear equation, is given as

$$\frac{\partial u}{\partial t}+\frac{\partial}{\partial x}\left(\frac{u^2}{2}\right)+\frac{\partial u}{\partial y}=0 \qquad \text{or} \qquad \frac{\partial u}{\partial t}+\vec{\nabla}\cdot\vec{f}=0 \tag{2.67}$$

where $\vec{f}=(\frac{u^2}{2},u)^T$. From the linearisation given in [46,61], it is possible to write the local advection velocity as, $\widetilde{\vec{\lambda}}=(\overline{u},1)^T$, where $\overline{u}$ is the average of the values of the variable u at the vertices of the cell. This test case will be used for a nonlinear conservation law to simulate a discontinuous solution. The mesh structure which is used is a genuinely unstructured triangular mesh, shown in Figure 2.19, on the domain $(x,y)\in[0,1]^2$. The boundary conditions used are

$$\begin{aligned} u(x,0)&=1.5-2x, && 0\le x\le 1\\ u(0,y)&=1.5, && 0\le y\le 1\\ u(1,y)&=-0.5, && 0\le y\le 1\ . \end{aligned} \tag{2.68}$$

The exact solution is given as

$$u(x,y)=\begin{cases} -0.5 & \text{if } y\le 0.5 \text{ and } -2(x-\frac{3}{4})+y-\frac{1}{2}\le 0\\ 1.5 & \text{if } y\le 0.5 \text{ and } -2(x-\frac{3}{4})+y-\frac{1}{2}\ge 0\\ \max\left(-0.5,\min\left(1.5,\frac{x-\frac{3}{4}}{y-\frac{1}{2}}\right)\right) & \text{otherwise .}\end{cases} \tag{2.69}$$

A genuinely unstructured triangular mesh, with 1926 vertices and 3690 cells, shown in Figure 2.19, is used to obtain all the results shown in Figure 2.20. The exact solution will be compared with the various solutions obtained using the different schemes outlined previously.

From Figure 2.20 it is possible to see that the N scheme is less accurate than the others in the region where the characteristics intersect. This is because the N scheme is not linearity preserving. The results for the LDA scheme, which is linearity preserving, shown in the same figure, illustrate that the shock is captured sharply. The PSI scheme for which the results are shown in the same figure, resolves the shock in a better way than the N and LDA schemes, because it is a second order scheme as well as positive. The LDA scheme also produce comparable isolines and resolves the linear part of the solution well.

Schemes	Test Case A	Test Case B	Test Case C		
	min (u)	max (u)	L_1 order	L_2 order	L_∞ order
N	0.00	0.58	0.92	0.85	0.76
LDA	-0.14	0.98	2.35	2.17	1.31
PSI	0.00	0.78	1.91	1.79	1.83

Table 2.1: Oscillation and accuracy measures. Mesh type A, shown in Figure 2.11, was used for accuracy. The finest mesh used has 33153 vertices while the coarsest mesh used has 561 vertices. The genuinely unstructured triangular mesh shown in Figure 2.10 was used for test cases A and B.

Schemes	Test Case C		
	L_1 order	L_2 order	L_∞ order
N	0.89	0.83	0.72
LDA	2.29	2.16	1.29
PSI	1.91	1.78	1.82

Table 2.2: Accuracy measures on grid type B, shown in Figure 2.12.

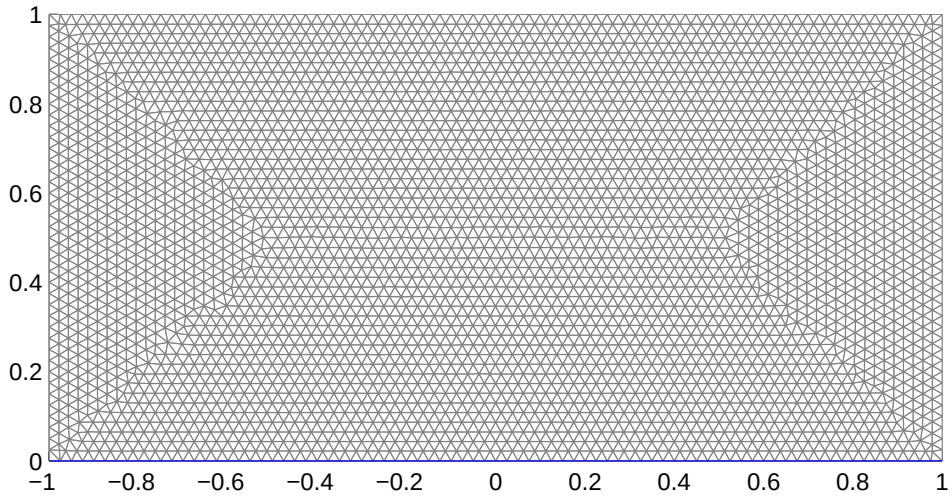

Figure 2.10: A genuinely unstructured triangular mesh, which has 3806 vertices and 7370 cells, used for the advection equation with discontinuous solution and with cosine squared profile on a nonuniform advection field

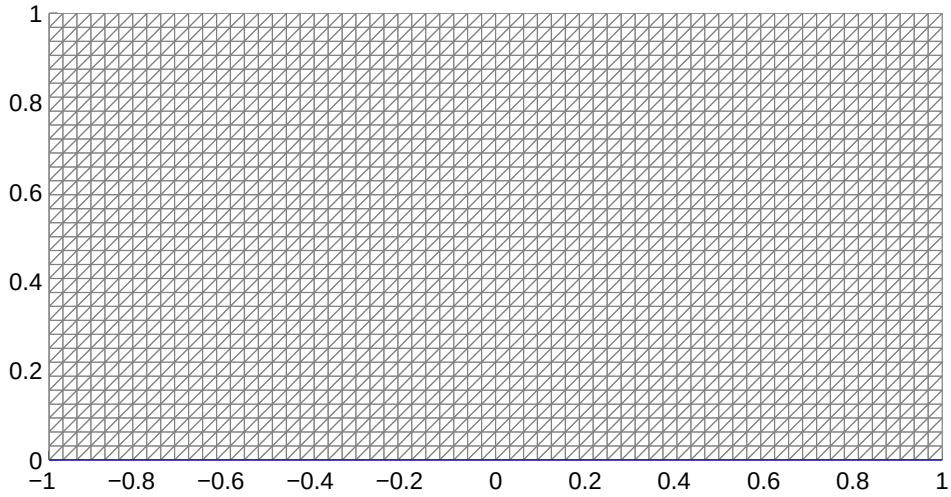

Figure 2.11: The mesh type A, which was used for the advection equation with smooth solution (for determining the order of accuracy) on a nonuniform advection field.

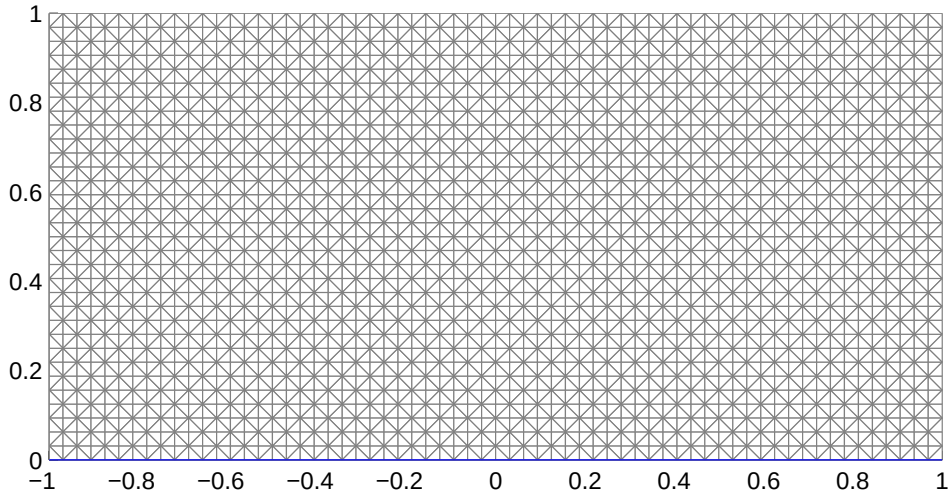

Figure 2.12: The mesh type B, which was used for the advection equation with smooth solution (for determining the order of accuracy) on a nonuniform advection field.

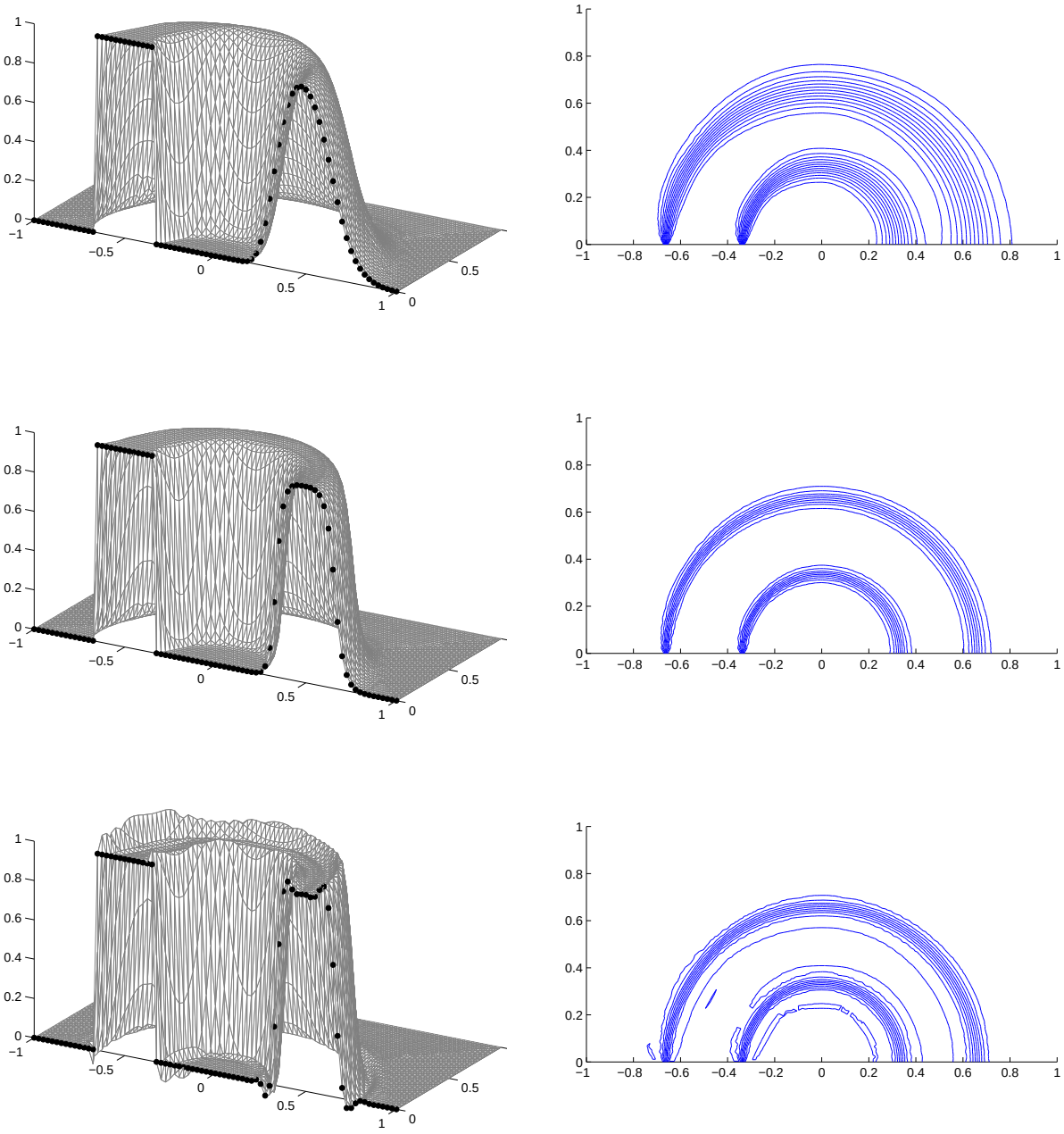

Figure 2.13: Test case A, solution for N (top), PSI (middle), LDA (bottom) schemes for the square wave case.

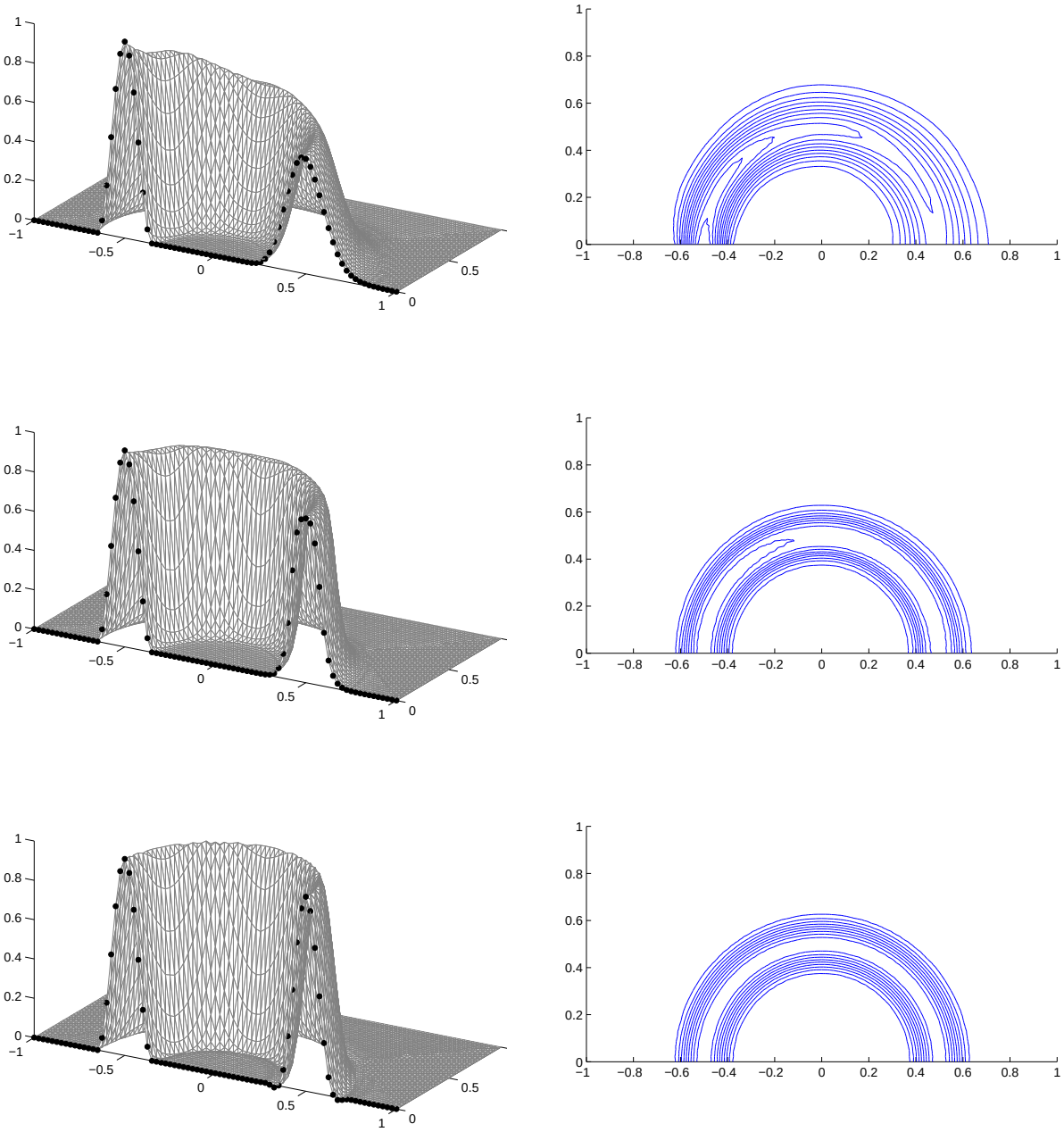

Figure 2.14: Test case B, solution for N (top), PSI (middle), LDA (bottom) schemes for the cosine squared case.

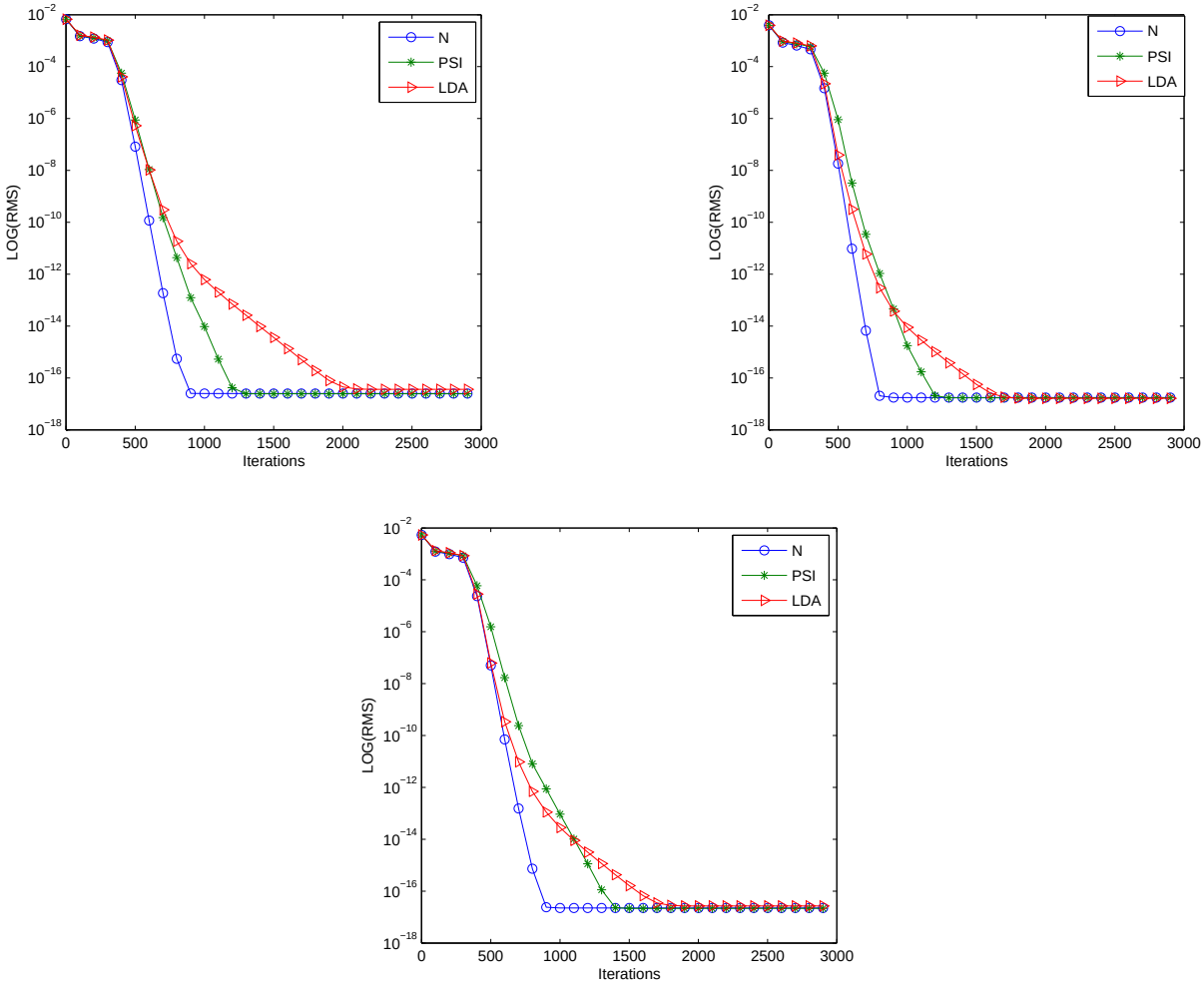

Figure 2.15: Convergence histories for test cases A (top left), B (top right) and C (bottom), on mesh shown in Figure 2.19.

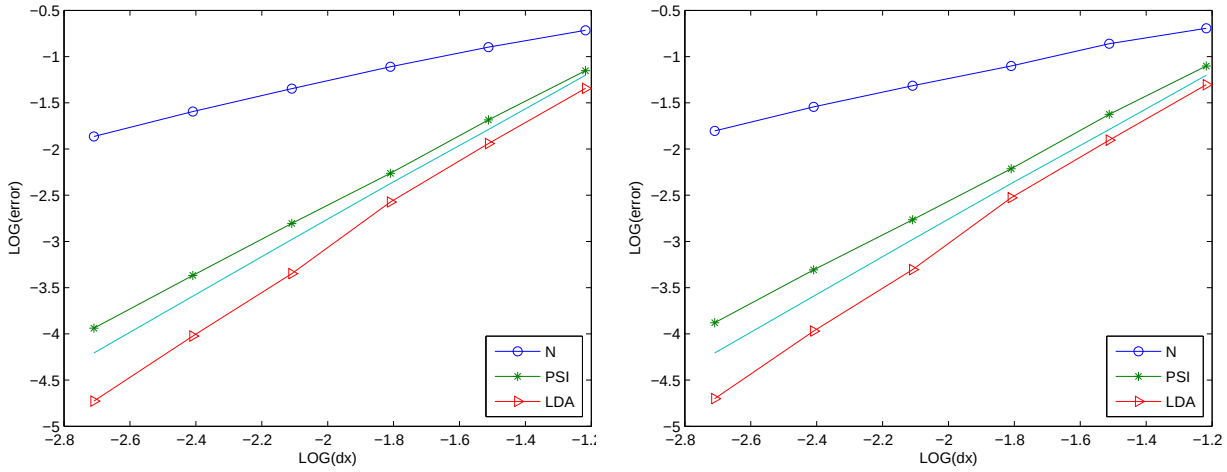

Figure 2.16: Numerical error for grid type A (left), and for grid type B (right) : L_1 error where the solid line without a marker is slope 2.

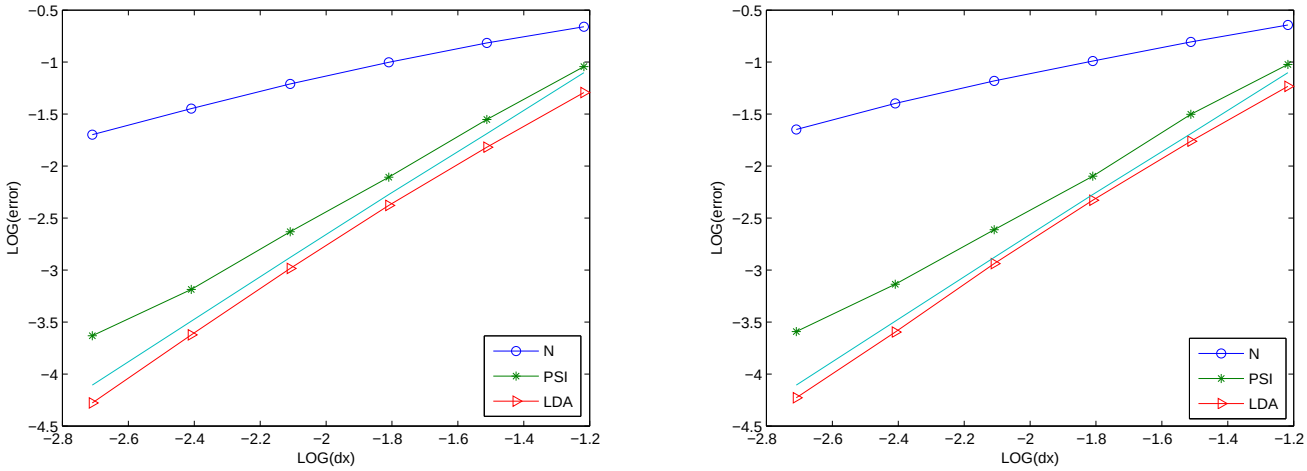

Figure 2.17: Numerical error for grid type A (left), and for grid type B (right) : L_2 error where the solid line without a marker is slope 2.

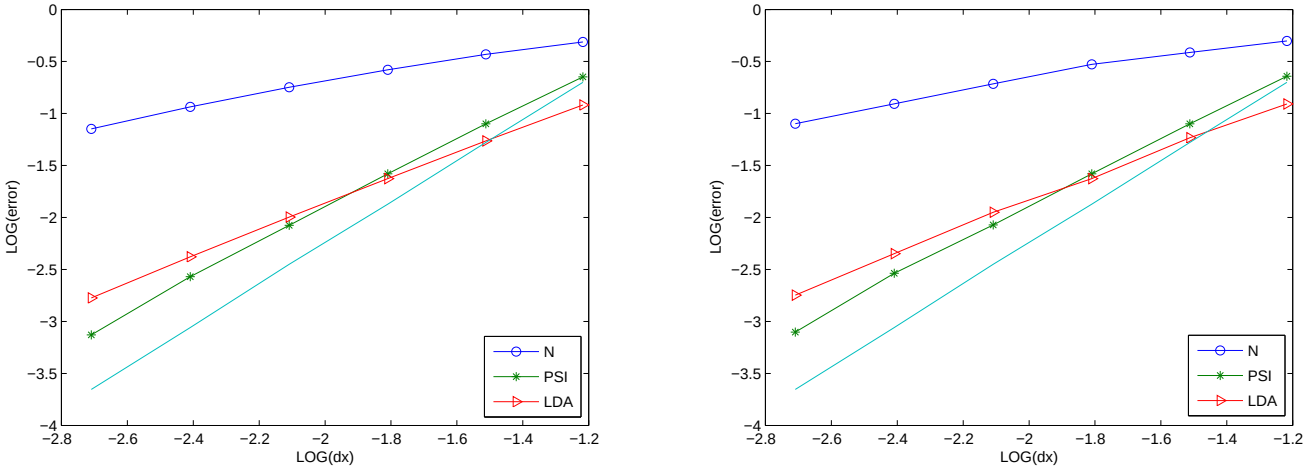

Figure 2.18: Numerical error for grid type A (top right), and for grid type B (top left) : L_∞ error where the solid line without a marker is slope 2.

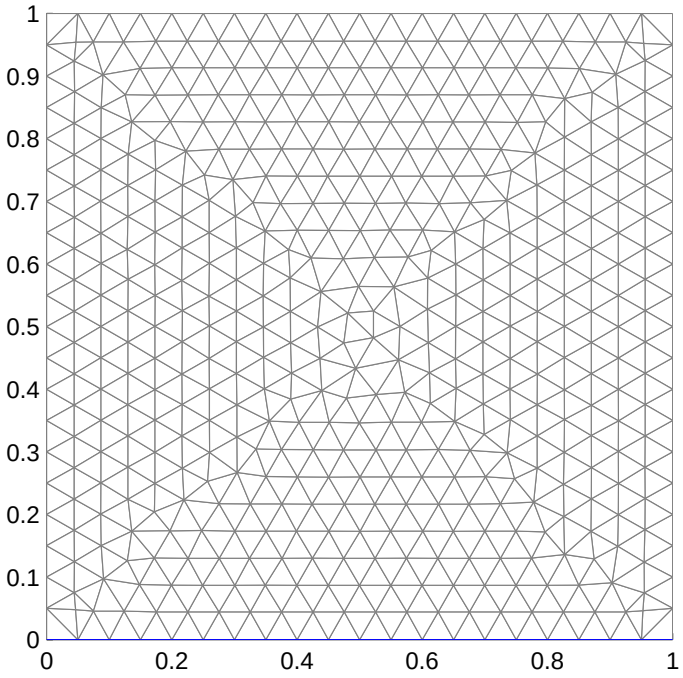

Figure 2.19: A genuinely unstructured triangular mesh, used for the test case which deals with discontinuous solution for Burgers' equation.

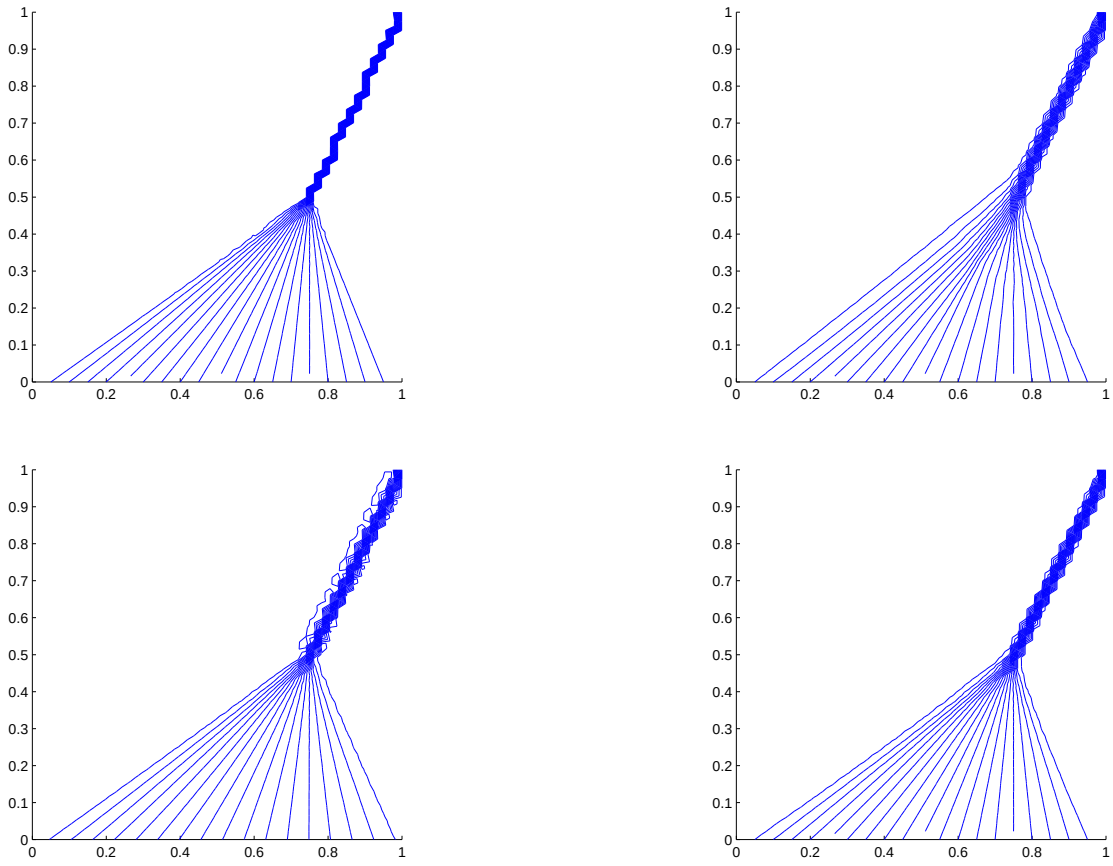

Figure 2.20: Solutions to the Burgers' equation test case, showing the isolines of the exact (top left) and N (top right), LDA (bottom left) and PSI (bottom right) solutions.

Chapter 3

High Order Fluctuation Splitting Schemes

3.1 Introduction

The construction of fluctuation splitting schemes which have higher than second order accuracy is of fundamental significance [8, 67]. This is mainly because numerical experiments on scalar advection show that very high order schemes are more efficient than second-order schemes, because the high reduction of the error due to the high order accuracy compensates for the large number of operations needed to obtain the very high order approximation [82]. Another, more compelling, reason is simply because the approximation of time-dependent problems demand the discrete forms of both spatial and temporal derivative terms to be of a very high order of accuracy, so that the degree of accuracy is maintained over a long time [3, 6, 27, 56].

In this chapter two existing schemes devised in order to achieve higher than second order fluctuation splitting schemes, presented by Abgrall and Roe [8], and Caraeni [17] will be discussed. Moreover, a new alternative to these existing schemes, named the additional neighbouring nodes (ANN) scheme, will also be introduced and described here. However, even though each approach achieved higher than second order accuracy, none of them satisfies the positivity property. Consequently, a new technique was devised by Hubbard [41], which imposes positivity on these high order schemes. This procedure

which will also be discussed in this chapter.

3.2 Abgrall-Roe Scheme

This scheme is a very high order fluctuation splitting scheme which was developed recently for the numerical solution of first order steady conservation laws, by Abgrall and Roe [8]. In the classical low order fluctuation splitting schemes, it is supposed that the dependent variable u has a linear variation over a mesh cell. In order to calculate a high order fluctuation within the cell, one assumes that the dependent variable has a high order polynomial variation over each cell. The idea was to develop a scheme in the context of triangular or tetrahedral cells, whose unknowns are stored and updated using additional nodes created by uniformly subdividing the global mesh, see Figure 3.1, so that it is possible to construct a high order interpolating polynomial on each cell. This then results in a fluctuation that can be evaluated on any of the subcells using a suitable quadrature rule. The purpose is to allow this construction to achieve high order accuracy, initially for solving steady state problems.

For constructing a third order scheme the first stage is to allow each triangle to be equipped with additional degrees of freedom to the values at the vertices. For example, Figure 3.1 shows the case $k = 2$ using p^k triangular elements whose degrees of freedom are the values of the solution at the points within T, shown in the Figure 3.1, creating k^2 sub-triangles within T [8]. The construction of an upwind fluctuation splitting scheme, for any degree of freedom σ, is given as

$$u_\sigma^{n+1} = u_\sigma^n - \frac{\Delta t}{S'_\sigma} \sum_{T,\sigma\in T} \psi_\sigma^T \tag{3.1}$$

where

$$\psi_\sigma^T = \sum_{T_\xi,\sigma\in T_\xi} \phi_\sigma^{T_\xi} \ . \tag{3.2}$$

Here σ denotes a point that may be one of the vertices of the original cell, or the additional points introduced by the sub-triangulation, T_ξ expresses a generic sub-triangle and S'_σ is the area of the median dual control volume associated with the sub-triangle node.

Consider a triangle as in Figure 3.1 for the case $k = 2$, with T_1, T_2, T_3 and T_4 being the subtriangles, and $\phi_\sigma^{T_\xi}$ representing the fluctuations for $\xi = 1,2,3,4$ which will be sent to the points contained in T. The high order (HO) fluctuation on a subtriangle is given as

$$\phi_\xi^{HO} = \int_{T_\xi} \vec{\lambda} \cdot \nabla u^h \mathrm{d}\Omega \tag{3.3}$$

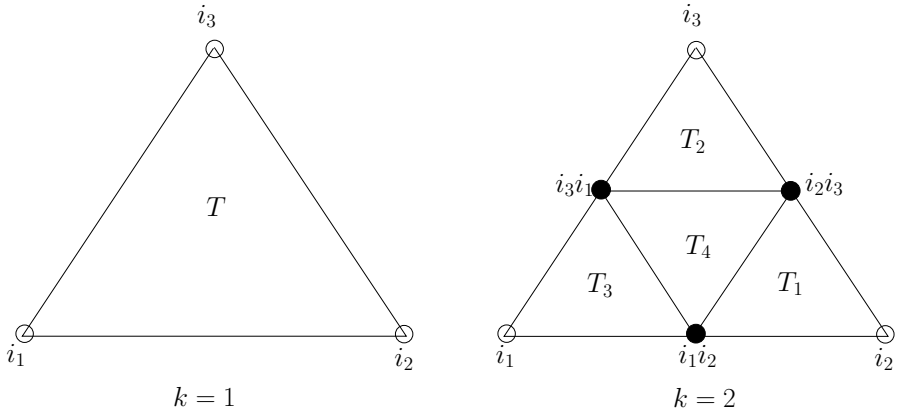

Figure 3.1: Sub-triangles of p^1 and p^2 interpolation.

where u^h represents a piecewise polynomial continuous representation with values stored at all the sub-cell nodes. Now by evaluating (3.3) exactly, the ϕ_ξ^{HO} can be obtained to be distributed to the nodes of the refined mesh. The proposed distribution is based on [8]

$$\phi_\sigma^{T_\xi} = \frac{\left((\phi_\sigma^{T_\xi})^N/\phi_\xi^{HO}\right)^+}{\sum_{\sigma'\in T^\xi}\left((\phi_{\sigma'}^{T_\xi})^N/\phi_\xi^{HO}\right)^+}\phi_\xi^{HO} = \beta_\sigma^{T_\xi}\phi_\xi^{HO}\ . \tag{3.4}$$

Even though these distribution coefficients are bounded between zero and one, in some cases, which will be discussed in detail in Section 3.2.1, the scheme (3.4) gives only zero distribution coefficients for a given subcell, violating conservation. Due to this, Abgrall and Roe [8] proposed a default mode of $\beta_\sigma^{T_\xi} = 1/3$, for use when this type of situation occurs in two dimensions. The distribution coefficients of this scheme are revised to be

$$\beta_\sigma^\xi = \frac{\left((\phi_\sigma^{T_\xi})^N/\phi_\xi^{HO}\right)^+ + \varepsilon}{\sum_{\sigma'\in T^\xi}\left((\phi_{\sigma'}^{T_\xi})^N/\phi_\xi^{HO}\right)^+ + 3\varepsilon}\ , \tag{3.5}$$

with $\varepsilon = 10^{-10}$. Unfortunately these distribution coefficients present a new problem, as they automatically default to central discretisation [41]. This issue will also be discussed in Section 3.2.1. Abgrall and Roe use the above distribution coefficients to calculate the fluctuations at the vertices of the sub-triangles,

$$\phi_\sigma^{T_\xi} = \beta_\sigma^\xi\phi_\xi^{HO}\ , \tag{3.6}$$

and the overall fluctuations at the vertices are

$$\psi_\sigma^T = \sum_{T_\xi, \sigma \in T_\xi} \phi_\sigma^{T_\xi} \ . \tag{3.7}$$

The resulting scheme is high order accurate but not positive. Following this result a method for imposing positivity on this high order scheme was developed by Hubbard [41], which will be discussed in Section 3.5.3.

3.2.1 The Problem

The high order fluctuation splitting scheme on triangular meshes presented by Abgrall and Roe [8] was found to be not positivity preserving from the various numerical experiments that were undertaken. These results were further substantiated by the theoretical investigation carried out. These findings also demonstrated the source of the non-positive results obtained using numerical experiments. This analysis follows [41, 42] and also some closely associated work done independently by Ricchiuto [68] and Abgrall [10]. There are three critical problems.

1. When the high and low order fluctuations have different signs, i.e. $\phi_\xi^N \ \phi_\xi^{HO} < 0$, for a particular sub-triangle, the scheme can violate conservation when (3.4) is used. For example, when the contributions made by the N scheme fluctuation to a particular node σ, $\left(\phi_\sigma^{T_\xi}\right)^N$, is non-negative for all vertices of T_ξ and the contribution from the very high order fluctuation $\left(\phi_\xi\right)^{HO}$ is negative, then the third order fluctuation splitting scheme gives zero distribution coefficients in (3.4), for every vertex of the subcell, infringing on the conservation. Abgrall and Roe [8] proposed the alteration to the distribution coefficients shown in (3.5), introducing a default mode of $\beta_\sigma^\xi = 1/3$, when this type of situation occurred, but this modification forced the scheme to acquire the property of central discretisation, which is not positive.

2. Even when $\phi_\xi^N \ \phi_\xi^{HO} \geq 0$, for sub-triangle ξ, it is also possible to have $\left|\phi_\xi^{HO}\right| \gg \left|\phi_\xi^N\right|$, i.e. the very high order fluctuation ϕ_ξ^{HO} can have a much bigger magnitude than the N scheme fluctuation ϕ_ξ^N. This means that it will affect the positivity of the steady state approximation, since a more restrictive condition than (2.50) is required for the time-stepping procedure to remain positive. Consequently it becomes very difficult to distribute the high order fluctuation to the appropriate vertices of the sub-triangle in a conservative manner while maintaining positivity.

3. In some circumstances, ϕ_ξ^{HO} is nonzero when $u_{i_1} = u_{i_2} = u_{i_3}$ in a subcell. When this situation occurs distributing ϕ_ξ^{HO} to the vertices of subcell ξ, in a conservative

manner while maintaining local or, sometimes, global positivity becomes unattainable. Hence, it is impossible to construct a conservative and locally positive higher than second order accurate fluctuation splitting scheme, if the distribution of the fluctuation in a subcell is restricted to be only to the vertices of that subcell.

3.3 Caraeni's scheme

The essence of Caraeni's scheme is its construction of a high order representation of the dependent variable u using the reconstructed gradients of the solution at the cell nodes to obtain a quadratic interpolant [17, 18, 20]. The first consideration that was made in order to obtain high order accuracy is that u has a quadratic variation over the cell. This can be achieved if the gradient of the dependent variable u is computed and stored at the cell nodes, before computing the high order fluctuation within the cell.

The procedure starts by approximating the cell gradients, using the Green-Gauss theorem, given by

$$\vec{\nabla} u^T = \frac{1}{S_T} \oint_{\partial T} u \vec{n} \, d\Gamma, \tag{3.8}$$

where S_T denote the area of each cell. The cell gradients are then used to approximate the value of the gradients at the nodes using

$$\vec{\nabla} u_i = \frac{1}{\sum_{T \in \cup T_i} {S_T}^{-1}} \sum_{T \in \cup T_i} S_T^{-1} \vec{\nabla} u^T \ . \tag{3.9}$$

Now it is possible to obtain a higher order reconstruction for the variable u over the cell. The values of u at the midpoints of the edge, i.e. those at $i_1 i_2$, $i_2 i_3$ and $i_3 i_1$ in Figure 3.2, are defined using

$$u_{i_1 i_2} = \frac{u_{i_1} - u_{i_2}}{2} + \frac{\vec{\nabla} u_{i_1} - \vec{\nabla} u_{i_2}}{8} \cdot (\vec{x}_{i_2} - \vec{x}_{i_1}) \ , \tag{3.10}$$

where i_1 and i_2 denote the vertices at each end of the cell edge. These values are used to calculate a high order fluctuation within the cell, which is then distributed using the non positive LDA scheme [17, 20]. As in the previous scheme, Caraeni's scheme is high order accurate but not positive, however positivity can also be imposed using the technique presented in [41]. This positive version of Caraeni's scheme will be discussed in Section 3.5.2.

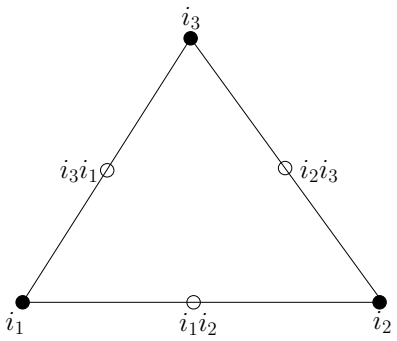

Figure 3.2: Definition of the nodes in a high order triangular cell for Caraeni's scheme.

3.4 The Additional Neighbouring Nodes Scheme

In Sections 3.2 and 3.3, the existing alternatives for constructing very high order fluctuation splitting schemes were presented. Abgrall and Roe [8] showed that by subdividing a triangular mesh to provide the additional degrees of freedom necessary for constructing quadratic polynomials, they were able to achieve a higher order accurate fluctuation splitting scheme. Another alternative to this approach was presented by Caraeni [17], who was able to recover solution gradients at the mesh nodes and use these to obtain a quadratic interpolant, which also led to higher than second order accurate fluctuation splitting scheme.

What will be presented here is a high order fluctuation splitting scheme that is constructed using extra information about the dependent variable stored at the additional neighbouring nodes of the global mesh. These additional neighbouring nodes provide the additional degrees of freedom that are necessary to develop a high order polynomial representation of the dependent variables, and hence evaluate the fluctuation ϕ^T with an appropriate degree of accuracy.

The first stage in the development of the additional neighbouring nodes scheme is to consider a mesh composed of triangles, denoted by T_i, with vertices i_1, i_2, i_3. In addition, $(i_l)_{4\leq l\leq n}$ are the other collocation points, as shown in Figure 3.3 for $n = 10$ to construct a unique cubic polynomial. For a given triangulation, we seek an interpolant that is piecewise polynomial of degree p in each triangle T_i, and therefore this triangulation needs to provide each T_i with

$$n = \frac{1}{2}(p+1)(p+2)\,, \tag{3.11}$$

degrees of freedom. Figure 3.4 shows the case $k = 2$, and the additional vertices i_4, i_5, i_6.

The construction of a continuous piecewise higher degree polynomial interpolant is achieved using the values of u at the additional mesh nodes neighbouring a given cell. For

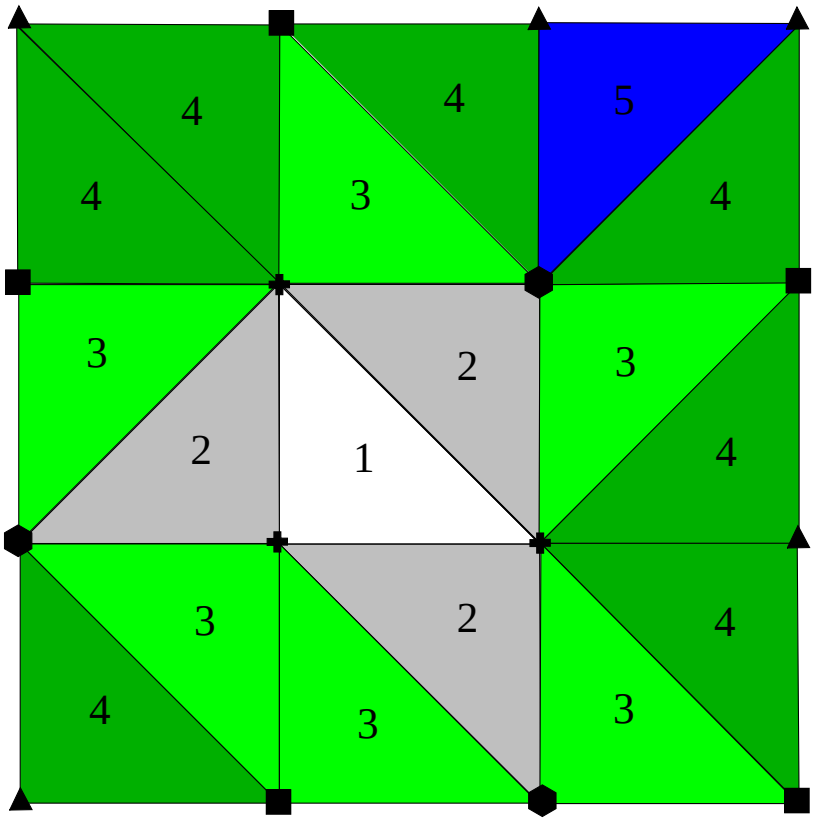

Figure 3.3: The nodes over which the high order polynomial representation of the dependent variables will be fitted. The crosses at the vertices of cell 1, plus the immediate neighbouring cell 2 vertices, indicated by hexagons, identify the nodes to be added for developing quadratic polynomials. If the next immediate neighbouring cells' vertices of cell 3 denoted by squares are also added, it will be possible to construct cubic polynomials etc. The numbers show the order in which the neighbouring cells are chosen to be added to the stencil.

constructing a quadratic interpolant we use three additional nodes, which are obtained from the three neighbouring cells by choosing the nodes opposite the given cell's edges, denoted 2 in Figure 3.3. These make it possible to construct a quadratic interpolating polynomial on each original cell of the mesh. In general, a p^{th}-order stencil has n nodes (3.11), and the complete polynomial in two dimensions of p^{th} degree is given by

$$u = \sum_{i=1}^{n} a_i x^e y^f , \qquad e + f \leq p \, . \tag{3.12}$$

The complete set of $n = 10$ points for the cubic polynomial (cells labelled 1-3) is shown in Figure 3.3. For constructing a quadratic interpolant, the polynomial involves six constants, which can be expressed in terms of the nodal values of the variable being interpo-

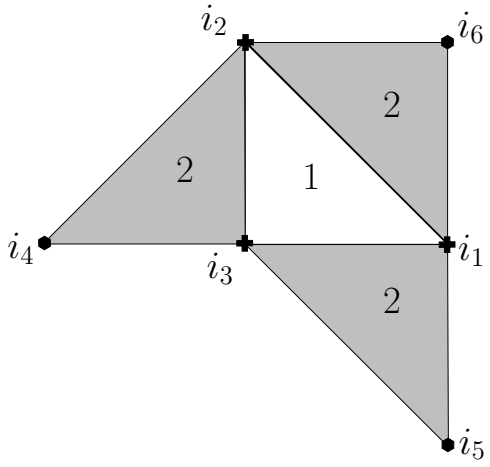

Figure 3.4: The stencil over which quadratic polynomial will be fitted, where i_1, i_2 and i_3 (crosses), are the vertices of cell 1, i_4, i_5 and i_6 (hexagons) identify the neighbouring nodes from cells identified by 2, to be added for developing quadratic polynomials.

lated (shown in Figure 3.4) as

$$u_j = a_1 + a_2 x_j + a_3 y_j + a_4 x_j y_j + a_5 x_j^2 + a_6 y_j^2 \qquad j = 1, ..., n \; . \tag{3.13}$$

This generates the matrix equation

$$B\underline{a} = \underline{u} \; , \tag{3.14}$$

where B is a square matrix containing the coefficients $1, .., y_j^2$, $\underline{a}$ and $\underline{u}$ are vectors containing the coefficients a_j and u_j. Once this matrix equation is solved for the coefficients, it will be possible to construct the third order midpoint values of u, on each edge of the original cell, $i_1 i_2$, $i_2 i_3$ and $i_3 i_1$. After the unique local quadratic interpolant on each cell of the original mesh is constructed, an additional stage is involved to attain conservation, since the continuity of the representation could be hampered. These issue arises as the reconstruction of the quadratic interpolant within each mesh cell is achieved by extending the stencil to obtain information from the neighbouring cells' nodes, making the stencil selection local for each cell. This means that the stencils are different for any given pair of neighbouring cells, and give two different polynomial representations for each internal mesh edge, the two local quadratic representations over the two adjacent cells. However, to produce a continuous representation, it is possible to use an average of the two neighbouring quadratic interpolants across each cell edge, which gives a quadratic interpolant on each edge of the original mesh. Quadrature is then used to evaluate the high order fluctuation, by evaluating (2.6) exactly. The high order fluctuation can then be used to

update the solution using, for example, an LDA distribution (2.57),

$$(\phi_i^T)^{ANN} = \frac{k_i^+}{\sum_j k_j^+}(\phi^T)^{ANN} = \beta_i^{LDA}(\phi^T)^{ANN} \ . \tag{3.15}$$

It is important to note that when the LDA distribution is used, this high order accurate scheme is not positive. A solution to this problem will be outlined later on in this chapter.

For boundary cells, as shown in Figure 3.5, it is impossible to pick enough additional nodes from the immediate neighbouring cells for constructing a continuous piecewise higher degree polynomial interpolant. This is because the boundary cells will always have one or two of the neighbouring cells, and thereby their corresponding nodes, absent in the mesh structure. As a consequence of this, the boundary cells will always be treated as special cases.

For boundary cells in regular meshes, there are various ways of choosing more neighbouring nodes for constructing higher degree polynomial interpolants. One such way of choosing between the various neighbouring nodes beyond the given cell is to continuously add the necessary amount of neighbouring nodes until enough neighbouring nodes are found for constructing the local polynomial.

To explain further, by looking at Figure 3.5, it is possible to see that to construct a quadratic interpolant, the immediate neighbouring cell's nodes, indicated by the hexagons, do not produce enough information, as at least six nodal values are required. However it is possible to collect as many or even more nodes as required for the quadratic polynomial to be constructed by adding the neighbouring neighbour cells' nodes, indicated by the squares in the figure. In this case, this gives eight nodes and consequently more columns in the system (3.14). Now, even though there will be more equations than unknowns, once the polynomials are constructed, it will be possible to use a singular value decomposition [39, 85], to find a solution to the resulting system and consequently the high order degree polynomial interpolant. In general, using singular value decomposition is advantageous in the case where B in (3.14) is a singular matrix, or if there are fewer equations than unknowns.

For radically irregular mesh structures, as shown in Figure 3.6, the basic ideas of the additional neighbouring nodes scheme carry over in a straightforward manner, but its application introduces new problems. These new problems arise because the construction of the polynomial interpolant depends on the closeness of the neighbouring cells' nodes to a given cell, and this type of stencil selection leads to the addition of more layers of neighbouring nodes, while also extending the distance between the nodes, due to the irregularity of the mesh structure. This creates a similar problem to that seen in the boundary

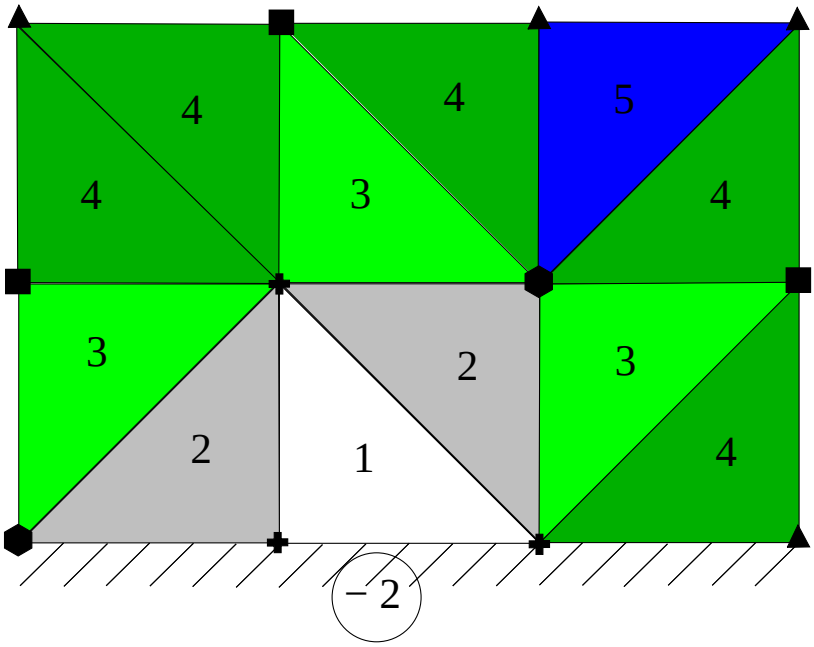

Figure 3.5: The cells that will be added to the stencil at the boundary cell indicated by 1, for the additional neighbouring nodes scheme. To construct quadratic polynomials for boundary cells 1, the crosses at the vertices of cell 1, plus the immediate neighbouring cell 2 vertices indicated by hexagons, plus the three vertices of cell 3 indicated by squares, will be used. -2 within the circle indicates the boundary and the numbers show the order in which the neighbouring cells are chosen to be added to the stencil.

cells, because it is difficult to collect the necessary number of nodes from the immediate neighbouring cells. As the nodes of the neighbouring cells could be further away from the cell, this can also make the information taken from these nodes sensitive to the mesh structure.

One suggestion to be made regarding the stencil selection is that, instead of selecting the immediate nodes of the cells neighbouring a given cell, it could be better to select the closest neighbouring nodes in a geometric sense, to obtain information for constructing a continuous piecewise higher degree polynomial interpolant, so that the stencil would not extended as far in space. In order to select the necessary number of the closest neighbouring nodes for constructing a high order polynomial, it could be possible to use distances between the centres of the cells or their size. Once the stencil contains enough nodes the singular value decomposition is again used to find the least squares fit polynomial.

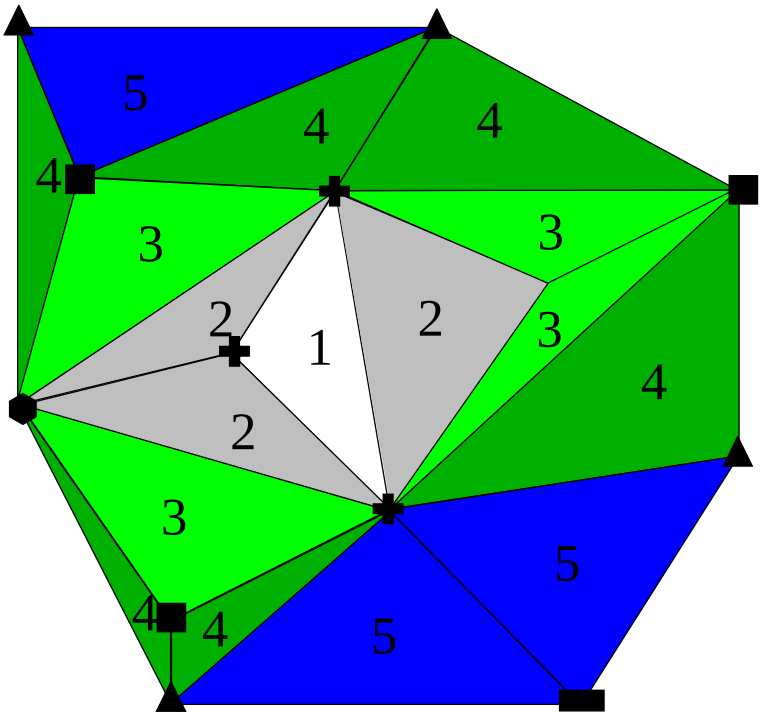

Figure 3.6: The additional neighbouring nodes scheme's choice of the closest neighbouring nodes that will be added to the stencil for a radically irregular mesh structure. The crosses at the vertices of cell 1, plus the vertices indicated by hexagons, and the three vertices of cell 3 indicated by squares, identify the nodes to be added for developing quadratic polynomials. However, this stencil selection adds more layers of neighbouring nodes and also takes information from the nodes of the surrounding cells which are further away, making the scheme sensitive to the mesh structure.

3.5 Modified Scheme

This section will describe a technique developed by Hubbard [41], which guarantees the absence of spurious oscillations by applying an additional smoothing stage. The explicit construction of a higher than second order scheme which is both positive and linearity preserving for the steady state advection problem will be outlined. Since the source of the non-positivity of the very high order scheme presented by Abgrall and Roe [8] was identified in the previous chapter, what will be outlined here is one possible approach which can be taken in order to improve the distribution of a modified form of the very high order fluctuation ϕ_{ξ}^{HO} to the appropriate vertices of the subtriangle (or subcell) in a conservative manner while imposing both local and global positivity.

The first step in constructing the modified third order scheme is understanding the fact that by modifying the interpolant, and consequently the fluctuation, it is possible to construct a positive distribution scheme within the existing framework. To explain further, by modifying the interpolant in a way which allows a locally positive distribution scheme, even when the fluctuation in a cell is distributed only to that cell's vertices, a new scheme which is both positive and higher than second order accurate for the steady state advection problem can be produced. In the previous Sections, 2.5.1 and 2.5.3, the linear interpolant used for the N and PSI schemes led to a positive scheme [66], and here the N scheme will also be used as the basis for the higher order case to help decide how to distribute a limited amount of a high order correction term.

Considering a triangular mesh cell, see Figure 3.1 on the right, the high order representation within that particular cell can be written as $\overline{u}(\vec{x}) + \delta u(\vec{x})$, where $\overline{u}(\vec{x})$ is the linear interpolant of the dependent variable u at the vertices of the cell, and $\delta u(\vec{x})$ is the high order correction to the interpolant over that cell. Thus, if $\delta u^{'}(\vec{x})$ represents a modified high order correction along the edges of the cell, the modified interpolant can be written as $u^{'}(\vec{x}) = \overline{u}(\vec{x}) + \delta u^{'}(\vec{x})$. The high order correction for each edge $i_1 i_2$ of the cell is limited so that

$$\| \delta u^{'}_{i_1 i_2}(\vec{x}) \| \leq K \mid u_{i_1} - u_{i_2} \mid \qquad \forall \vec{x} = \mu \vec{x}_{i_1} + (1-\mu)\vec{x}_{i_2}, \quad 0 \leq \mu \leq 1, \tag{3.16}$$

for some constant $K \geq 0$, and this condition allows the fluctuation obtained by using the modified interpolant to be distributed in a locally positive manner, for an appropriate time-step restriction in (2.11).

The limiting of the high order polynomial is conducted at every quadrature point so that the above relations are satisfied. The optimal choice for the constant K is still an open question but in general there are three values for the constant K which have particular

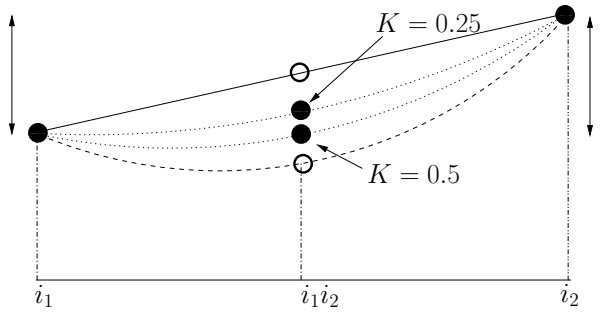

Figure 3.7: The limiting procedure for a general case along a cell edge, where • show the limited values at the quadrature points, and ∘ indicate the linear and quadratic limits. The double ended arrows indicate the values the polynomial is allowed to take at the quadrature point. The solid line indicates the linear interpolant $\overline{u}(\vec{x})$, the dashed line indicates the quadratic interpolant $u(\vec{x})$ and the dotted lines are the limited interpolant $u^{'}(\vec{x})$ for $K = 0.25$ and $K = 0.5$.

interest

- $K = 0$, reduces to the linear case and the PSI scheme is recovered.
- $K = 0.25$, which guarantees a monotonic interpolant along every edge and is the largest value that guarantees a limited monotonic interpolant along each edge. The monotonicity proof is outlined in [41]. Figure 3.7 illustrates the geometric effect of using $K = 0.25$ which clearly lies between the linear and quadratic interpolants. This value of K will also be used in all the results conducted in this work, because using larger values of K was found by experiment to reduce the rate of convergence to steady state.
- $K = 0.5$, which guarantees that the midpoint interpolant values are bounded by the endpoint values for any given edge. Figure 3.7 shows the the geometric effect of using $K = 0.5$. It is worth noting that the time step restriction will become more severe as K increases [41].

It can easily be shown that this modification allows a positive distribution as follows. The fluctuation due to the limited interpolant $u^{'}(\vec{x})$ for a general edge can be written as

$$\oint_{\partial\Omega} u'\vec{\lambda}\cdot\vec{n}\,\mathrm{d}\Gamma = \sum_{edges}\int_{i_1}^{i_2} u'\vec{\lambda}\cdot\vec{n}\,\mathrm{d}\Gamma \tag{3.17}$$

$$= \sum_{edges}\left[\int_{i_1}^{i_2} u'\vec{\lambda}\cdot\vec{n}\,\mathrm{d}\Gamma + \int_{i_1}^{i_2}\bar{u}\,\vec{\lambda}\cdot\vec{n}\,\mathrm{d}\Gamma - \int_{i_1}^{i_2}\bar{u}\,\vec{\lambda}\cdot\vec{n}\,\mathrm{d}\Gamma\right]$$

$$= \sum_{edges}\left[\int_{i_1}^{i_2}(u'-\bar{u})\,\vec{\lambda}\cdot\vec{n}\,\mathrm{d}\Gamma + \int_{i_1}^{i_2}\bar{u}\,\vec{\lambda}\cdot\vec{n}\,\mathrm{d}\Gamma\right]$$

$$= \sum_{edges}\left[\int_{i_1}^{i_2}\delta u'\,\vec{\lambda}\cdot\vec{n}\,\mathrm{d}\Gamma + \int_{i_1}^{i_2}\bar{u}\,\vec{\lambda}\cdot\vec{n}\,\mathrm{d}\Gamma\right]\ . \tag{3.18}$$

In order to ensure that (3.16) is satisfied, but high order is retained whenever possible, a function $\alpha_{i_1 i_2}(\vec{x})$ is defined along each edge which satisfies

$$\delta u'(\vec{x}) = \alpha_{i_1 i_2}(\vec{x})(u_{i_1} - u_{i_2})\ . \tag{3.19}$$

(3.18) then gives

$$\oint_{\partial\Omega} u'\vec{\lambda}\cdot\vec{n}\,\mathrm{d}\Gamma = \sum_{edges}\left[\int_{i_1}^{i_2}\alpha_{i_1 i_2}(u_{i_1}-u_{i_2})\vec{\lambda}\cdot\vec{n}\,\mathrm{d}\Gamma + \int_{i_1}^{i_2}\bar{u}\,\vec{\lambda}\cdot\vec{n}\,\mathrm{d}\Gamma\right]\ . \tag{3.20}$$

In order to satisfy (3.16), $\mid\alpha(\vec{x})\mid \leq K$ is required for all $\vec{x}$ on the given edge. It is enough that the inequality is satisfied at the quadrature points and in this work, $\alpha_{i_1 i_2}$ is chosen at the edge midpoint (the additional quadrature point necessary for the application of Simpson's rule) to take the form

$$\alpha_{i_1 i_2} = max\left(-K, min\left[K, \frac{u_{i_1 i_2} - \frac{(u_{i_1}+u_{i_2})}{2}}{u_{i_1}-u_{i_2}}\right]\right)\ , \tag{3.21}$$

in which division by zero is avoided by making sure the denominator does not become zero.

Now, note that the low order fluctuation can be written

$$\begin{aligned}\phi^{LO} &= -\frac{1}{2}\sum_{i\in T} u_i \widetilde{\vec{\lambda}}\cdot\vec{n}_i \\ &= \frac{(u_{i_1}-u_{i_2})\widetilde{\vec{\lambda}}\cdot\vec{n_{i_2}}}{2} + \frac{(u_{i_1}-u_{i_3})\widetilde{\vec{\lambda}}\cdot\vec{n_{i_3}}}{2} \\ &= \phi_{i_1 i_2} + \phi_{i_1 i_3} \\ &= k_{i_2}(u_{i_1}-u_{i_2}) + k_{i_3}(u_{i_1}-u_{i_3})\ , \end{aligned} \tag{3.22}$$

where $\widetilde{\vec{\lambda}}$ is the linearised advection velocity, from (2.7). The inflow parameters are defined as $k_{i_2} = \frac{1}{2}\widetilde{\vec{\lambda}}\cdot\vec{n_{i_2}}$ and $k_{i_3} = \frac{1}{2}\widetilde{\vec{\lambda}}\cdot\vec{n_{i_3}}$ and i_2 and i_3 are chosen so that k_{i_2} and k_{i_3} are of the same sign or zero. Now it is worth noting that the N scheme can be viewed as distributing $\phi_{i_1 i_2}$ and $\phi_{i_1 i_3}$ (3.22) via

$$\begin{aligned}
&S_{i_2}u_{i_2} \to S_{i_2}u_{i_2} + \frac{1}{2}\Delta t\widetilde{\vec{\lambda}}\cdot\vec{n_{i_2}}(u_{i_1}-u_{i_2}) \qquad \text{if} \qquad \widetilde{\vec{\lambda}}\cdot\vec{n_{i_2}} \geq 0 \\
&S_{i_1}u_{i_1} \to S_{i_1}u_{i_1} + \frac{1}{2}\Delta t\widetilde{\vec{\lambda}}\cdot\vec{n_{i_2}}(u_{i_1}-u_{i_2}) \qquad \text{if} \qquad \widetilde{\vec{\lambda}}\cdot\vec{n_{i_2}} < 0 \\
&S_{i_3}u_{i_3} \to S_{i_3}u_{i_3} + \frac{1}{2}\Delta t\widetilde{\vec{\lambda}}\cdot\vec{n_{i_3}}(u_{i_1}-u_{i_3}) \qquad \text{if} \qquad \widetilde{\vec{\lambda}}\cdot\vec{n_{i_3}} \geq 0 \\
&S_{i_1}u_{i_1} \to S_{i_1}u_{i_1} + \frac{1}{2}\Delta t\widetilde{\vec{\lambda}}\cdot\vec{n_{i_3}}(u_{i_1}-u_{i_3}) \qquad \text{if} \qquad \widetilde{\vec{\lambda}}\cdot\vec{n_{i_3}} < 0\ .
\end{aligned} \tag{3.23}$$

An alternative to (3.23) can be derived from rewriting the low order fluctuation as

$$\phi^N = k_{i_2}^+(u_{i_1}-u_{i_2}) + k_{i_2}^-(u_{i_1}-u_{i_2}) + k_{i_3}^+(u_{i_1}-u_{i_3}) + k_{i_3}^-(u_{i_1}-u_{i_3}), \tag{3.24}$$

where $[\,]^+$ and $[\,]^-$ are the positive and the negative parts of the argument within the square brackets, and the vertices i_1, i_2 and i_3 are again chosen according to the inflow edges, as directed by the N scheme. This leads to a formulation of the distribution given by

$$\begin{aligned}
S_{i_1}u_{i_1} &\to S_{i_1}u_{i_1} + \Delta t[k_{i_2}^-(u_{i_1}-u_{i_2}) + k_{i_3}^-(u_{i_1}-u_{i_3})] \\
S_{i_2}u_{i_2} &\to S_{i_2}u_{i_2} + \Delta t k_{i_2}^+(u_{i_1}-u_{i_2}) \\
S_{i_3}u_{i_3} &\to S_{i_3}u_{i_3} + \Delta t k_{i_3}^+(u_{i_1}-u_{i_3})\ .
\end{aligned} \tag{3.25}$$

These are useful alternative formulations for the distribution of the higher order fluctuation. Now, returning to the high order fluctuation in (3.20) and using the fact that

$$(u_{i_2} - u_{i_3}) \equiv (u_{i_1} - u_{i_3}) - (u_{i_1} - u_{i_2}) \;, \tag{3.26}$$

it is possible to derive the form

$$\begin{aligned}
\phi^{LIM} &= \oint_{\partial\Omega} u^{'}\vec{\lambda}\cdot\vec{n}\,\mathrm{d}\Gamma \qquad (3.27)\\
&= \frac{1}{2}(u_{i_1} - u_{i_2})\widetilde{\vec{\lambda}}\cdot\vec{n_{i_2}} + \frac{1}{2}(u_{i_1} - u_{i_3})\widetilde{\vec{\lambda}}\cdot\vec{n_{i_3}}\\
&+ \int_{i_1}^{i_2}\alpha_{i_1i_2}(u_{i_1} - u_{i_2})\vec{\lambda}\cdot\vec{n}\,\mathrm{d}\Gamma - \int_{i_2}^{i_3}\alpha_{i_2i_3}(u_{i_1} - u_{i_2})\vec{\lambda}\cdot\vec{n}\,\mathrm{d}\Gamma\\
&- \int_{i_3}^{i_1}\alpha_{i_3i_1}(u_{i_1} - u_{i_3})\vec{\lambda}\cdot\vec{n}\,\mathrm{d}\Gamma + \int_{i_2}^{i_3}\alpha_{i_2i_3}(u_{i_1} - u_{i_3})\vec{\lambda}\cdot\vec{n}\,\mathrm{d}\Gamma,
\end{aligned}$$

where i_1, i_2 and i_3 are the vertices of the cell (or subcell) taken in an anticlockwise manner. This then gives

$$\begin{aligned}
\oint_{\partial\Omega} u^{'}\vec{\lambda}\cdot\vec{n}\,\mathrm{d}\Gamma &= \left[\frac{1}{2}\widetilde{\vec{\lambda}}\cdot\vec{n_{i_2}} + \int_{i_1}^{i_2}\alpha_{i_1i_2}\vec{\lambda}\cdot\vec{n}\,\mathrm{d}\Gamma - \int_{i_2}^{i_3}\alpha_{i_2i_3}\vec{\lambda}\cdot\vec{n}\,\mathrm{d}\Gamma\right](u_{i_1} - u_{i_2})\\
&+ \left[\frac{1}{2}\widetilde{\vec{\lambda}}\cdot\vec{n_{i_3}} - \int_{i_3}^{i_1}\alpha_{i_3i_1}\vec{\lambda}\cdot\vec{n}\,\mathrm{d}\Gamma + \int_{i_2}^{i_3}\alpha_{i_2i_3}\vec{\lambda}\cdot\vec{n}\,\mathrm{d}\Gamma\right](u_{i_1} - u_{i_3})\\
&= K_{i_1i_2}(u_{i_1} - u_{i_2}) + K_{i_1i_3}(u_{i_1} - u_{i_3}) \;. \qquad (3.28)
\end{aligned}$$

This is now written in similar form to the linear fluctuation (3.22).

Note that if $K_{i_1i_2}$ has the same sign as k_{i_2} in (3.28), sending $K_{i_1i_2}(u_{i_1} - u_{i_2})$ to the same node as $k_{i_2}(u_{i_1} - u_{i_2})$ will lead to a locally positive distribution. Otherwise, if they are of a different sign, then sending $K_{i_1i_2}(u_{i_1} - u_{i_2})$ to the other edge node updated by $k_{i_2}(u_{i_1} - u_{i_2})$ on edge i_1i_2, leads to an update which is locally positive. The same procedure will be performed for the fluctuation associated with edge i_1i_3. This is the essence of the positive scheme on which the high order scheme will be based.

Importantly, due to the constraints on $\alpha_{i_1i_2}$, $\alpha_{i_2i_3}$ and $\alpha_{i_3i_1}$ in (3.28), $K_{i_1i_2}$ and $K_{i_1i_3}$ are clearly bounded. Furthermore, simple bounds can be derived for these coefficients on each edge, i.e.

$$
\begin{aligned}
|\,K_{i_1 i_2}\,| &= \left|\frac{1}{2}\widetilde{\vec{\lambda}}\cdot\vec{n_{i_2}} + \int_{i_1}^{i_2}\alpha\vec{\lambda}\cdot\vec{n}\,\mathrm{d}\Gamma - \int_{i_2}^{i_3}\alpha\vec{\lambda}\cdot\vec{n}\,\mathrm{d}\Gamma\right| \\
&\leq \left|\frac{1}{2}\widetilde{\vec{\lambda}}\cdot\vec{n_{i_2}}\right| + \left|\int_{i_1}^{i_2}\alpha\vec{\lambda}\cdot\vec{n}\,\mathrm{d}\Gamma\right| + \left|\int_{i_2}^{i_3}\alpha\vec{\lambda}\cdot\vec{n}\,\mathrm{d}\Gamma\right| \\
&\leq \left|\frac{1}{2}\widetilde{\vec{\lambda}}\cdot\vec{n_{i_2}}\right| + \int_{i_1}^{i_2}|\alpha|\left|\vec{\lambda}\cdot\vec{n}\right|\,\mathrm{d}\Gamma + \int_{i_2}^{i_3}|\alpha|\left|\vec{\lambda}\cdot\vec{n}\right|\,\mathrm{d}\Gamma \\
&\leq \left|\frac{1}{2}\widetilde{\vec{\lambda}}\cdot\vec{n_{i_2}}\right| + K\int_{i_1}^{i_2}\left|\vec{\lambda}\cdot\vec{n}\right|\,\mathrm{d}\Gamma + K\int_{i_2}^{i_3}\left|\vec{\lambda}\cdot\vec{n}\right|\,\mathrm{d}\Gamma \\
&\leq \left|\frac{1}{2}\widetilde{\vec{\lambda}}\cdot\vec{n_{i_2}}\right| + K\left[\max_{i_1\to i_2}\left|\vec{\lambda}\cdot\vec{n_{i_3}}\right| + \max_{i_2\to i_3}\left|\vec{\lambda}\cdot\vec{n_{i_1}}\right|\right] \qquad (3.29)
\end{aligned}
$$

and

$$
\begin{aligned}
|\,K_{i_1 i_3}\,| &= \left|\frac{1}{2}\widetilde{\vec{\lambda}}\cdot\vec{n_{i_3}} - \int_{i_3}^{i_1}\alpha\vec{\lambda}\cdot\vec{n}\,\mathrm{d}\Gamma + \int_{i_2}^{i_3}\alpha\vec{\lambda}\cdot\vec{n}\,\mathrm{d}\Gamma\right| \\
&\leq \left|\frac{1}{2}\widetilde{\vec{\lambda}}\cdot\vec{n_{i_3}}\right| + \left|\int_{i_3}^{i_1}\alpha\vec{\lambda}\cdot\vec{n} + \mathrm{d}\Gamma\right| + \left|\int_{i_2}^{i_3}\alpha\vec{\lambda}\cdot\vec{n}\,\mathrm{d}\Gamma\right| \\
&\leq \left|\frac{1}{2}\widetilde{\vec{\lambda}}\cdot\vec{n_{i_3}}\right| + \int_{i_3}^{i_1}|\alpha|\left|\vec{\lambda}\cdot\vec{n}\right|\,\mathrm{d}\Gamma + \int_{i_2}^{i_3}|\alpha|\left|\vec{\lambda}\cdot\vec{n}\right|\,\mathrm{d}\Gamma \\
&\leq \left|\frac{1}{2}\widetilde{\vec{\lambda}}\cdot\vec{n_{i_3}}\right| + K\int_{i_3}^{i_1}\left|\vec{\lambda}\cdot\vec{n}\right|\,\mathrm{d}\Gamma + K\int_{i_2}^{i_3}\left|\vec{\lambda}\cdot\vec{n}\right|\,\mathrm{d}\Gamma \\
&\leq \left|\frac{1}{2}\widetilde{\vec{\lambda}}\cdot\vec{n_{i_3}}\right| + K\left[\max_{i_3\to i_1}\left|\vec{\lambda}\cdot\vec{n_{i_2}}\right| + \max_{i_2\to i_3}\left|\vec{\lambda}\cdot\vec{n_{i_1}}\right|\right]\ . \qquad (3.30)
\end{aligned}
$$

Since $K_{i_1 i_2}$ and $K_{i_1 i_3}$ are bounded, it is now automatically possible, for small enough Δt, to use the limited fluctuation (3.28) to produce a locally positive update to the dependent variable u. As in the N scheme formulation given by (3.22)-(3.25), the contribution due to edge $i_1 i_2$ and $i_1 i_3$ can be written as

$$
\begin{aligned}
&S_{i_2}u_{i_2} \to S_{i_2}u_{i_2} + \Delta t K_{i_1 i_2}(u_{i_1} - u_{i_2}) \quad \text{if} \quad K_{i_1 i_2} \geq 0 \\
&S_{i_1}u_{i_1} \to S_{i_1}u_{i_1} + \Delta t K_{i_1 i_2}(u_{i_1} - u_{i_2}) \quad \text{if} \quad K_{i_1 i_2} < 0 \\
&S_{i_3}u_{i_3} \to S_{i_3}u_{i_3} + \Delta t K_{i_1 i_3}(u_{i_1} - u_{i_3}) \quad \text{if} \quad K_{i_1 i_3} \geq 0 \\
&S_{i_1}u_{i_1} \to S_{i_1}u_{i_1} + \Delta t K_{i_1 i_3}(u_{i_1} - u_{i_3}) \quad \text{if} \quad K_{i_1 i_3} < 0\ . \qquad (3.31)
\end{aligned}
$$

For small enough Δt, this clearly leads to a positive distribution, which will be shown shortly. Note that along the line of (3.24), the limited high order fluctuation can also be

written as

$$\phi^{LIM} = K^{+}_{i_1 i_2}(u_{i_1} - u_{i_2}) + K^{-}_{i_1 i_2}(u_{i_1} - u_{i_2}) + K^{+}_{i_1 i_3}(u_{i_1} - u_{i_3}) + K^{-}_{i_1 i_3}(u_{i_1} - u_{i_3}), \qquad (3.32)$$

and that the distribution (3.31) is equivalently given as

$$\begin{aligned} S_{i_1} u_{i_1} &\rightarrow S_{i_1} u_{i_1} + \Delta t[K^{-}_{i_1 i_2}(u_{i_1} - u_{i_2}) + K^{-}_{i_1 i_3}(u_{i_1} - u_{i_3})] \\ S_{i_2} u_{i_2} &\rightarrow S_{i_2} u_{i_2} + \Delta t K^{+}_{i_1 i_2}(u_{i_1} - u_{i_2}) \\ S_{i_3} u_{i_3} &\rightarrow S_{i_3} u_{i_3} + \Delta t K^{+}_{i_1 i_3}(u_{i_1} - u_{i_3}) \, . \end{aligned} \qquad (3.33)$$

The N scheme directs the way the vertices i_1, i_2 and i_3 are chosen according to the inflow edges. Now the contributions from the two edges are gathered together to give the cell T vertices contributions, which allows the overall distribution to be done in a manner similar to that of the PSI scheme (2.58), by imposing linearity preservation on the N scheme, so that

$$(\phi_i^T)^{PSI^{LIM}} = \frac{\left[(\beta_i^T)^{N^{LIM}}\right]^+}{\sum_{j \in T}\left[(\beta_j^T)^{N^{LIM}}\right]^+}(\phi^T)^{LIM} = (\beta_i^T)^{PSI^{LIM}}(\phi^T)^{LIM} \, , \qquad (3.34)$$

where $(\beta_i^T)^{PSI^{LIM}}$ is the limited high order fluctuation and $(\beta_i^T)^{N^{LIM}}$ can be defined using

$$(\phi_i^T)^{N^{LIM}} = (\beta_i^T)^{N^{LIM}}(\phi^T)^{LIM} \, . \qquad (3.35)$$

The limiting of the polynomial in (3.16) ensures that at least one distribution coefficient $(\beta_i^T)^{N^{LIM}}$ within each cell is positive so the denominator in (3.34) is never zero. Also the limiting procedure applied in (3.34) will not increase the magnitude of the distribution coefficients given by (3.35). The restriction on the time step is required by (3.33), and will be discussed in the next section. The limited fluctuation can now be used to produce a high order scheme which is both positive and linearity preserving.

3.5.1 Modified Third Order Abgrall-Roe Scheme

The approximation of the two-dimensional scalar advection equation

$$\frac{\partial u}{\partial t} + \vec{\lambda} \cdot \vec{\nabla} u = 0 \qquad (3.36)$$

using the modified fluctuation splitting schemes will be considered here, for linearly varying $\vec{\lambda}$, and piecewise quadratic u with further restriction to cases where $\vec{\nabla}\cdot\vec{\lambda}=0$, which means that the fluctuation can be written as

$$\phi^T = -\int_T \vec{\lambda}\cdot\vec{\nabla}u\,\mathrm{d}\Omega = -\int_T \vec{\nabla}\cdot\left(\vec{\lambda}u\right)\mathrm{d}\Omega = \oint_{\partial\Omega} u\vec{\lambda}\cdot\vec{n}\,\mathrm{d}\Gamma, \tag{3.37}$$

where $\vec{n}$ is the inward pointing normal to the cell boundary. Using Simpson's rule along each edge of the triangular cells, the fluctuation is exactly

$$\begin{aligned}
\oint_{\partial\Omega} u\vec{\lambda}\cdot\vec{n}\,\mathrm{d}\Gamma &= \frac{1}{6}\left(u_{i_1}\vec{\lambda}_{i_1}\cdot\vec{n}_{i_3} + 4u_{i_1i_2}\vec{\lambda}_{i_1i_2}\cdot\vec{n}_{i_3} + u_{i_2}\vec{\lambda}_{i_2}\cdot\vec{n}_{i_3}\right) \\
&+ \frac{1}{6}\left(u_{i_2}\vec{\lambda}_{i_2}\cdot\vec{n}_{i_1} + 4u_{i_2i_3}\vec{\lambda}_{i_2i_3}\cdot\vec{n}_{i_1} + u_{i_3}\vec{\lambda}_{i_3}\cdot\vec{n}_{i_1}\right) \\
&+ \frac{1}{6}\left(u_{i_3}\vec{\lambda}_{i_3}\cdot\vec{n}_{i_2} + 4u_{i_3i_1}\vec{\lambda}_{i_3i_1}\cdot\vec{n}_{i_2} + u_{i_1}\vec{\lambda}_{i_1}\cdot\vec{n}_{i_2}\right) \\
&= \frac{1}{6}\left[u_{i_1}\vec{\lambda}_{i_1}\cdot\vec{n}_{i_3} + 4\left(\frac{u_{i_1}+u_{i_2}}{2}\right)\vec{\lambda}_{i_1i_2}\cdot\vec{n}_{i_3} + u_{i_2}\vec{\lambda}_{i_2}\cdot\vec{n}_{i_3}\right] \\
&+ \frac{1}{6}\left[4\left(u_{i_1i_2} - \frac{u_{i_1}+u_{i_2}}{2}\right)\vec{\lambda}_{i_1i_2}\cdot\vec{n}_{i_3}\right] \\
&+ \frac{1}{6}\left[u_{i_2}\vec{\lambda}_{i_2}\cdot\vec{n}_{i_1} + 4\left(\frac{u_{i_2}+u_{i_3}}{2}\right)\vec{\lambda}_{i_2i_3}\cdot\vec{n}_{i_1} + u_{i_3}\vec{\lambda}_{i_3}\cdot\vec{n}_{i_1}\right] \\
&+ \frac{1}{6}\left[4\left(u_{i_2i_3} - \frac{u_{i_2}+u_{i_3}}{2}\right)\vec{\lambda}_{i_2i_3}\cdot\vec{n}_{i_1}\right] \\
&+ \frac{1}{6}\left[u_{i_3}\vec{\lambda}_{i_3}\cdot\vec{n}_{i_2} + 4\left(\frac{u_{i_3}+u_{i_1}}{2}\right)\vec{\lambda}_{i_3i_1}\cdot\vec{n}_{i_2} + u_{i_1}\vec{\lambda}_{i_1}\cdot\vec{n}_{i_2}\right] \\
&+ \frac{1}{6}\left[4\left(u_{i_3i_1} - \frac{u_{i_3}+u_{i_1}}{2}\right)\vec{\lambda}_{i_3i_1}\cdot\vec{n}_{i_2}\right]
\end{aligned} \tag{3.38}$$

where i_1, i_2 and i_3 are the three vertices of the triangle.

For linear $\vec{\lambda}$ and u when $\vec{\nabla}\cdot\vec{\lambda}=0$, the fluctuations are

$$\begin{aligned}
\oint_{\partial\Omega} u\vec{\lambda}\cdot\vec{n}\,\mathrm{d}\Gamma &= \frac{1}{6}\left(u_{i_1}\vec{\lambda}_{i_1}\cdot\vec{n}_{i_3}+4u_{i_1i_2}\vec{\lambda}_{i_1i_2}\cdot\vec{n}_{i_3}+u_{i_2}\vec{\lambda}_{i_2}\cdot\vec{n}_{i_3}\right) \\
&+ \frac{1}{6}\left(u_{i_2}\vec{\lambda}_{i_2}\cdot\vec{n}_{i_1}+4u_{i_2i_3}\vec{\lambda}_{i_2i_3}\cdot\vec{n}_{i_1}+u_{i_3}\vec{\lambda}_{i_3}\cdot\vec{n}_{i_1}\right) \\
&+ \frac{1}{6}\left(u_{i_3}\vec{\lambda}_{i_3}\cdot\vec{n}_{i_2}+4u_{i_3i_1}\vec{\lambda}_{i_3i_1}\cdot\vec{n}_{i_2}+u_{i_1}\vec{\lambda}_{i_1}\cdot\vec{n}_{i_2}\right) \\
&= \frac{1}{6}\left[u_{i_1}\vec{\lambda}_{i_1}\cdot\vec{n}_{i_3}+4\left(\frac{u_{i_1}+u_{i_2}}{2}\right)\vec{\lambda}_{i_1i_2}\cdot\vec{n}_{i_3}+u_{i_2}\vec{\lambda}_{i_2}\cdot\vec{n}_{i_3}\right] \\
&+ \frac{1}{6}\left[u_{i_2}\vec{\lambda}_{i_2}\cdot\vec{n}_{i_1}+4\left(\frac{u_{i_2}+u_{i_3}}{2}\right)\vec{\lambda}_{i_2i_3}\cdot\vec{n}_{i_1}+u_{i_3}\vec{\lambda}_{i_3}\cdot\vec{n}_{i_1}\right] \\
&+ \frac{1}{6}\left[u_{i_3}\vec{\lambda}_{i_3}\cdot\vec{n}_{i_2}+4\left(\frac{u_{i_3}+u_{i_1}}{2}\right)\vec{\lambda}_{i_3i_1}\cdot\vec{n}_{i_2}+u_{i_1}\vec{\lambda}_{i_1}\cdot\vec{n}_{i_2}\right]
\end{aligned} \tag{3.39}$$

where

$$\int_T \vec{\lambda}\cdot\vec{\nabla}u\,\mathrm{d}\Omega = \left(\int_T \vec{\lambda}\,\mathrm{d}\Omega\right)\cdot\vec{\nabla}u = S_T\widetilde{\vec{\lambda}}\cdot\vec{\nabla}u = -\frac{1}{2}\sum_{i\in T} u_i\widetilde{\vec{\lambda}}\cdot\ \vec{n}_i, \tag{3.40}$$

in which $\widetilde{\vec{\lambda}} = (\vec{\lambda}_{i_1}+\vec{\lambda}_{i_2}+\vec{\lambda}_{i_3})/3$. Hence, in the high order case

$$\begin{aligned}
\oint_{\partial\Omega} u\vec{\lambda}\cdot\vec{n}\,\mathrm{d}\Gamma &= -\frac{1}{2}u_{i_1}\widetilde{\vec{\lambda}}\cdot\vec{n}_{i_1}-\frac{1}{2}u_{i_2}\widetilde{\vec{\lambda}}\cdot\vec{n}_{i_2}-\frac{1}{2}u_{i_3}\widetilde{\vec{\lambda}}\cdot\vec{n}_{i_3} \\
&+ \frac{2}{3}\left(u_{i_1i_2}-\frac{u_{i_1}+u_{i_2}}{2}\right)\vec{\lambda}_{i_1i_2}\cdot\vec{n}_{i_3}+\frac{2}{3}\left(u_{i_2i_3}-\frac{u_{i_2}+u_{i_3}}{2}\right)\vec{\lambda}_{i_2i_3}\cdot\vec{n}_{i_1} \\
&+ \frac{2}{3}\left(u_{i_3i_1}-\frac{u_{i_3}+u_{i_1}}{2}\right)\vec{\lambda}_{i_3i_1}\cdot\vec{n}_{i_2}\ .
\end{aligned} \tag{3.41}$$

This will lay the cornerstone for constructing a limited very high order cell fluctuation, which will in turn be distributed to the appropriate mesh vertices. The unlimited fluctuation, by itself, cannot be distributed to the vertices denoted by i_1, i_2 and i_3 in a manner which satisfies the positivity property. Therefore, the interpolated values at the midpoints of the subcell edges, $u_{i_{i_1}i_2}$, $u_{i_{i_2}i_3}$ and $u_{i_{i_3}i_1}$ shown in Figure 3.9, will be limited. The mathematical representation of the limited midpoint values can be written as

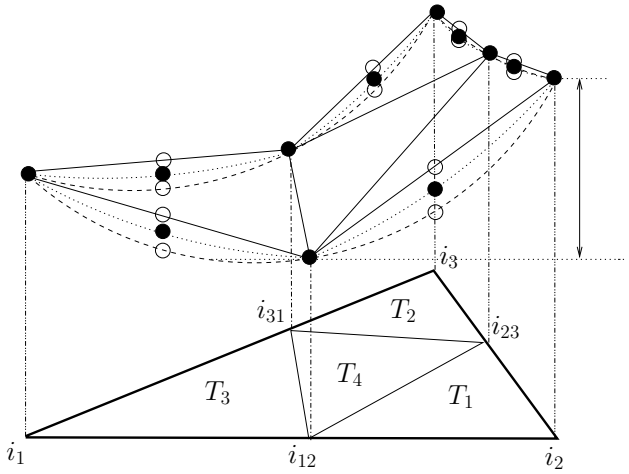

Figure 3.8: The limiting procedure for subtriangle reconstruction, where • show the limited values at the quadrature points, and ∘ indicate the linear and quadratic limits. The solid lines indicate the linear interpolant $\overline{u}(\vec{x})$, the dashed lines indicate the quadratic interpolant $u(\vec{x})$ while the dotted lines are the limited interpolant $u'(\vec{x})$.

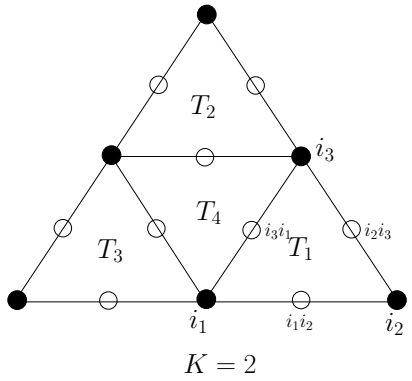

Figure 3.9: The high order reconstruction points of the Abgrall-Roe scheme.

$$
\begin{aligned}
u^{'}_{i_1 i_2} &= \frac{(u_{i_1} + u_{i_2})}{2} + \alpha_{i_1 i_2}(u_{i_1} - u_{i_2}) \\
u^{'}_{i_2 i_3} &= \frac{(u_{i_2} + u_{i_3})}{2} + \alpha_{i_2 i_3}(u_{i_2} - u_{i_3}) \\
u^{'}_{i_3 i_1} &= \frac{(u_{i_3} + u_{i_1})}{2} + \alpha_{i_3 i_1}(u_{i_3} - u_{i_1}) \ ,
\end{aligned} \tag{3.42}
$$

where the coefficients $\alpha_{i_1 i_2}$, $\alpha_{i_2 i_3}$ and $\alpha_{i_3 i_1}$ are defined as

$$
\begin{aligned}
\alpha_{i_1 i_2} &= \max\left(-K, \min\left[K, \frac{u_{i_1 i_2} - \frac{(u_{i_1} + u_{i_2})}{2}}{u_{i_1} - u_{i_2}}\right]\right) \\
\alpha_{i_2 i_3} &= \max\left(-K, \min\left[K, \frac{u_{i_2 i_3} - \frac{(u_{i_2} + u_{i_3})}{2}}{u_{i_2} - u_{i_3}}\right]\right) \\
\alpha_{i_3 i_1} &= \max\left(-K, \min\left[K, \frac{u_{i_3 i_1} - \frac{(u_{i_3} + u_{i_1})}{2}}{u_{i_3} - u_{i_1}}\right]\right)
\end{aligned} \tag{3.43}
$$

in which division by zero is avoided by making sure the denominator does not become zero. Here, $u^{'}_{i_1 i_2}$, $u^{'}_{i_2 i_3}$ and $u^{'}_{i_3 i_1}$ are the limited midpoint values as shown in Figure 3.8, indicated by the filled circles on the dotted lines. These are based on (3.16), and satisfy

$$
\begin{aligned}
\left| u^{'}_{i_1 i_2} - \frac{(u_{i_1} + u_{i_2})}{2} \right| &\leq K \left| u_{i_1} - u_{i_2} \right| \\
\left| u^{'}_{i_2 i_3} - \frac{(u_{i_2} + u_{i_3})}{2} \right| &\leq K \left| u_{i_2} - u_{i_3} \right| \\
\left| u^{'}_{i_3 i_1} - \frac{(u_{i_3} + u_{i_1})}{2} \right| &\leq K \left| u_{i_3} - u_{i_1} \right|
\end{aligned} \tag{3.44}
$$

where the value of $K \geq 0$ will be chosen appropriately. To guarantee that the above relation holds at all the quadrature points, the high order polynomial will be limited. The best choice for K is an open question but three significant values are given in the previous Section 3.5. The positive time-step restriction depends on K and decreases as K increases. The appropriate choice of K is very important because the precise calculation of the coefficients $\alpha_{i_1 i_2}$, $\alpha_{i_2 i_3}$ and $\alpha_{i_3 i_1}$ for the appropriate edges will be dependent on the value of K. This will allow the fluctuation to be written as,

$$\begin{aligned}\oint_{\partial\Omega} u\vec{\lambda}\cdot\vec{n}\,\mathrm{d}\Gamma &= -\frac{u_{i_1}\widetilde{\vec{\lambda}}\cdot\vec{n_{i_1}}}{2}-\frac{u_{i_2}\widetilde{\vec{\lambda}}\cdot\vec{n_{i_2}}}{2}-\frac{u_{i_3}\widetilde{\vec{\lambda}}\cdot\vec{n_{i_3}}}{2} \\ &+ \frac{2\alpha_{i_1i_2}(u_{i_1}-u_{i_2})\vec{\lambda}_{i_1i_2}\cdot\vec{n_{i_3}}}{3}+\frac{2\alpha_{i_2i_3}(u_{i_2}-u_{i_3})\vec{\lambda}_{i_2i_3}\cdot\vec{n_{i_1}}}{3} \\ &+ \frac{2\alpha_{i_3i_1}(u_{i_3}-u_{i_1})\vec{\lambda}_{i_3i_1}\cdot\vec{n_{i_2}}}{3}\,. \end{aligned} \tag{3.45}$$

Returning to the linear case described in Section 2.5.1, the fluctuation can then be written as

$$\begin{aligned}-\frac{u_{i_1}\widetilde{\vec{\lambda}}\cdot\vec{n_{i_1}}}{2}-\frac{u_{i_2}\widetilde{\vec{\lambda}}\cdot\vec{n_{i_2}}}{2}-\frac{u_{i_3}\widetilde{\vec{\lambda}}\cdot\vec{n_{i_3}}}{2} &= \frac{(u_{i_1}-u_{i_2})\widetilde{\vec{\lambda}}\cdot\vec{n_{i_2}}}{2}+\frac{(u_{i_1}-u_{i_3})\widetilde{\vec{\lambda}}\cdot\vec{n_{i_3}}}{2} \\ &= \phi_{i_1i_2}+\phi_{i_1i_3} \\ &= k_{i_2}(u_{i_1}-u_{i_2})+k_{i_3}(u_{i_1}-u_{i_3})\,, \end{aligned} \tag{3.46}$$

where $k_{i_2}=\frac{1}{2}\widetilde{\vec{\lambda}}\cdot\vec{n_{i_2}}$ and $k_{i_3}=\frac{1}{2}\widetilde{\vec{\lambda}}\cdot\vec{n_{i_3}}$ are of the same sign or zero. The modified fluctuation (3.45) can now be distributed to the vertices in a positive manner, following the analysis of Section 3.5. As will be shown below, the N scheme will assist in guiding the direction in which the modified fluctuation will be distributed.

The N scheme can be viewed as distributing $\phi_{i_1i_2}$ and $\phi_{i_1i_3}$ using (3.23) which is a useful alternative formulation when considering the distribution of the higher order fluctuation. The fluctuation in the limited high order case (3.45), is equal to

$$\begin{aligned}\phi^{LIM} &= \oint_{\partial\Omega} u'\vec{\lambda}\cdot\vec{n}\,\mathrm{d}\Gamma \\ &= \frac{(u_{i_1}-u_{i_2})\widetilde{\vec{\lambda}}\cdot\vec{n_{i_2}}}{2}+\frac{2\alpha_{i_1i_2}(u_{i_1}-u_{i_2})\vec{\lambda}_{i_1i_2}\cdot\vec{n_{i_3}}}{3}-\frac{2\alpha_{i_2i_3}(u_{i_1}-u_{i_2})\vec{\lambda}_{i_2i_3}\cdot\vec{n_{i_1}}}{3} \\ &+ \frac{(u_{i_1}-u_{i_3})\widetilde{\vec{\lambda}}\cdot\vec{n_{i_3}}}{2}-\frac{2\alpha_{i_3i_1}(u_{i_1}-u_{i_3})\vec{\lambda}_{i_3i_1}\cdot\vec{n_{i_2}}}{3}+\frac{2\alpha_{i_2i_3}(u_{i_1}-u_{i_3})\vec{\lambda}_{i_2i_3}\cdot\vec{n_{i_1}}}{3} \\ &= K_{i_1i_2}(u_{i_1}-u_{i_2})+K_{i_1i_3}(u_{i_1}-u_{i_3})\,, \end{aligned} \tag{3.47}$$

since $\vec{n_{i_1}}=-\vec{n_{i_2}}-\vec{n_{i_3}}$ and

$$u_j-u_k\equiv(u_j-u_i)+(u_i-u_k)\equiv(u_i-u_k)-(u_i-u_j)\,. \tag{3.48}$$

The limited high order fluctuations (3.47) can be seen to have a similar form to the N scheme fluctuations (3.46). Now if $K_{i_1 i_2}$ has the same sign as k_{i_2}, sending $K_{i_1 i_2}(u_{i_1} - u_{i_2})$ to the same node as $k_{i_2}(u_{i_1} - u_{i_2})$ will lead to a locally positive distribution. If they are of a different sign, then sending $K_{i_1 i_2}(u_{i_1} - u_{i_2})$ to the node opposite that updated by $k_{i_2}(u_{i_1} - u_{i_2})$ on edge $i_1 i_2$, leads to an update which is locally positive. However, note that when $\widetilde{\vec{\lambda}} \cdot \vec{n_{i_2}} = 0$ or $\widetilde{\vec{\lambda}} \cdot \vec{n_{i_3}} = 0$ in (3.46), the split between nodes in (3.47) is not unique and leads to a situation where the fluctuation can be arbitrarily distributed to either node in the high order distribution. This does not seem to have any detrimental effect on the numerical results. The new scheme can be written in a form similar to (3.31), which will lead to a positive distribution. Since the fluctuation can also be written as (3.32), the distribution (3.31) is equivalently given as

$$\begin{aligned} S_{i_1} u_{i_1} &\rightarrow S_{i_1} u_{i_1} + \Delta t [K^-_{i_1 i_2}(u_{i_1} - u_{i_2}) + K^-_{i_1 i_3}(u_{i_1} - u_{i_3})] \\ S_{i_2} u_{i_2} &\rightarrow S_{i_2} u_{i_2} + \Delta t K^+_{i_1 i_2}(u_{i_1} - u_{i_2}) \\ S_{i_3} u_{i_3} &\rightarrow S_{i_3} u_{i_3} + \Delta t K^+_{i_1 i_3}(u_{i_1} - u_{i_3}) \end{aligned} \tag{3.49}$$

where $[\,]^+$ and $[\,]^-$ are the positive and the negative parts of the argument, and the vertices i_1, i_2 and i_3 are chosen according to the inflow edges, as directed by the N scheme. This scheme is clearly locally positive for

$$\Delta t \leq \min \left(\frac{-S_{i_1}}{K^-_{i_1 i_2} + K^-_{i_1 i_3}}, \frac{S_{i_2}}{K^+_{i_1 i_2}}, \frac{S_{i_3}}{K^+_{i_1 i_3}} \right) . \tag{3.50}$$

Now the overall distribution is done in a manner similar to that of the PSI scheme (2.58), by imposing linearity preservation on the N scheme, so that

$$(\phi_i^T)^{PSI^{LIM}} = \frac{\left[(\beta_i^T)^{N^{LIM}} \right]^+}{\sum_{j \in T} \left[(\beta_j^T)^{N^{LIM}} \right]^+} \phi_T^{LIM} = (\beta_i^T)^{PSI^{LIM}} \phi_T^{LIM} \tag{3.51}$$

where $(\beta_j^T)^{N^{LIM}}$ is the limited high order fluctuation and $(\beta_i^T)^{N^{LIM}}$ can be defined using

$$(\phi_i^T)^{N^{LIM}} = (\beta_i^T)^{N^{LIM}} \phi_T^{LIM} . \tag{3.52}$$

The limiting of the polynomial ensures that at least one distribution coefficient within each cell is positive. Also the limiting procedure applied in (3.51) will not increase the magnitude of the distribution coefficients given by (3.52).

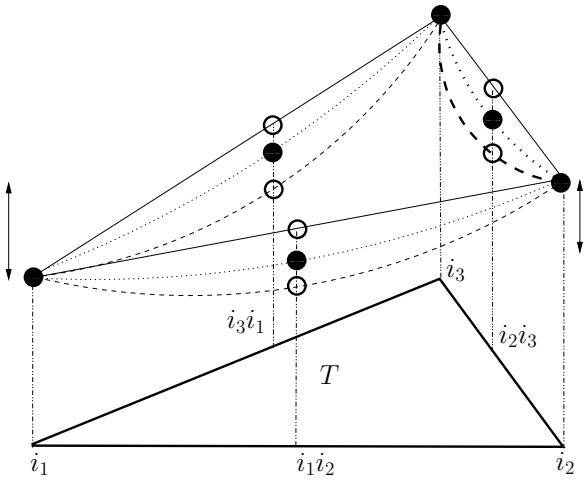

Figure 3.10: The limiting procedure for Caraeni's scheme gradient recovery, where • show the limited values at the quadrature points, and ∘ indicate the linear and quadratic limits. The solid lines indicate the linear interpolant $\overline{u}(\vec{x})$, the dashed lines indicate the quadratic interpolant $u(\vec{x})$ and the dotted lines are the limited interpolant $u^{'}(\vec{x})$.

3.5.2 Caraeni's Scheme

The implementation of the technique for imposing positivity on Caraeni's scheme is carried out using the edge midpoint values (3.10), so that it is possible to construct $u^{'}_{i_1i_2}$, $u^{'}_{i_2i_3}$ and $u^{'}_{i_3i_1}$, the limited midpoint values along each edge, as shown in Figure 3.10, indicated by the filled circles. As already discussed in Section 3.5, the limiting procedure is exactly the same for all higher than second order schemes, and the limited high order fluctuation for Caraeni's scheme can also be written in the form (3.47), i.e.

$$\phi^{CAR^{LIM}} = \oint_{\partial\Omega} u\vec{\lambda}\cdot\vec{n}\,\mathrm{d}\Gamma = K_{i_1i_2}(u_{i_1}-u_{i_2}) + K_{i_1i_3}(u_{i_1}-u_{i_3})\ . \tag{3.53}$$

This limited high order fluctuation can now be distributed in a similar manner to that of the PSI scheme (2.58), i.e.

$$(\phi_i^T)^{CAR^{LIM}} = \frac{\left[(\beta_i^T)^{N^{LIM}}\right]^+}{\Sigma_{j\in T}\left[(\beta_j^T)^{N^{LIM}}\right]^+}\phi_T^{CAR^{LIM}} = (\beta_i^T)^{PSI^{LIM}}\phi_T^{CAR^{LIM}}\ . \tag{3.54}$$

Constructing a positive higher than second order scheme is therefore also possible for Caraeni's scheme, because the limiting procedure will not allow the distribution coefficient to be larger in magnitude than that of the underlying positive scheme (3.49).

3.5.3 The Positive Additional Neighbouring Nodes Scheme

The LDA distribution coefficients, as stated previously in Section 3.4, do not distribute the high order fluctuation of the additional neighbouring nodes scheme in a positivity preserving manner. As with the approach proposed by Caraeni [17], which constructed a high order fluctuation within each cell and then distributed it using the LDA distribution coefficients, the additional neighbouring nodes scheme also cannot guarantee the absence of spurious oscillation from the flow without the application of an additional smoothing stage. The modification outlined earlier in this section can be used to guarantee the absence of spurious oscillations. Once again, by modifying the high order interpolant and using a limiting procedure it is possible to distribute the limited fluctuation in a positivity preserving manner, so that the spurious oscillations can be overcome in exactly the same way as for Abgrall-Roe and Caraeni's schemes. The implementation of this technique starts by using quadrature to evaluate the fluctuation over the mesh cell, not the subcell used in Section 3.5, so the limited solution value at a given edge midpoint, such as $i_1 i_2$, is given as

$$u'_{i_1 i_2} = \frac{(u_{i_1} + u_{i_2})}{2} + \alpha_{i_1 i_2}(u_{i_1} - u_{i_2}) \ , \tag{3.55}$$

where, as in (3.21)

$$\alpha_{i_1 i_2} = \max\left(-K, \min\left[K, \frac{u_{i_1 i_2} - \frac{(u_{i_1}+u_{i_2})}{2}}{u_{i_1} - u_{i_2}}\right]\right) \ . \tag{3.56}$$

This limiting procedure is exactly the same as discussed earlier, and the limited high order fluctuation can again be written as

$$\phi^{ANN^{LIM}} = \oint_{\partial\Omega} u\vec{\lambda}\cdot\vec{n}\,\mathrm{d}\Gamma = K_{i_1 i_2}(u_{i_1} - u_{i_2}) + K_{i_1 i_3}(u_{i_1} - u_{i_3}) \ . \tag{3.57}$$

It will be distributed in the same manner that created the PSI scheme (2.58), i.e.

$$(\phi_i^T)^{ANN^{LIM}} = \frac{\left[(\beta_i^T)^{N^{LIM}}\right]^+}{\sum_{j\in T}\left[(\beta_j^T)^{N^{LIM}}\right]^+}\phi_T^{ANN^{LIM}} = (\beta_i^T)^{PSI^{LIM}}\phi_T^{ANN^{LIM}} \ . \tag{3.58}$$

As discussed in Section 3.5.1, like the PSI scheme, the limiting procedure will produce distribution coefficients which will not be larger in magnitude than those of the underlying positive scheme, so a positive third order additional neighbouring nodes scheme is achieved.

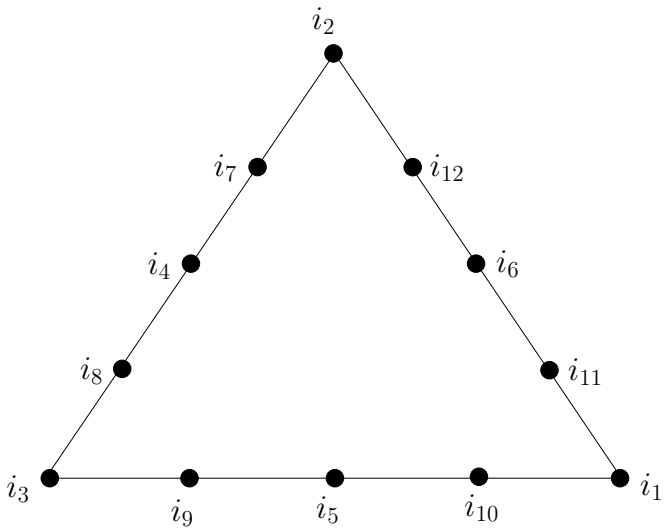

Figure 3.11: The quadrature points used in integration along each cell edge

3.6 Burgers' Equation

The simple extension of the high order schemes, described in the previous chapter, to nonlinear equations will be outlined here. The analysis follows [41] . A two-dimensional variant of Burgers' equation is used to exemplify a nonlinear equation, and is given in (2.67). In order to evaluate the high order fluctuation for the positive high order schemes, Burgers' equation needs a suitable q_p point quadrature along each cell edge, since Simpson's rule is not accurate enough to be used for evaluating the fluctuation, as was the case in the linear advection equation. Once the appropriate quadrature points are chosen, it is possible to write the fluctuation as

$$\begin{aligned} \oint_{\partial\Omega} \vec{f}\cdot\vec{n}\,\mathrm{d}\Gamma &= \sum_{edges}\left(\sum_{l=1}^{q_p}\omega^l\,\vec{f}(u^l)\cdot\vec{n}\right)_e \\ &= \sum_{edges}\left(\sum_{l=1}^{q_p}\omega^l\,\vec{f}(\bar{u}^l)\cdot\vec{n}\right)_e + \sum_{edges}\left(\sum_{l=1}^{q_p}\omega^l\left(\vec{f}(u^l)-\vec{f}(\bar{u}^l)\right)\cdot\vec{n}\right)_e \end{aligned} \tag{3.59}$$

where ω^l are the quadrature weight coefficients and $\bar{u}$ is the value of the linear interpolant of u at the quadrature points along the cell edges. One can observe that the above equation now comprises a difference in the flux, which can be handled in a similar manner to a standard finite volume scheme, whenever a suitable Roe linearisation exists [70], and can therefore be written

$$\vec{f}(u) - \vec{f}(\bar{u}) = \widetilde{\frac{\partial \vec{f}}{\partial u}}(u - \bar{u}) = \widetilde{\vec{\lambda}}(u - \bar{u}) \; . \tag{3.60}$$

The advection velocity, $\widetilde{\vec{\lambda}} = ((u+\bar{u})/2, 1)^T$, now also depends on the limited polynomial interpolant. However, because the polynomial interpolant is limited in the same way as in the linear advection equation, there is only a small extra procedure involved. For example, the limiting along a given edge $i_1 i_2$ in Figure 3.11 is carried out by setting

$$\begin{aligned} u'_{i_{11}} &= \frac{(3u_{i_1} + u_{i_2})}{4} + \alpha_{i_{11}}(u_{i_1} - u_{i_2}) \\ u'_{i_6} &= \frac{(u_{i_1} + u_{i_2})}{2} + \alpha_{i_6}(u_{i_1} - u_{i_2}) \\ u'_{i_{12}} &= \frac{(u_{i_1} + 3u_{i_2})}{4} + \alpha_{i_{12}}(u_{i_1} - u_{i_2}) \; , \end{aligned} \tag{3.61}$$

where the coefficients $\alpha_{i_{11}}$, α_{i_6} and $\alpha_{i_{12}}$ are defined as

$$\begin{aligned} \alpha_{i_{11}} &= \max\left(-K, \min\left[K, \frac{u_{i_{11}} - \frac{(3u_{i_1} + u_{i_2})}{4}}{u_{i_1} - u_{i_2}}\right]\right) \\ \alpha_{i_6} &= \max\left(-K, \min\left[K, \frac{u_{i_6} - \frac{(u_{i_1} + u_{i_2})}{2}}{u_{i_1} - u_{i_2}}\right]\right) \\ \alpha_{i_{12}} &= \max\left(-K, \min\left[K, \frac{u_{i_{12}} - \frac{(u_{i_1} + 3u_{i_2})}{4}}{u_{i_1} - u_{i_2}}\right]\right) \end{aligned} \tag{3.62}$$

in which division by zero is carefully avoided. Now, the advection velocities, required by (3.60) along the same edge $i_1 i_2$, depend on the limited polynomial interpolant, and are defined by

$$\begin{aligned}
\widetilde{\vec{\lambda}}_{i_{11}} &= \left(\frac{u'_{i_{11}} + \frac{3(u_{i_1}+u_{i_2})}{4}}{2}, 1 \right)^T \\
\widetilde{\vec{\lambda}}_{i_6} &= \left(\frac{u'_{i_6} + \frac{3(u_{i_1}+u_{i_2})}{2}}{2}, 1 \right)^T \\
\widetilde{\vec{\lambda}}_{i_{12}} &= \left(\frac{u'_{i_{12}} + \frac{(u_{i_1}+3u_{i_2})}{4}}{2}, 1 \right)^T .
\end{aligned} \tag{3.63}$$

Similar expressions are used to calculate the advection velocities in (3.60) for the other edges, i_2i_3 and i_3i_1. One needs to be careful to make sure the solution is bounded so as to maintain positivity, because here the time step limit will now depend on the solution. Given the above information, the fluctuation for the nonlinear scalar equation can now be written as

$$\oint_{\partial\Omega} \vec{f} \cdot \vec{n} \, \mathrm{d}\Gamma = \phi^{LO} + \sum_{edges} \left(\sum_{l=1}^{q_p} \omega^l (u^l - \vec{u}^l) \widetilde{\vec{\lambda}} \cdot \vec{n} \right)_e . \tag{3.64}$$

This now follows the same procedure as in the linear advection case, except that the additional quadrature points will be used in the integration along each cell edges when evaluating the fluctuation. Again one needs to be careful in keeping the advection velocity bounded so as to achieve a positive scheme by using a suitable time step limit, which makes it possible to limit the interpolant in the same way as in the linear advection.

3.7 Results

The same uniformly structured and genuinely unstructured triangular meshes that were used in Chapter 2 will also be used for circular advection of a discontinuous solution profile (test case A), cosine squared profile (test case B) and a smooth solution (test case C), the test cases shown in Figures 2.11, 2.12 and 2.10 respectively. The modified positive schemes discussed in Sections 3.5.1, 3.5.2 and 3.5.3 will be known as the Abgrall-Roe PSI scheme when the non-oscillatory modification it is applied to the Abgrall-Roe scheme, ANN PSI scheme when it is applied to the ANN scheme and Caraeni PSI scheme when it is applied to Caraeni's scheme. The structured and genuinely unstructured triangular meshes mentioned above are used to obtain results with the Caraeni, ANN, Caraeni PSI and ANN PSI schemes. A uniformly subdivided genuinely unstructured triangular mesh,

Schemes	Test Case A	Test Case B	Test Case C		
	min (u)	max (u) outflow	L_1 order	L_2 order	L_∞ order
Abgrall-Roe	-0.0648	0.9703	2.52	1.98	1.47
Abgrall-Roe PSI	0.0000	0.9163	2.69	2.32	2.31
Caraeni	-0.1683	0.9999	3.03	2.62	2.04
Caraeni PSI	0.0000	0.9285	3.48	2.73	1,25
ANN	-0.1896	1.0000	2.55	2.31	2.08
ANN PSI	0.0000	0.8947	2.64	2.38	2.17

Table 3.1: Oscillation and accuracy measures. Mesh type A was used for accuracy. The first two columns have been obtained on the 3806 node and subdivided 984 node meshes shown in Figures 2.10 and 3.12 respectively.

Schemes	Test Case C		
	L_1 order	L_2 order	L_∞ order
Abgrall-Roe	2.49	1.92	1.41
Abgrall-Roe PSI	2.63	2.28	2.26
Caraeni	2.97	2.58	1.98
Caraeni PSI	3.41	2.67	1.19
ANN	2.50	2.29	2.03
ANN PSI	2.59	2.32	2.11

Table 3.2: Accuracy measures on grid type B.

created from a coarser mesh to give a similar number of unknowns and shown in Figure 3.12, will be used to obtain results with the Abgrall-Roe based schemes for the same test cases, described above. Subdivided meshes derived from the uniformly structured meshes shown in Figures 2.11 and 2.12, will also be used to obtain results with the Abgrall-Roe based schemes which demonstrate their accuracy.

A regular structured mesh with 2145 vertices shown in Figure 2.11 are used for test cases A, B and C to obtain results with the third and fourth order ANN PSI scheme.

For test case A, which was outlined in Section 2.6, the most interesting aspect is that it will show whether the schemes presented in this chapter satisfy the positivity property, as

Schemes	Test Case C		
	L_1 order	L_2 order	L_∞ order
3rd order ANN PSI	2.59	2.32	2.11
4th order ANN PSI	3.36	2.91	2.58

Table 3.3: Accuracy measures on grid type A.

oscillations will be visible close to the discontinuities if they don't. None of the modified positive schemes produce any unphysical oscillations.

Figure 3.13 shows the Abgrall-Roe third order scheme, with very small oscillations visible at the discontinuities near to the inflow boundary, arising from the non-positivity issue discussed in Section 3.2.1. For the modified Abgrall-Roe scheme, Figure 3.16 shows that the oscillations have clearly been removed, and the maximum and minimum solution values are the same as the exact solution, to machine precision. For Caraeni's scheme Figure 3.14 shows a significant amount of oscillation which is clearly visible close to the discontinuities, and also some oscillation visible at the outflow boundary (especially around the minimum values). The Caraeni PSI scheme, like the Abgrall-Roe PSI scheme has no oscillations, and the maximum and minimum solution values are recreated exactly as Figure 3.17 exhibits.

For the ANN scheme, derived from extending the stencil, Figure 3.15 shows some oscillations that are visible close to discontinuities with a similar pattern to that of Caraeni's scheme, Figure 3.13. As expected the ANN PSI scheme gives results which are positive and the maximum and minimum solution values are the same as the exact solutions. Based on the results discussed above it is possible to say that the PSI-based schemes are better when discontinuities occur. In all cases the results are significantly better than those of the PSI scheme. Note that the semi circular shape of the solution is completely respected in each test case. For this test case, a comparison of the solutions at the outflow, where the solution is at its maximum, are provided in Figure 3.19, along with a comparison between all the positive high order schemes. This confirms the observations made above.

Figure 3.26 shows the third and fourth order ANN PSI schemes applied on the regular structured mesh with 2145 vertices shown in Figure 2.11. The comparison of the two solutions at the outflow are also shown in Figure 3.28. As in the third order ANN PSI scheme, the fourth order ANN PSI scheme clearly doesn't show any oscillation at the discontinuities and a zoom of the solution where the solution is maximum also shows an improvement.

Test case B, illustrates each scheme's capacity to maintain a smooth peak value without artificially steepening the profile, as already mentioned in Section 2.6. Figure 3.13 shows the third order Abgrall-Roe scheme, with slight oscillations at the outflow profile and some improvement in accuracy compared to the low order schemes, which is also apparent from the outflow profile shown in Figure 3.20. The Abgrall-Roe PSI scheme has clearly removed the small oscillations which were present in the basic Abgrall-Roe scheme, at the cost of a slight drop in peak value seen in Figure 3.16. Caraeni's scheme, shown in Figure 3.14, produces more oscillations in the outflow profile compared to the

Abgrall-Roe scheme. However, Figure 3.17 shows that the Caraeni PSI scheme completely removes the oscillations, again at the expense of a slight drop in peak value. As with the previous non-positive schemes, the ANN scheme also produce slight oscillations at the outflow profile (shown in Figure 3.15). The maximum solution at the outflow for the modified ANN PSI scheme shown in Figure 3.18 produces a slight drop in peak value which is consistent with the Caraeni PSI and Abgrall-Roe PSI schemes. For all the schemes discussed above, the comparison of the solutions at the outflow is provided in Figure 3.20.

Table 3.1 and 3.2 show results obtained using a uniform unstructured mesh shown in Figure 3.12 for Abgrall-Roe based schemes, and all the schemes except the Abgrall-Roe based schemes using the mesh shown in Figure 2.10. The tables identify the minimum value for test case A and the maximum value for test case B, and confirm the observations stated above.

The third and fourth order ANN PSI scheme results are shown in Figure 3.27. Figure 3.29 shows the solution comparisons at the outflow. Neither scheme produces oscillations at the discontinuities, and a zoom of the solution around the outflow where the solution is maximum clearly shows that an increase of the formal accuracy of the scheme does improve the result.

Test case C, which was also introduced in Section 2.6, is used to test the order of accuracy of the schemes using the same circular advection velocity as the above two test cases, but with a smoother solution profile. Figure 3.21, shows the zoom of the solutions at outflow obtained using genuinely unstructured meshes. The results obtained for the different schemes are similar to those of test case B, but the smooth peak values at the outflow are much more close to the exact solution.

All the oscillation and accuracy measures calculated are summarised in Table 3.1 and on the left of Figures 3.22, 3.23 and 3.24 for mesh type A, and Table 3.2 and on the right of Figures 3.22, 3.23 and 3.24 for mesh type B.

The accuracy measures are calculated using structured triangular meshes of the form shown in Figures 2.11 and 2.12, by repeatedly halving the background mesh size, so that it is possible to see the rate at which the error will reduce as finer meshes are used, starting from a coarser one. Here, a sequence of six structured meshes with 561, 2145, 8385, 33153, 131841 and 525825 vertices are used.

For the smooth test case Caraeni's scheme is the most accurate of all the schemes outlined in this thesis, since it uses an LDA distribution which is known to be more accurate than the PSI scheme for smooth solutions, where achieving high accuracy is more important than dealing with the slight oscillations that may occur. Based on this fact it is

possible to say that for smooth solutions, where achieving high accuracy is more important than dealing with small oscillations that may be present, using an LDA-type scheme is a logical choice. Even though the reasons are not very clear yet the ANN scheme, which also uses an LDA distribution, produces a less accurate result than Caraeni's scheme, possibly because the ANN scheme reconstructs a quadratic interpolant within each cell using more information from the surrounding cells, especially for the boundary cells which requires even more information from the surrounding cells. Hence the stencil of the scheme is not local, which may affect the accuracy of the scheme. The Abgrall-Roe scheme also produces a less accurate result than Caraeni's scheme, as it sometimes reverts back to an unstable central distribution at certain nodes, which seems to affect its accuracy.

The tables also show that the modified schemes are less accurate than the schemes based on LDA distribution, but the PSI-based modified schemes are more suitable in dealing with discontinuities, as already discussed for test case A. However, between the modified schemes, the Caraeni PSI scheme is more accurate than Abgrall-Roe PSI and ANN PSI. Even though the Abgrall-Roe PSI scheme produces higher than second order accuracy, the smoothness of the interpolant seems to be affected as the limiting procedure is conducted separately on each of the four subcells. As expected the additional neighbouring nodes PSI scheme achieves higher than second order accuracy. Compared to schemes based on LDA distribution, a slight drop in accuracy for PSI-based schemes for this test case C is to be expected, since the advection velocity is not constant in space and the solution profile contains a turning point, which often means that the schemes return to the standard second order scheme.

For an accuracy study conducted on successively refined structured meshes, the L_1, L_2 and L_∞ norms are considered and the results are shown in Figures 3.22 to 3.24. Comparison between the accuracy measures for mesh type A and mesh type B is shown to produce minimal difference, but mesh type A produces a slightly better accuracy than mesh type B, as the mesh connectivity is favourably inclined for this test case. Overall, it is possible to see that all the modified positive schemes produce higher that second order accuracy in L_1 and L_2 norms and, as expected, imposing positivity doesn't necessarily improve the order of accuracy for the smooth test case. However, the Abgrall-Roe PSI scheme shows improved accuracy compared to the original Abgrall-Roe scheme, possibly because the Abgrall-Roe scheme reverts to the central distribution in some cases, which would be unstable if used on its own [41]. The L_∞ norm results in Figure 3.24 illustrate the impact of the Abgrall-Roe scheme reverting back to using the central difference distribution. It is though, still possible to see the accuracy improve as the mesh is refined, for the L_∞ norm. For third order and fourth order ANN PSI schemes, Table 3.3 shows the summary

of the calculated accuracy measures. Figure 3.31 shows the rate at which the error would decrease as finer meshes are used for L_1, L_2 and L_∞ norms. The figure shows clearly that the fourth order ANN PSI scheme improves its effective accuracy compared to the third order ANN PSI scheme.

The convergence history of all the solutions obtained for the above three test cases are plotted in Figure 3.25. The convergence monitor which has been used is again the root mean square (RMS) of the residual at each time step, as already stated in Section 2.6. It can be seen from the figures that all the schemes converge rapidly to machine accuracy, except the Abgrall-Roe scheme [41]. The rate of convergence to the steady state for the converging schemes is most rapid for the N scheme. For the modified high order schemes, the convergence histories shown are for $K = 0.25$. As the value of K increases the convergence rate slows until it ceases to converge for $K = 0.75$. For $K = 0.5$, the simulation takes more than double the number of iterations to converge compared to $K = 0.25$.

3.7.1 Nonlinear Burgers' Equation

As in the previous chapter, Section 2.7, this test case involves a discontinuous solution of a nonlinear conservation law, represented by the two-dimensional Burgers' equation (2.67). The mesh structures which are used are the genuinely unstructured triangular mesh shown in Figure 2.19, and a uniformly subdivided mesh created from a coarser mesh to give a similar number of unknowns (it has 1933 vertices and is shown in Figure 3.32) on the domain $(x,y) \in [0,1]^2$. The exact solution varies linearly until the intersection point located at $x = \frac{3}{4}$, $y = \frac{1}{2}$, where it then forms a discontinuity which lies inclined to the mesh. All the schemes except the Abgrall-Roe scheme converge to machine accuracy.

The results for the positive high order schemes show that the new limiting procedure completely removes the unphysical oscillations from the high order schemes which were previously not positive. The ANN PSI scheme, shown in Figure 3.34, gives straight iso-lines in the lower triangle, below where the characteristics intersect, and also give a good resolution at the convergence point $(\frac{3}{4}, \frac{1}{2})$. Figure 3.33 shows that the positive Abgrall-Roe PSI and Caraeni PSI schemes also do not produce unphysical oscillations and are able to capture the shock. The high order representation also improves the accuracy of the scheme in the smooth regions compared to the low order schemes. The modified Caraeni PSI scheme, as shown in Figure 3.34, also completely removes the unphysical oscillations and captures the shock accurately.

The plot of the solution cross-sections for $y = 0.75$, where it crosses the discontinuity,

are shown in Figure 3.38. Similarly, the cross-section through $y = 0.25$, which crosses the fan, is shown in Figure 3.35. On the right in both of these figures, a zoom of the "corner" is provided. It is clear to see the improvement in the quality of the solutions with the increase in the order of accuracy. The solutions across the shock, $y = 0.75$, show very little difference between the positive high order schemes, on the other hand the LDA scheme is shown to produce oscillations. For $y = 0.25$, the positive high order schemes produce better quality results, compared to the low order schemes, as seen in the figures.

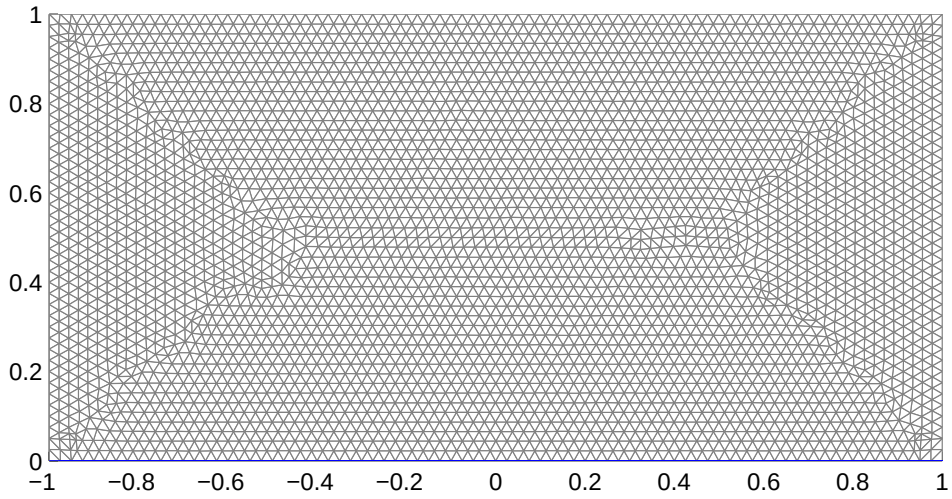

Figure 3.12: The mesh used for the advection results obtained with submesh reconstruction schemes.

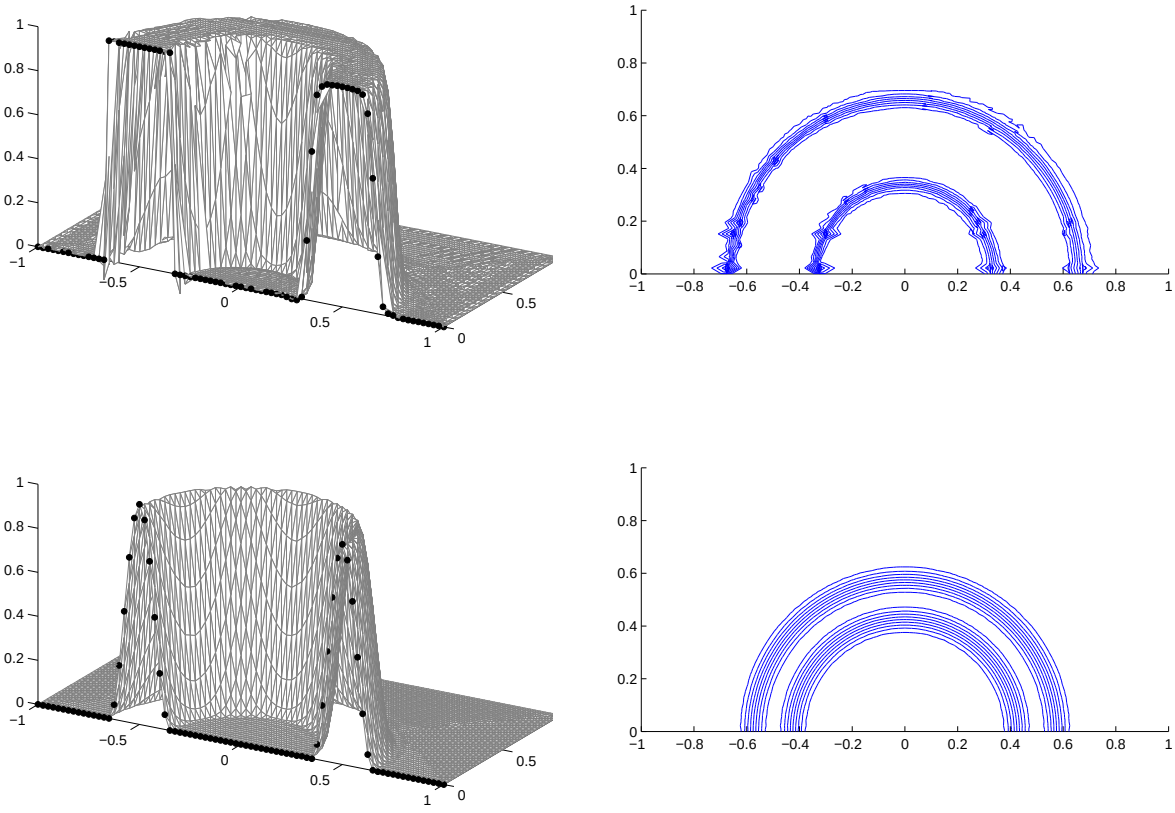

Figure 3.13: Solutions for the Abgrall-Roe scheme applied to the circular advection square wave test case A (top) and cosine squared test case B (bottom).

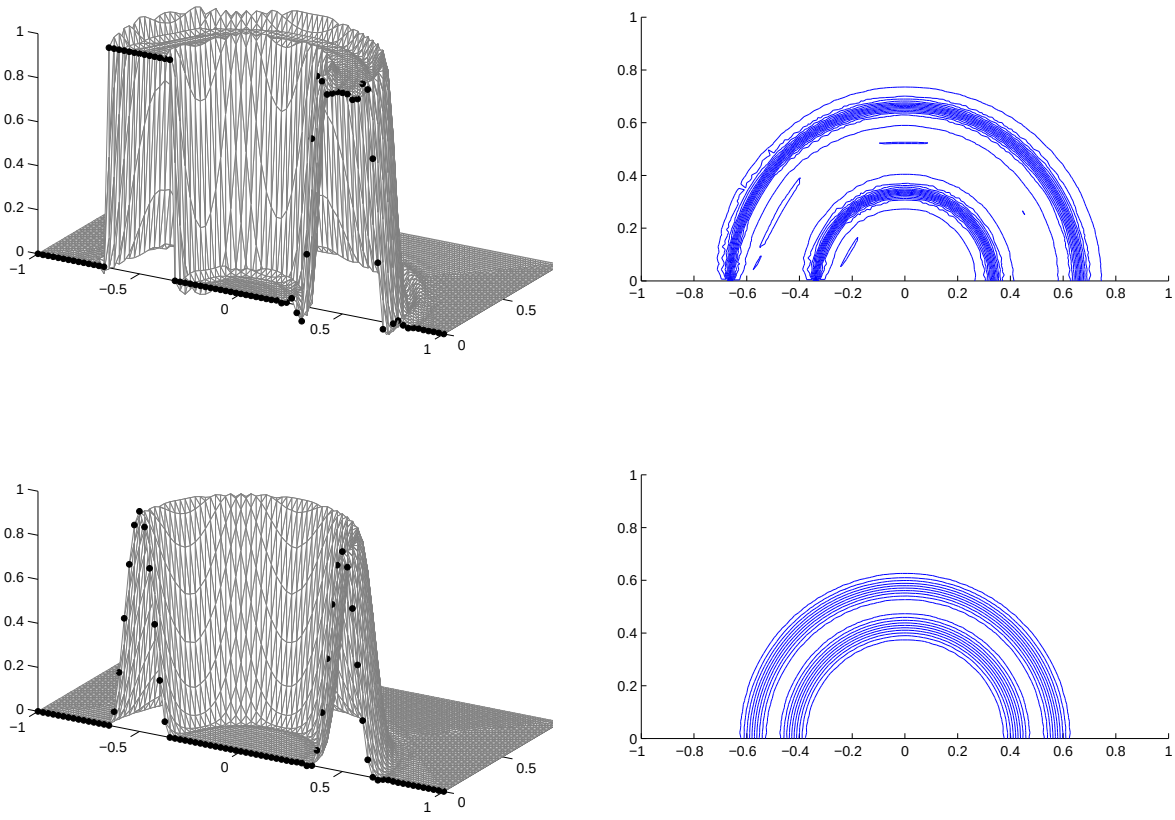

Figure 3.14: Solution for Caraeni's scheme applied to the circular advection square wave test case A (top) and cosine squared test case B (bottom).

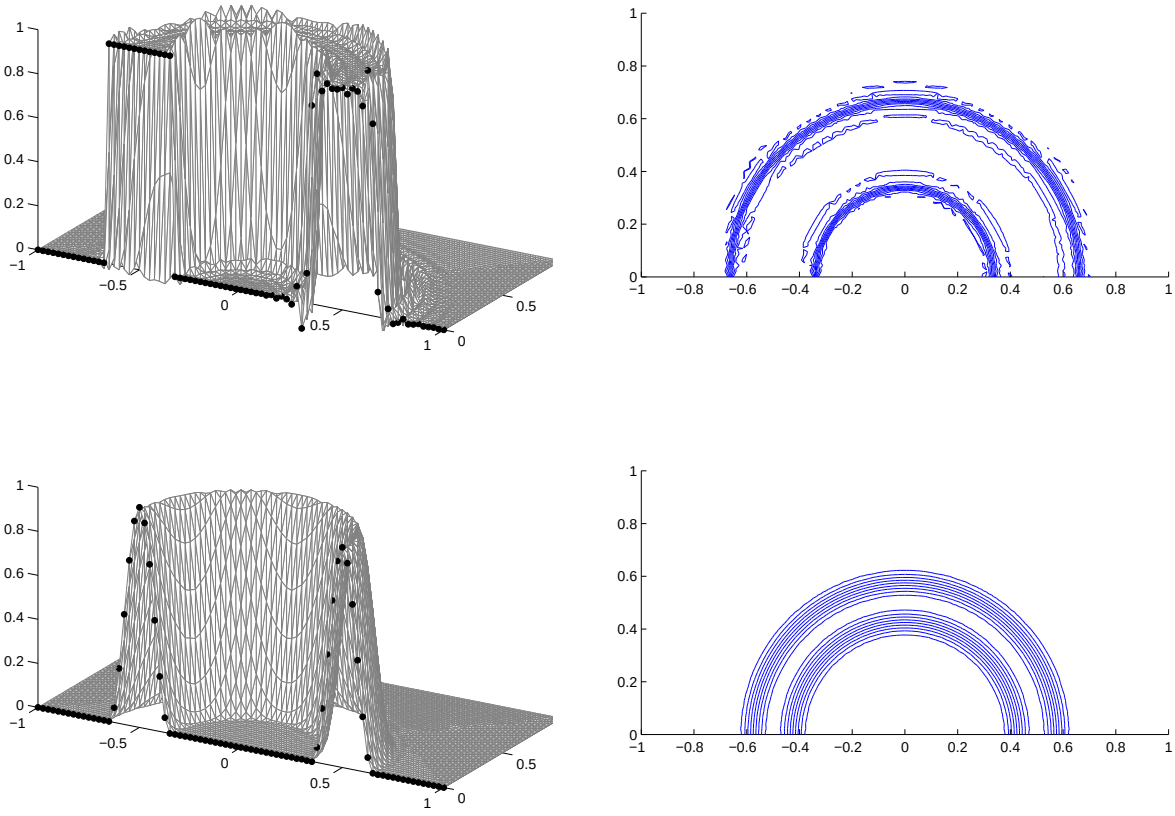

Figure 3.15: Solution for ANN scheme applied to the circular advection square wave test case A (top) and cosine squared test case B (bottom).

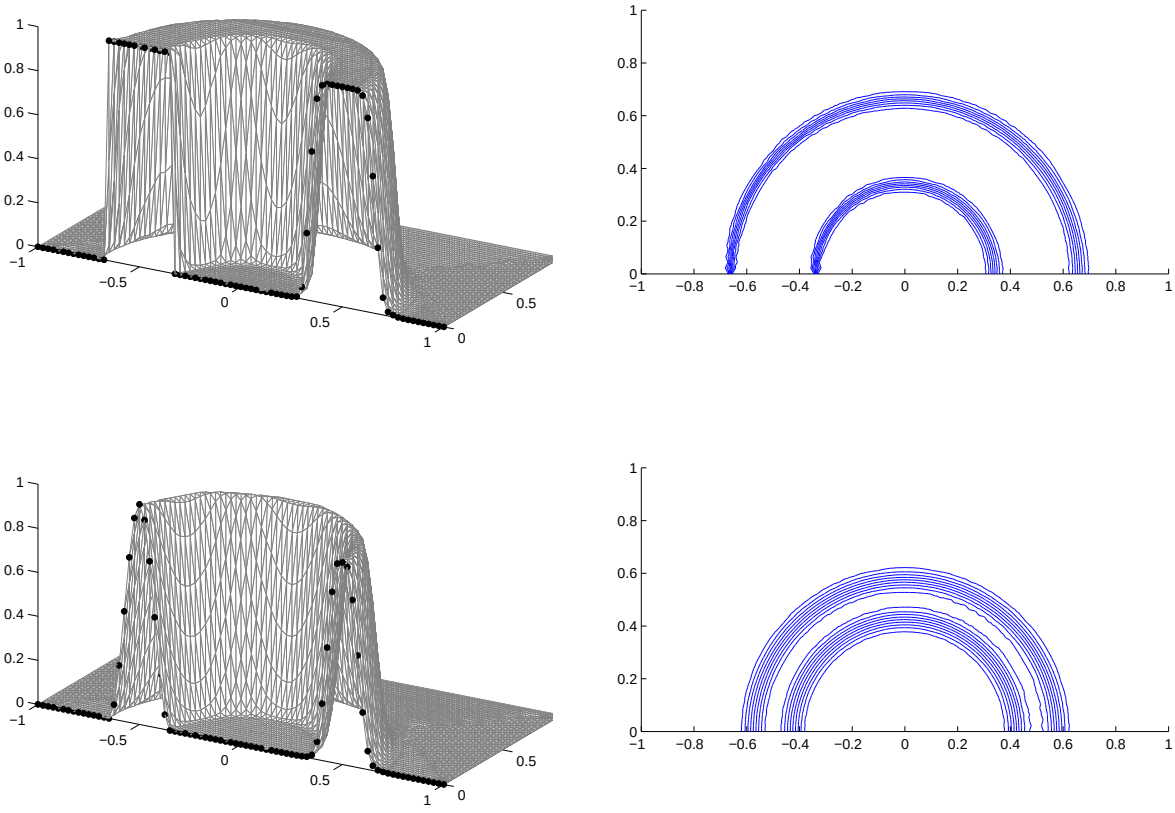

Figure 3.16: Solutions for the Abgrall-Roe PSI scheme applied to the circular advection square wave test case A (top) and cosine squared test case B (bottom).

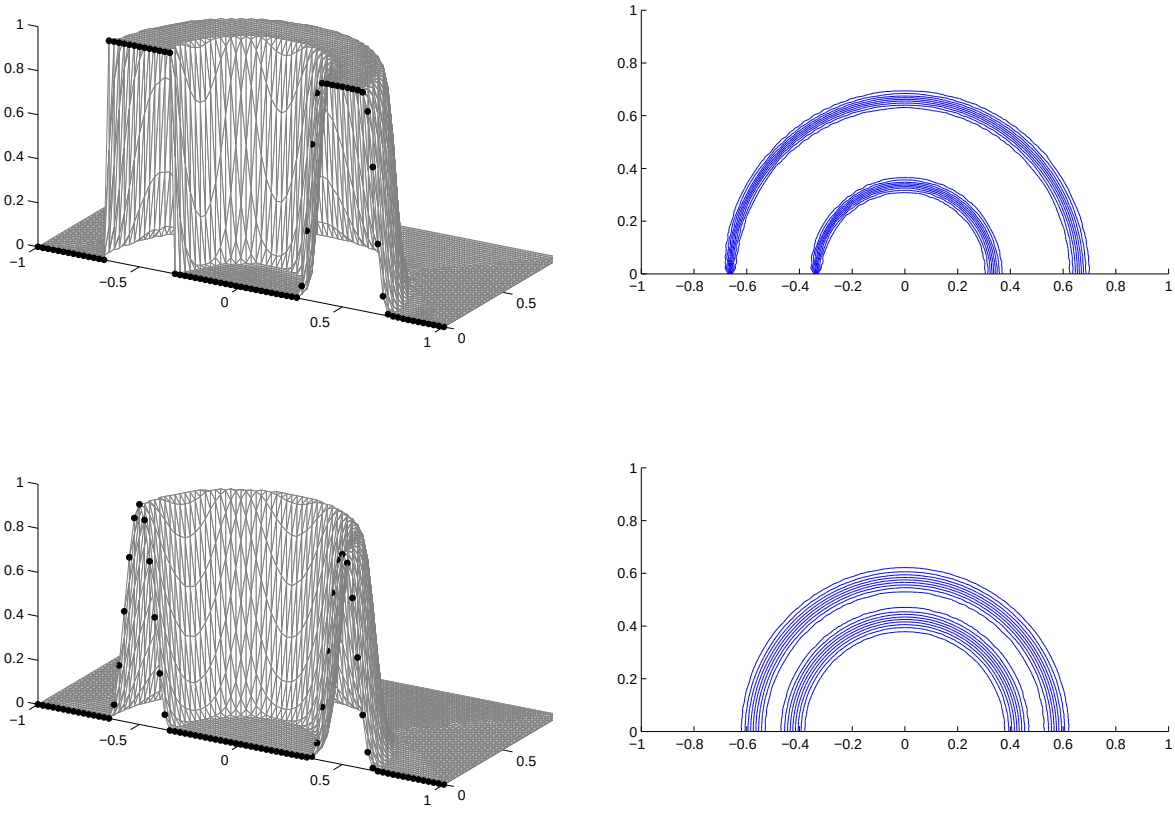

Figure 3.17: Solution for the Caraeni PSI scheme applied to the circular advection square wave test case A (top) and cosine squared test case B (bottom).

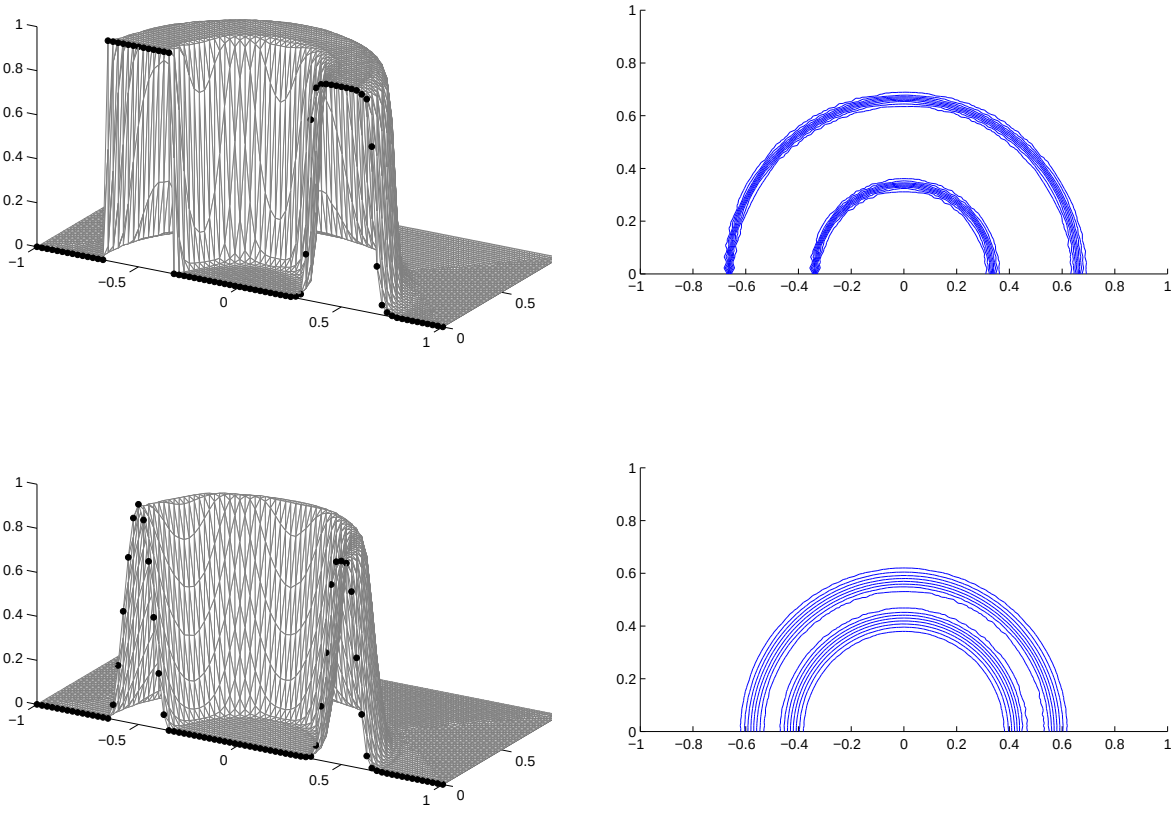

Figure 3.18: Solution for ANN PSI scheme applied to the circular advection square wave test case A (top) and cosine squared test case B (bottom).

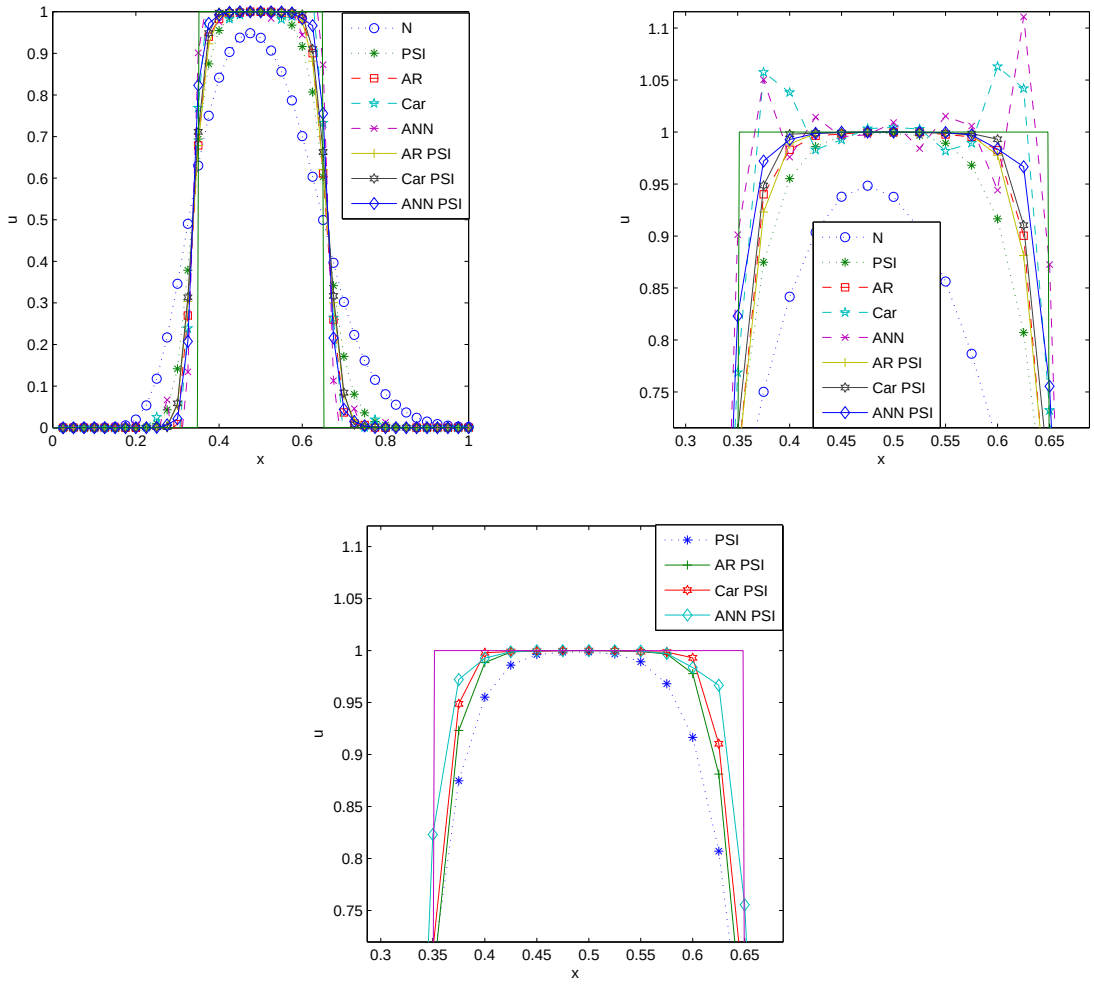

Figure 3.19: Test case A, square wave at outflow (top left), zoom around the maximum (top right) and zoom around all the positive high order schemes (bottom). Solid line is exact solution.

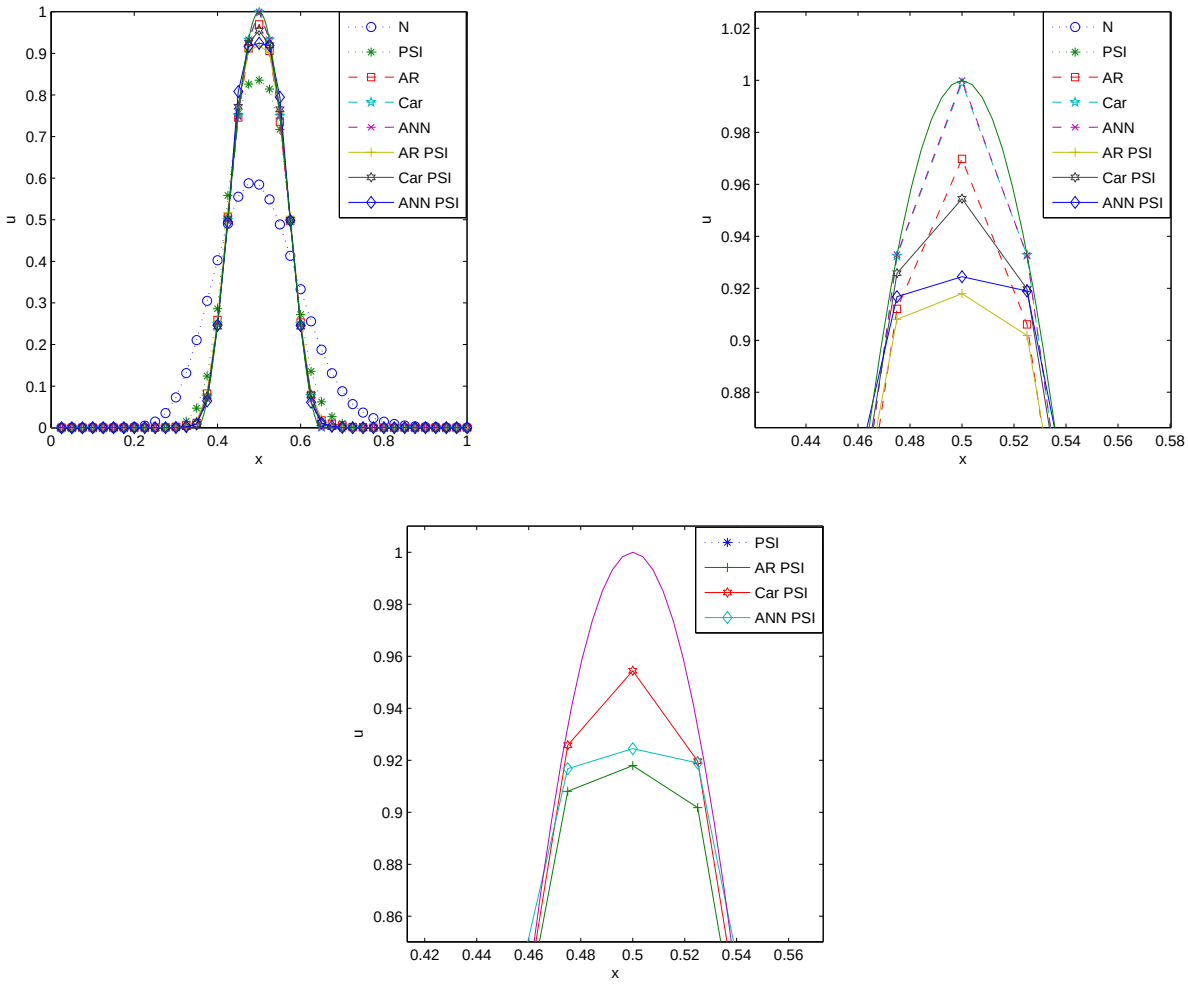

Figure 3.20: Test case B, cosine squared profile at outflow (top left), zoom around the maximum (top right) and zoom around all the positive high order schemes (bottom). Solid line is exact solution.

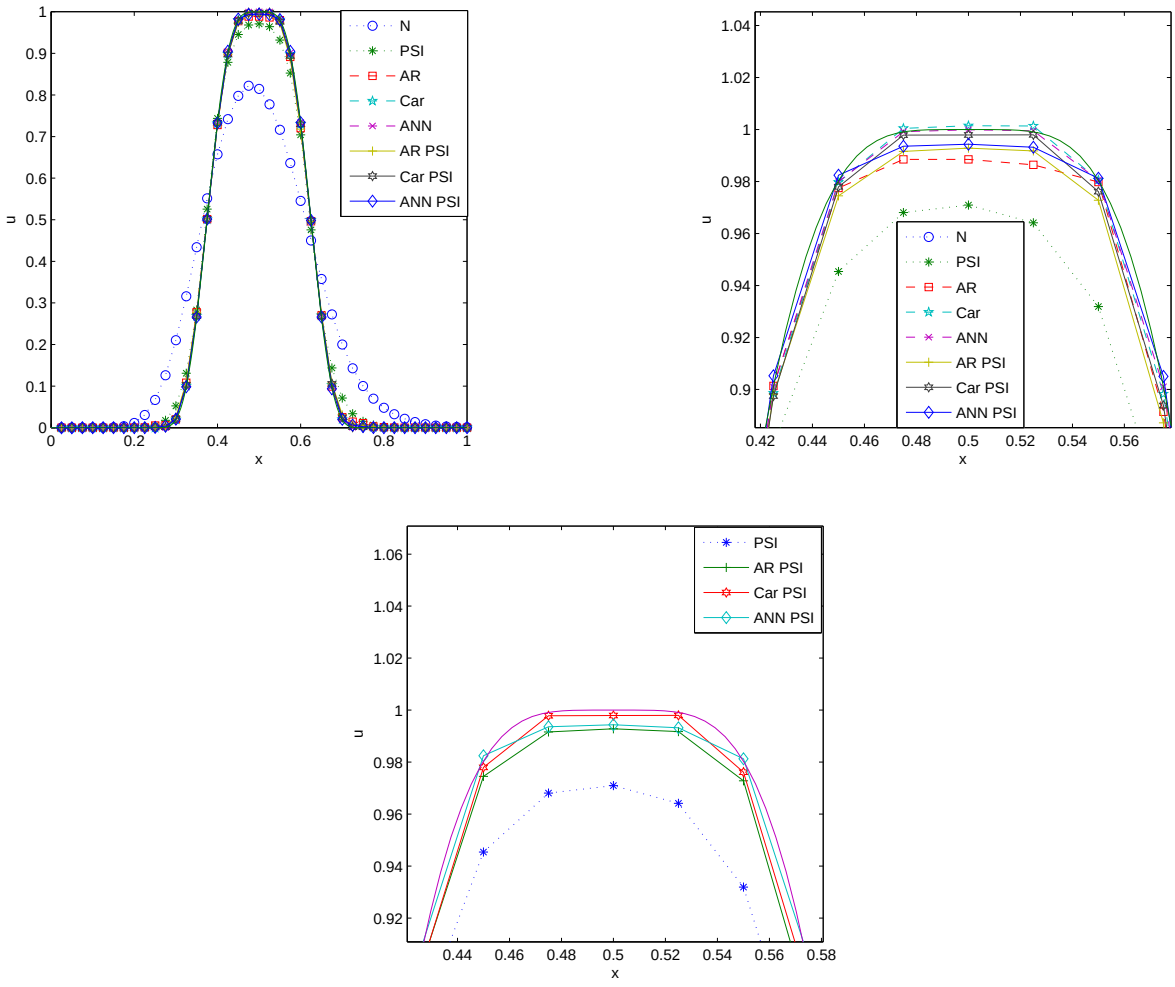

Figure 3.21: Test case C, smooth profile at outflow (top left), zoom around the maximum (top right) and zoom around all the positive high order schemes (bottom). Solid line is exact solution.

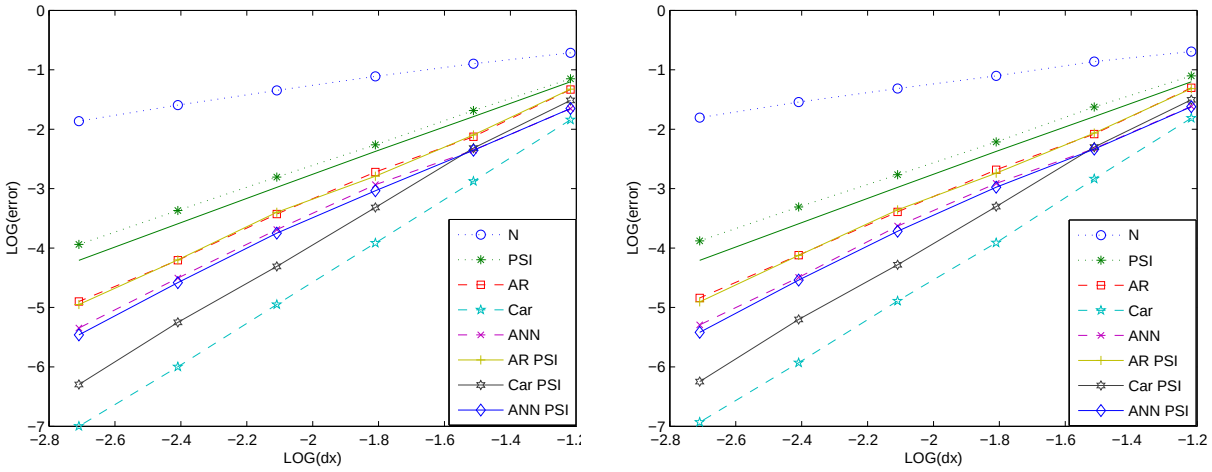

Figure 3.22: Numerical error for grid type A (left), and for grid type B (right) : L_1 error where the solid line without a marker is slope 2.

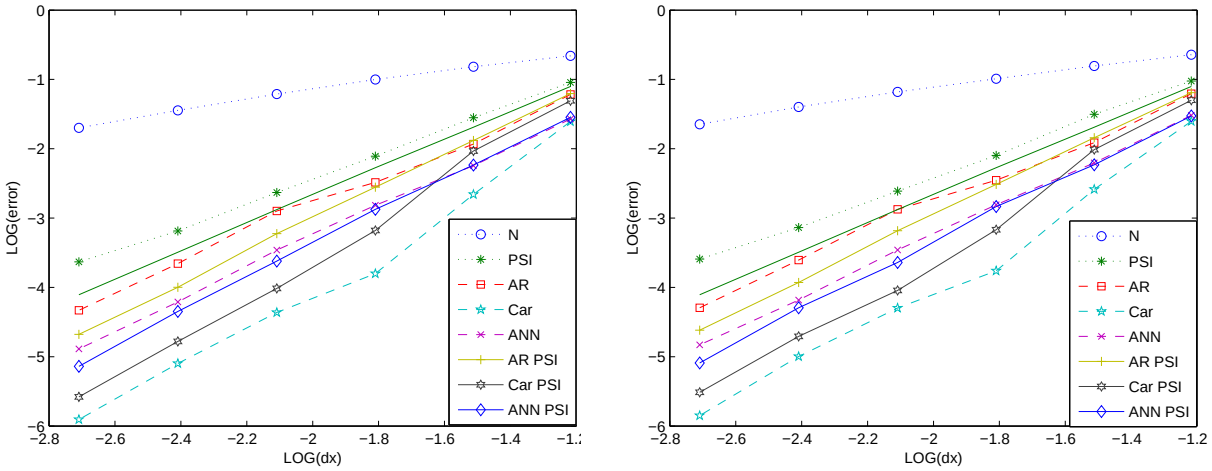

Figure 3.23: Numerical error for grid type A (left), and for grid type B (right) : L_2 error where the solid line without a marker is slope 2.

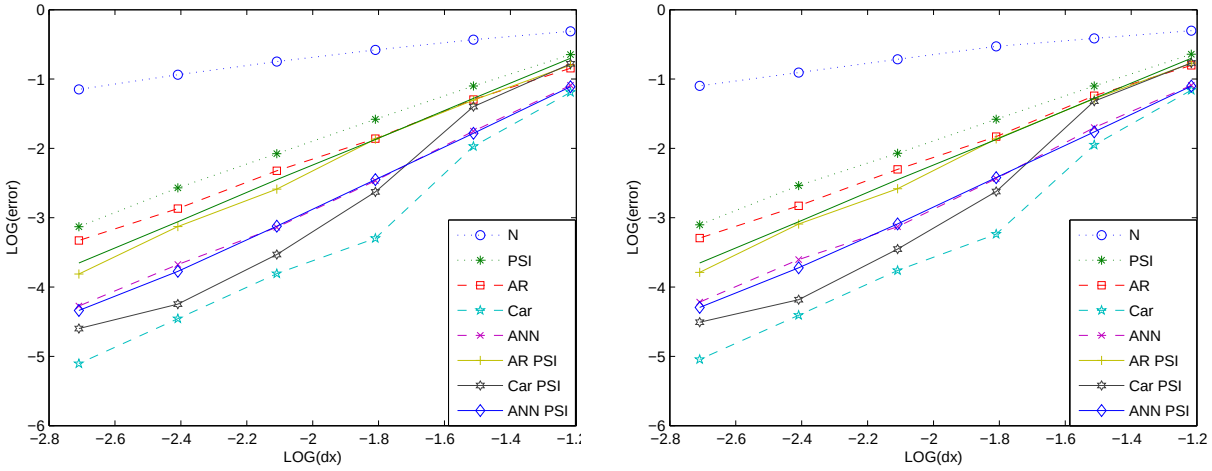

Figure 3.24: Numerical error for grid type A (left), and for grid type B (right) : L_∞ error where the solid line without a marker is slope 2.

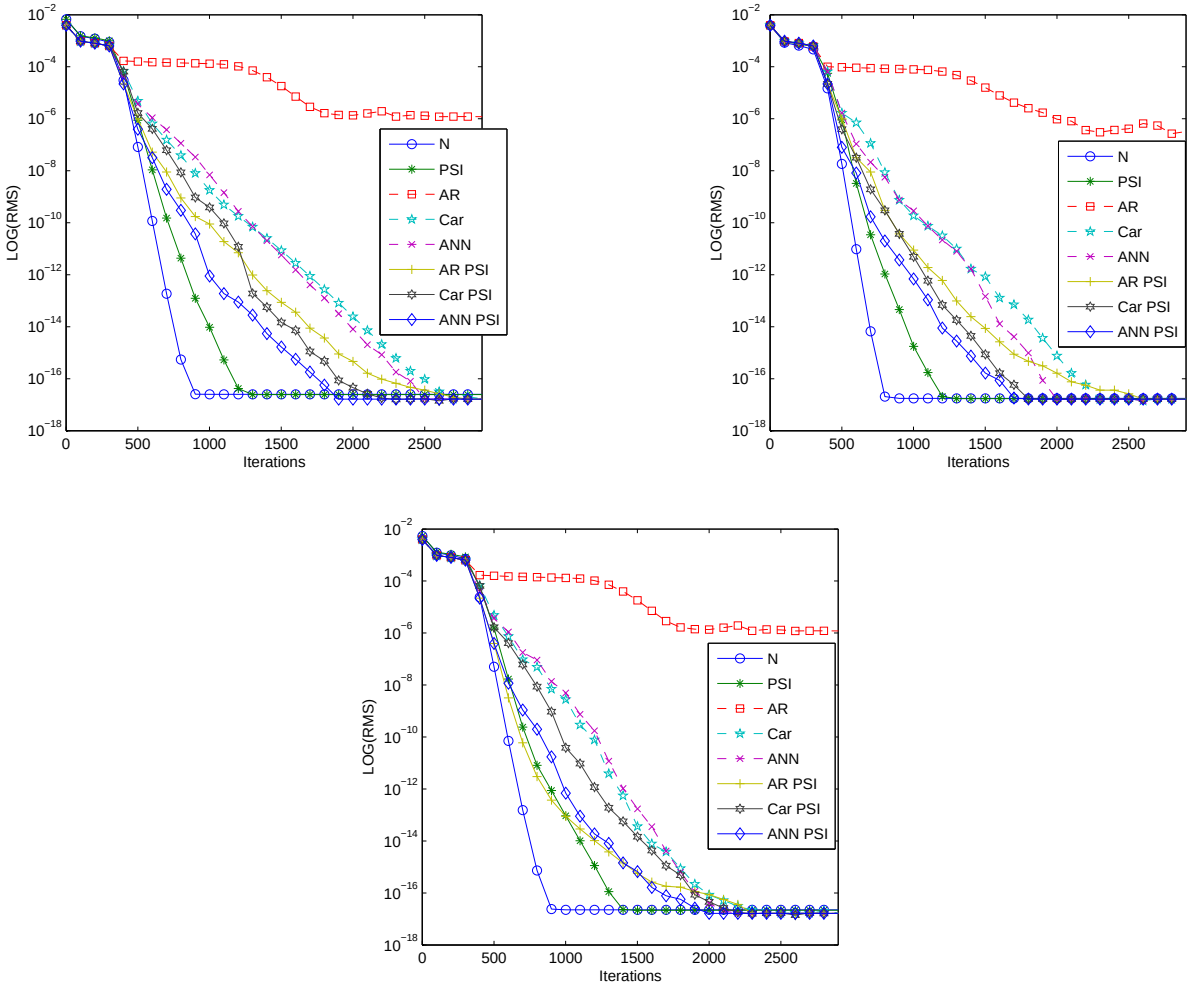

Figure 3.25: Convergence histories for test cases A (top left), B (top right), C (bottom), on meshes shown in Figures 2.19 and 3.12.

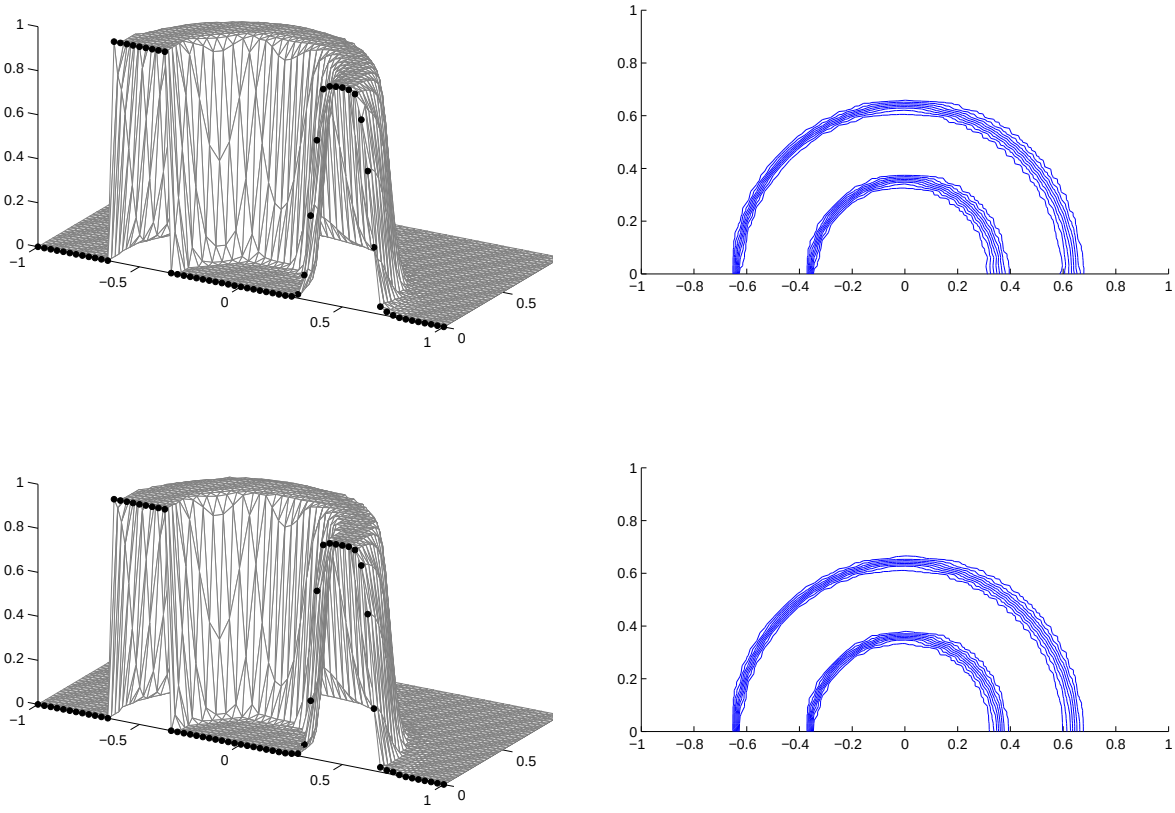

Figure 3.26: Solution for third order ANN PSI scheme (top) and fourth order ANN PSI scheme (bottom) applied to the circular advection square wave test case A.

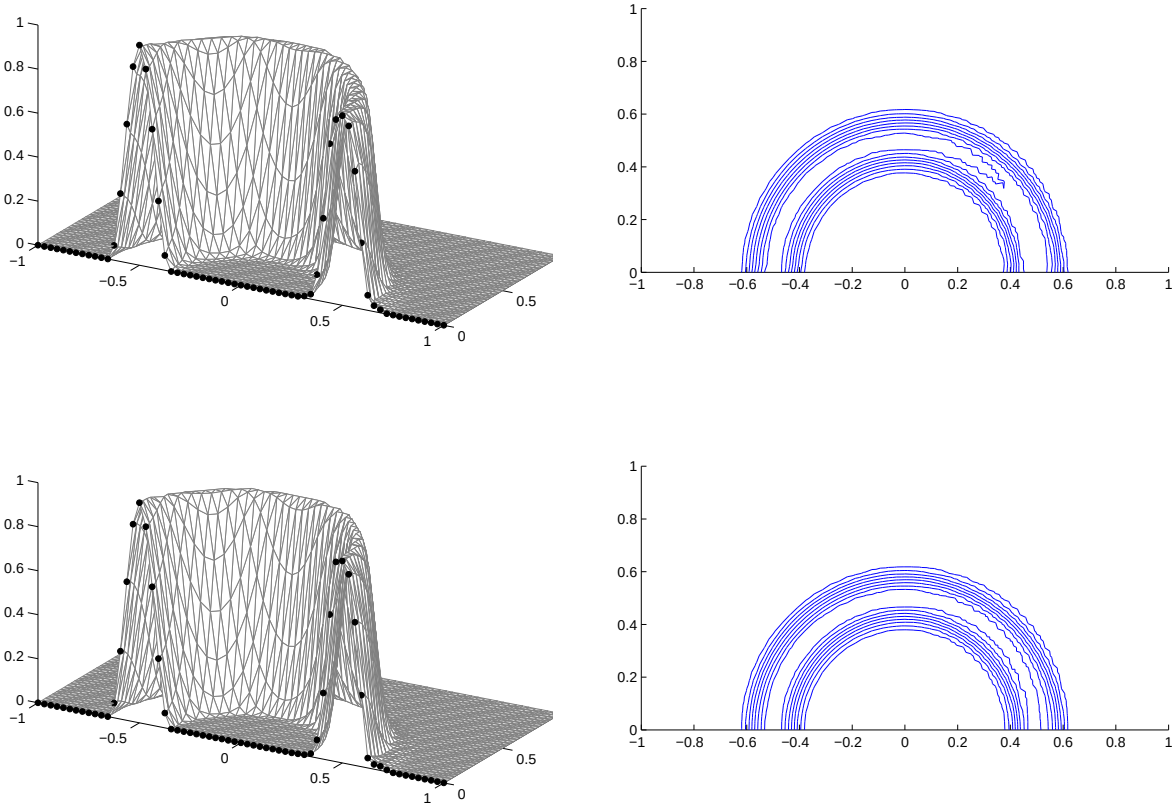

Figure 3.27: Solution for third order ANN PSI scheme (top) and fourth order ANN PSI scheme (bottom) applied to cosine squared profile, test case B.

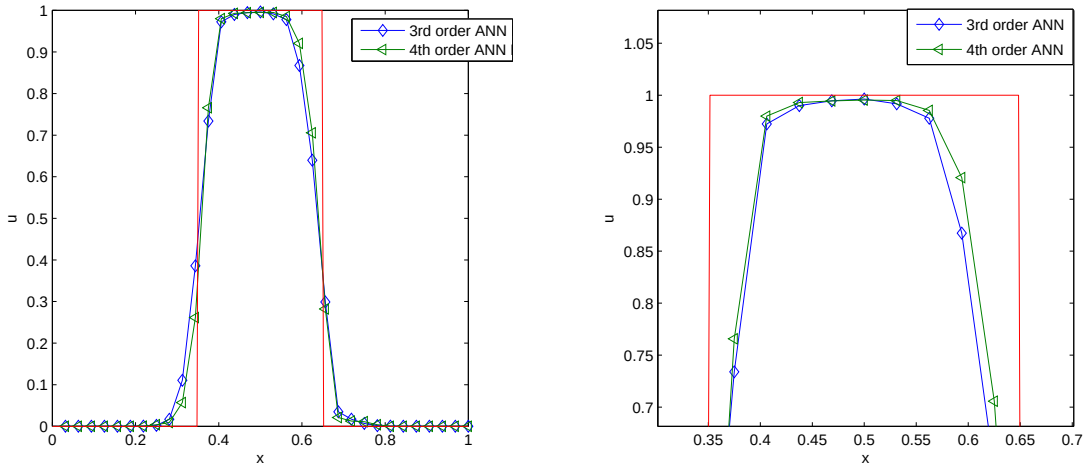

Figure 3.28: Test case A, square wave at outflow (left), zoom around the maximum (right), for third order and fourth order modified ANN PSI schemes. Solid line is exact solution.

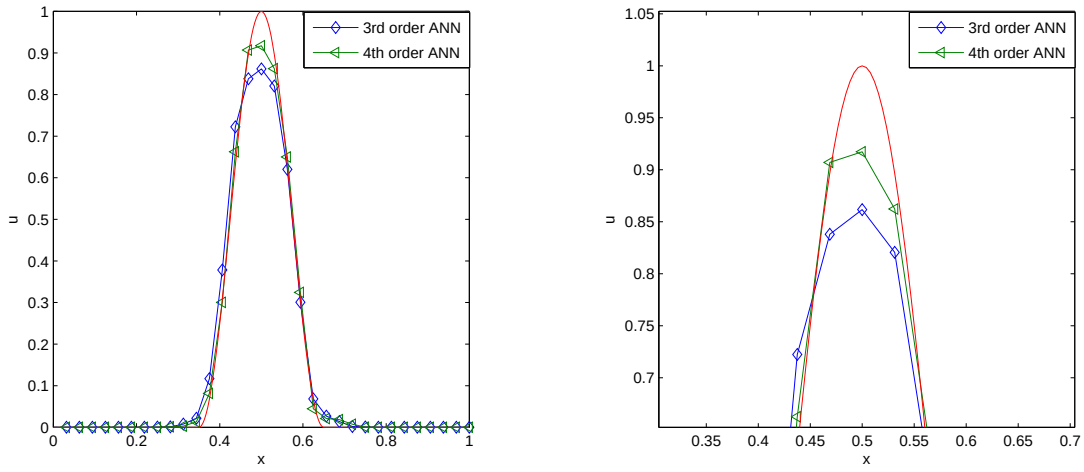

Figure 3.29: Test case B, cosine squared profile at outflow (left), zoom around the maximum (right), for third order and fourth order modified ANN PSI schemes. Solid line is exact solution.

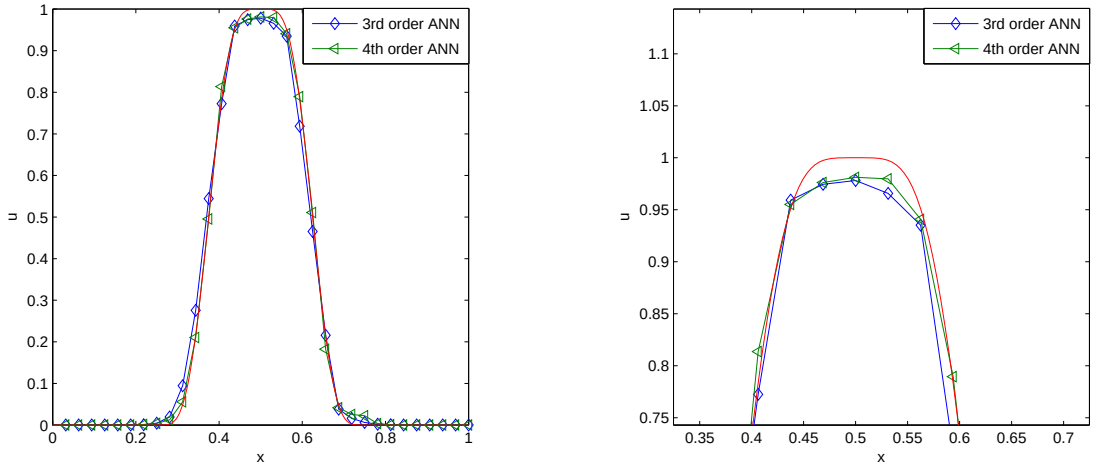

Figure 3.30: Test case C, smooth profile at outflow (left), zoom around the maximum (right), for third order and fourth order modified ANN PSI schemes. Solid line is exact solution.

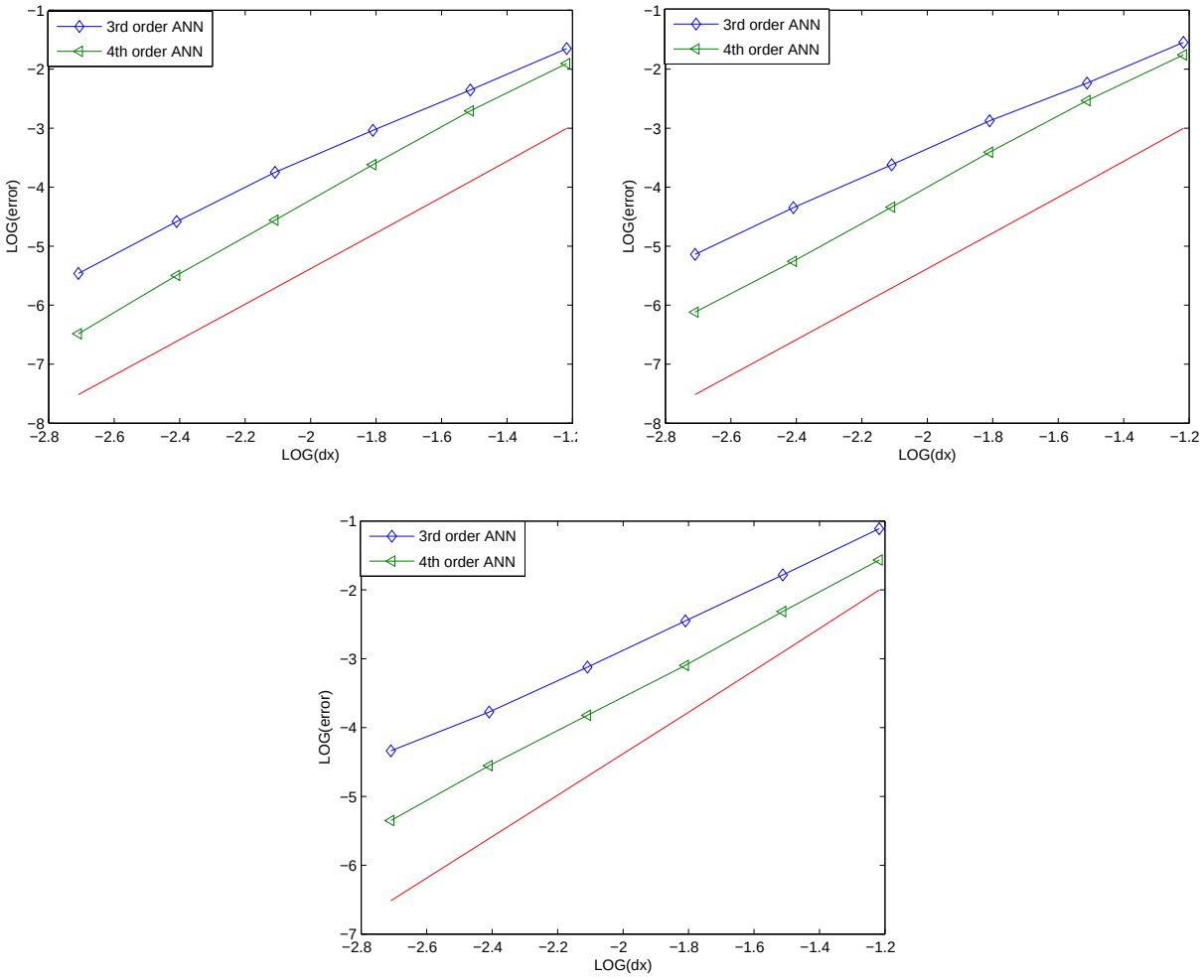

Figure 3.31: Numerical error for third order and fourth order ANN PSI schemes on grid type A : L_1 error (top left), L_2 error (top right) and L_∞ error (bottom) where the solid line without a marker is slope 3.

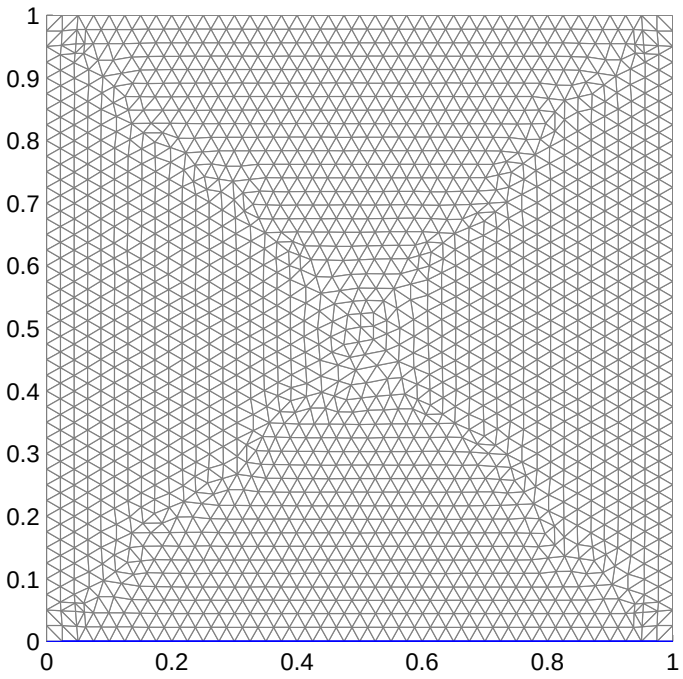

Figure 3.32: A submesh created from a coarser mesh to give a similar number of unknowns as that of genuinely unstructured triangular mesh shown in Figure 2.19, and used for the test case which deals with a discontinuous solution for Burgers' equation.

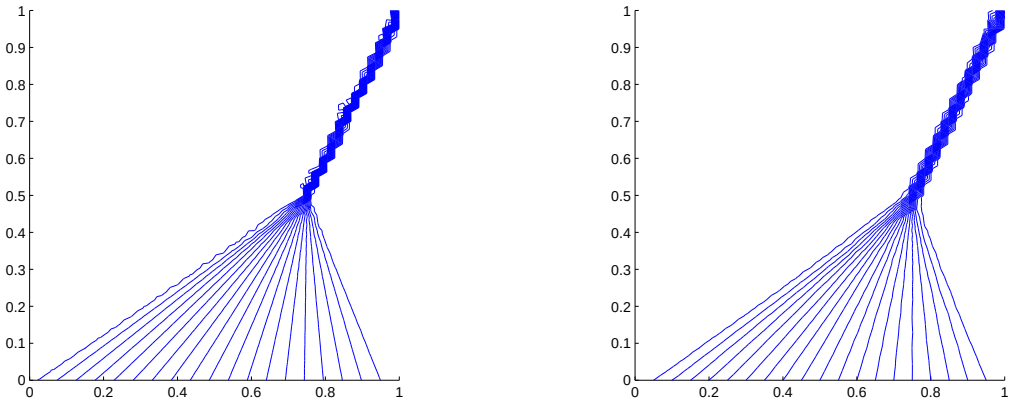

Figure 3.33: Isolines of the AR scheme (left) and AR PSI scheme (right) solutions.

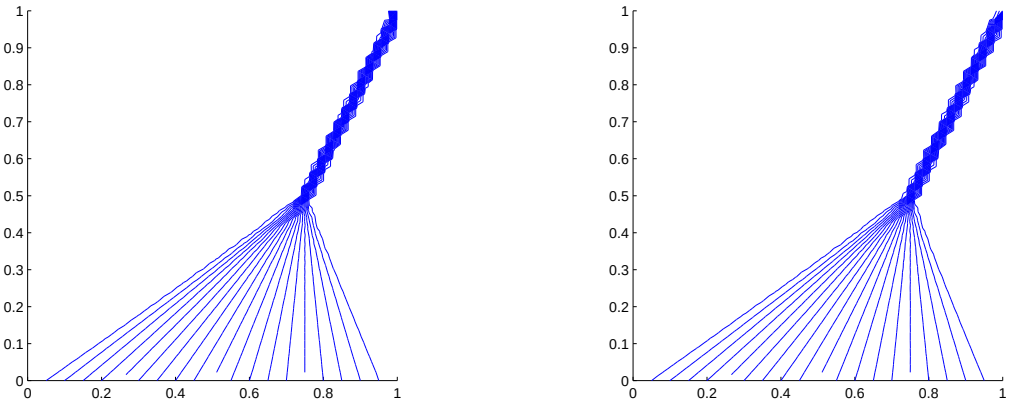

Figure 3.34: Isolines of the ANN PSI scheme (left) and Caraeni PSI scheme (right) solutions.

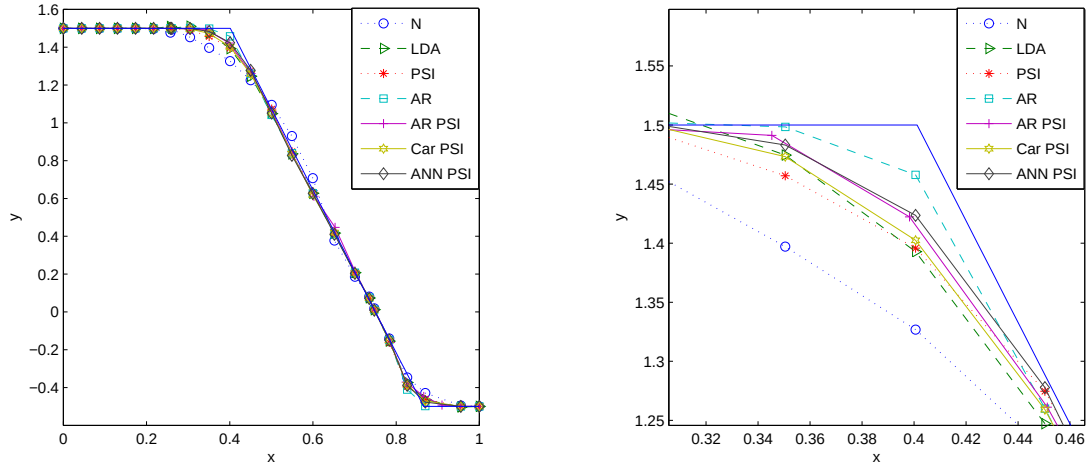

Figure 3.35: Plot of the solutions across the fan, $y = 0.25$, (left) and the zoom around the corner (right). Solid line is exact solution.

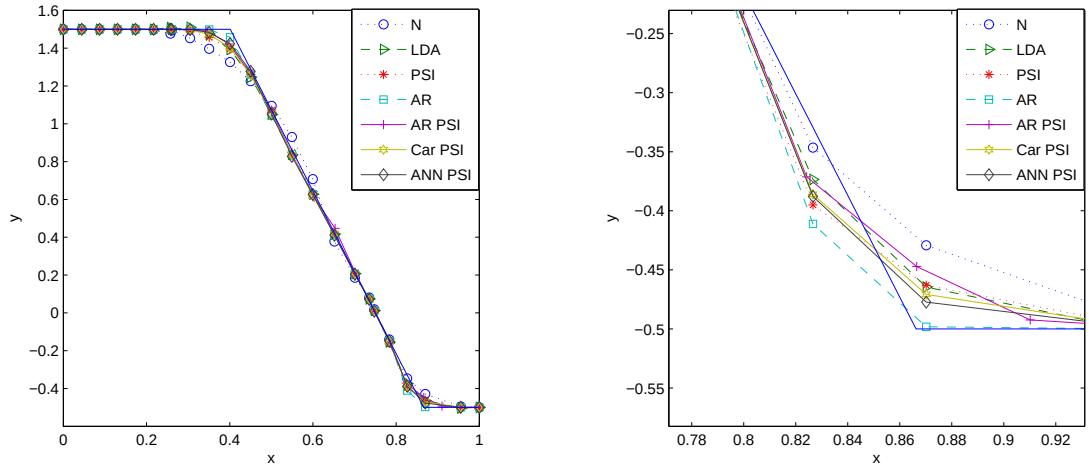

Figure 3.36: Plot of the solutions across the fan, $y = 0.25$, (left) and the zoom around the bottom corner (right). Solid line is exact solution.

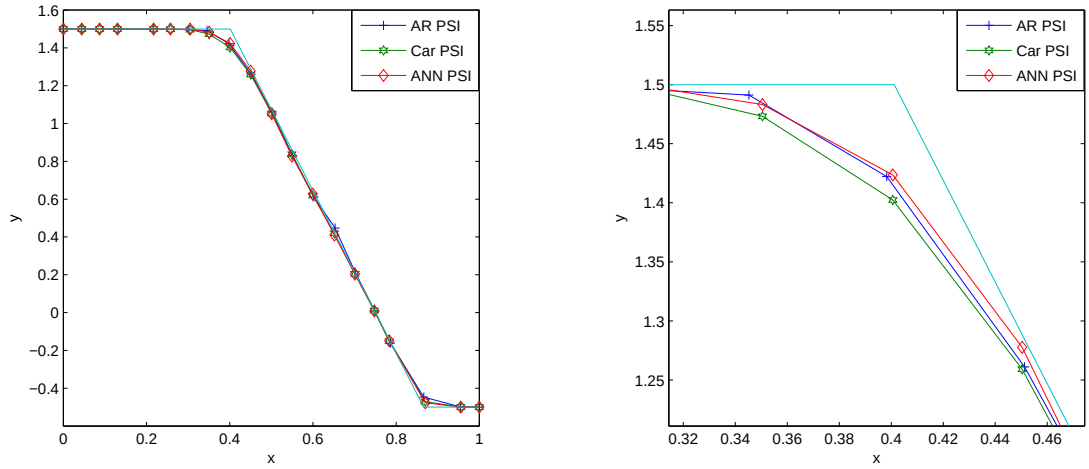

Figure 3.37: Plot of the solutions across the fan, $y = 0.25$, (left) and the zoom around the top corner (right) for the high order positive schemes. Solid line is exact solution.

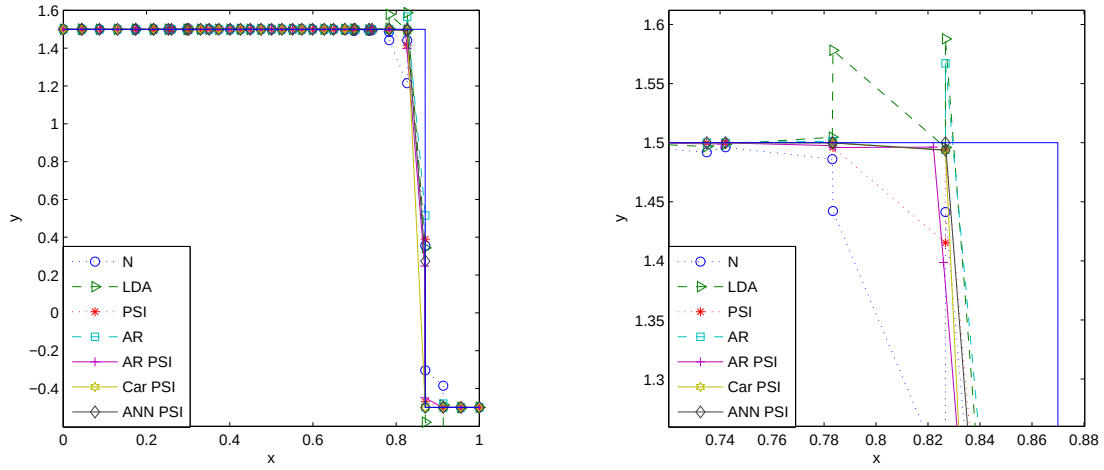

Figure 3.38: Plot of the solutions across the shock,$y = 0.75$, (left) and the zoom around the corner (right). Solid line is exact solution.

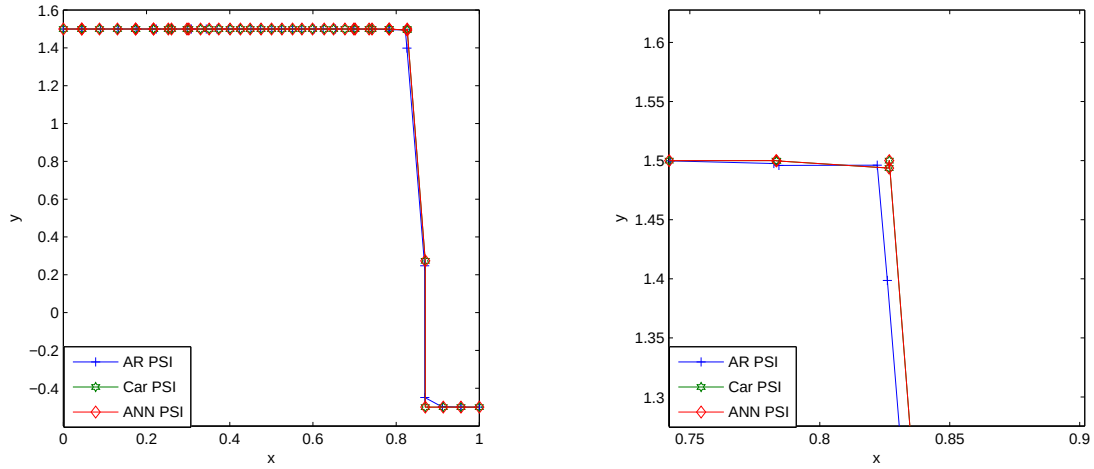

Figure 3.39: Plot of the solutions across the shock, $y = 0.75$, (left) and the zoom around the corner (right) for the high order positive schemes.

Chapter 4

Fluctuation Splitting Schemes for Unsteady Problems

4.1 Introduction

This chapter is concerned with the construction of a multistage high-order (in space *and* time) fluctuation splitting scheme for two-dimensional unsteady scalar advection on triangular meshes. The method has been developed as a complement to the high order discretisation of the steady state by R.Abgrall and P.L.Roe [8], and the unsteady high order space-time discretisation of R.Abgrall, N.Andrianov and M.Mezine [3].

The implementation of this technique was carried out by combining Runge-Kutta time-stepping [79] for the time derivative with a continuous piecewise quadratic representation of the dependent variable, which together lead to a high order space-time fluctuation. The description will start with the space-time variants of the N, followed by PSI and LDA schemes, the construction of higher than second order multistep methods [3], and multistage methods.

4.2 Space-Time Framework

For a fluctuation splitting scheme (2.11), a discrete formulation for unsteady advection can be achieved by introducing a space-time fluctuation splitting framework [6, 24, 26, 30,

68]. The solution of the advection equation (2.5) will be approximated on discretisations of $\Omega_T = \Omega \times [0,t]$, which can be decomposed into space-time prisms $\mathscr{P} = T \times [t^n, t^{n+1}]$, shown in Figure 4.1 for triangular cells. This approach defines the cell fluctuation to be the integral of the differential operator with space-time approximation of u on $T \times [t^n, t^{n+1}]$. For example, to get second order accuracy a second order approximation of u is needed implying $\phi^T = \mathscr{O}(h^3)$. The numerical solution of (2.5) is interpolated linearly in space and linearly in time, i.e.

$$u^h(x,t) = u^{n+1}(x)\frac{t-t^n}{\Delta t} + u^n(x)\frac{t^{n+1}-t}{\Delta t} \ , \tag{4.1}$$

where u^n and u^{n+1} are, respectively, found using the piecewise linear interpolation between $(u^n_{i_1}, u^n_{i_2}, u^n_{i_3})$ and $(u^{n+1}_{i_1}, u^{n+1}_{i_2}, u^{n+1}_{i_3})$. Hence, the discretisations approximating time dependent solutions of (2.5) in $T \times [t^n, t^{n+1}]$ can be summarised in three steps.

1. Compute the fluctuation on the space-time prism $T \times [t^n, t^{n+1}]$

$$\phi^{n+1} = \int_{t^n}^{t^{n+1}} \left(\int_T \frac{\partial u^h}{\partial t} + \vec{\lambda} \cdot \nabla u^h \mathrm{d}\Omega \right) \mathrm{d}t \ , \tag{4.2}$$

   which could be simplified in the piecewise linear case to [6]

$$\phi^{n+1} = \frac{|T|}{3} \sum_{i \in T} (u_i^{n+1} - u_i^n) + \frac{\Delta t}{2} \sum_{i \in T} k_i (u_i^{n+1} + u_i^n) \ . \tag{4.3}$$

2. Distribute the cell fluctuation ϕ^{n+1} to the nodes of T, ϕ_i^{n+1} is used to denote the contribution of the fluctuation to node $i \in T$, and by construction, these must satisfy

$$\sum_{j \in T} \phi_j^{n+1} = \phi^{n+1} \ , \tag{4.4}$$

   for conservation. The distribution coefficients β_i^T, which determine the appropriate proportion of the fluctuation ϕ^{n+1} to be sent from cell T to node i, is given by

$$\beta_i^T = \frac{\phi_i^{n+1}}{\phi^{n+1}} \ , \tag{4.5}$$

   which should also satisfy

$$\sum_{j \in T} \beta_j^T = 1 \ . \tag{4.6}$$

3. Collect all the cell contributions of all $T \in D_i$ and calculate the unknown nodal

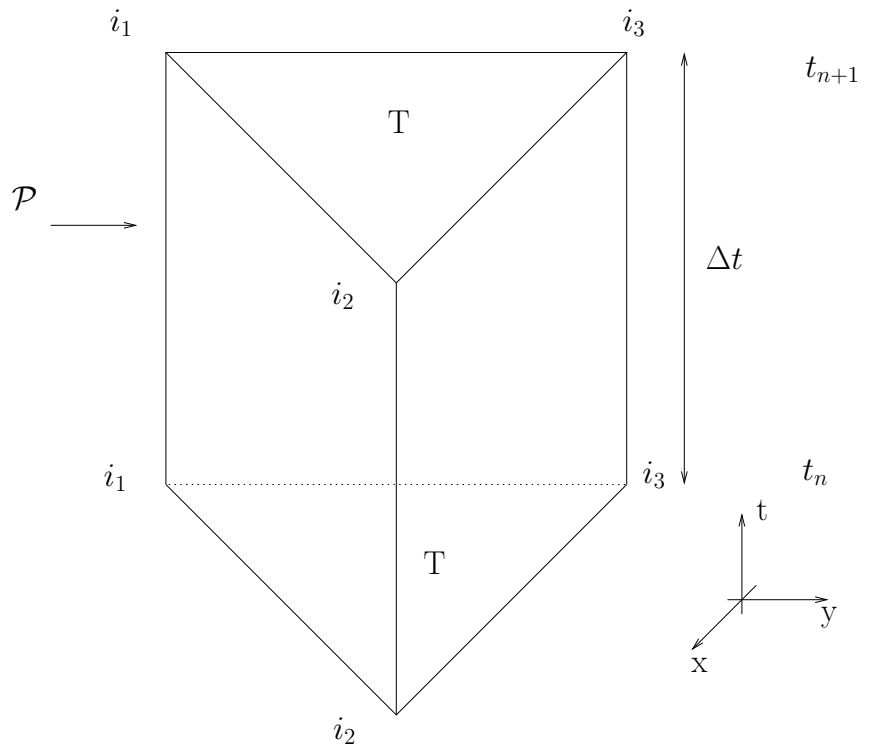

Figure 4.1: Prismatic element $\mathscr{P}$.

values of u^{n+1} by solving the algebraic system

$$\sum_{T \in D_i} \phi_i^{n+1} = 0 \, . \tag{4.7}$$

The basic design properties for the space-time fluctuation splitting schemes remain unchanged except the following two properties.

Positivity

The space-time fluctuation splitting discrete solution at t^{n+1} requires the solution of a system of the type

$$Au^{n+1} = Bu^n \, . \tag{4.8}$$

A positive space-time fluctuation splitting scheme is one for which [68]

1. A is an invertible M-matrix ($A_{ii} \geq 0$, $A_{ij} \leq 0$ for $j \neq i$, $|A_{ii}| > \sum_{j \neq i} |A_{ij}| \; \forall i$)
2. B is a positive matrix ($B_{ij} \geq 0 \; \forall i, \; j$)

A linear positive space-time scheme cannot be linearity preserving according to Godunov's theorem [32, 44, 46]. The positivity property guarantees that there are no numerical oscillations.

The Upwinding Property

For the space-time fluctuation splitting schemes, the fluctuation needs to be distributed upwind in time to the vertices of prism $\mathscr{P}$. This is known as a causality principle and states that no contribution is sent to the past nodes located at time t^n, instead all the fluctuation of $\mathscr{P}$ is sent to time t^{n+1}. Hence, for every space-time prism $T \times [t^n, t^{n+1}]$, a space-time upwind scheme will never distribute any fluctuation to the nodes at time t^n, thereby decoupling the values of u^n at these nodes from their values at time t^{n+1} and producing a true time marching procedure.

4.3 Petrov-Galerkin Formulation

In Chapter 2, the Petrov-Galerkin formulation of the fluctuation splitting approach was outlined. It was shown that the steady state fluctuation splitting schemes can be equated with a mass-lumped Petrov-Galerkin spatial discretisation. Considering the unsteady scalar advection equation, a consistent Petrov-Galerkin formulation where the Petrov-Galerkin is test function applied to the unsteady conservation law is determined by the distribution scheme, of equation (2.43). The semi-discretisation of the unsteady scalar advection equation is [6]

$$\sum_T \sum_j m_{ij}^T \frac{du_j}{dt} + \sum_T \phi_i^T = 0 \,, \tag{4.9}$$

where m_{ij}^T is a consistent mass matrix given by

$$m_{ij}^T = \int_T \omega_i \psi_j \, \mathrm{d}\Omega = \frac{|T|}{3} \begin{bmatrix} \frac{\phi_1^T}{\phi^T} + \frac{1}{6} & \frac{\phi_1^T}{\phi^T} - \frac{1}{12} & \frac{\phi_1^T}{\phi^T} - \frac{1}{12} \\ \frac{\phi_2^T}{\phi^T} - \frac{1}{12} & \frac{\phi_2^T}{\phi^T} + \frac{1}{6} & \frac{\phi_2^T}{\phi^T} - \frac{1}{12} \\ \frac{\phi_3^T}{\phi^T} - \frac{1}{12} & \frac{\phi_3^T}{\phi^T} - \frac{1}{12} & \frac{\phi_3^T}{\phi^T} + \frac{1}{6} \end{bmatrix} . \tag{4.10}$$

Here, ω_i is the Petrov-Galerkin weighting function associated with node i, and ψ_j denotes the standard basis function. The consistent formulation (4.9) is needed to get high order accuracy, and makes the unsteady scheme implicit in time since the consistent mass matrix is not diagonal as it would be for the steady state mass-lumped case. This type of consistent formulation, combined with different time-stepping techniques for the time derivatives and using the standard fluctuation splitting schemes, will be used to carry out unsteady computations.

4.4 Dual time-stepping technique

The dual time-stepping technique [51], is used to solve the nonlinear systems of equations which result from the consistent formulation (4.9) required to reach a high order of accuracy for solving unsteady problems. The consistent formulation consists of coupled nonlinear systems of equation, which need to be solved at each time step by some iterative method. One approach for doing this is the dual time-stepping technique, where the nonlinear system of equations is solved by inner iterations which advance in pseudo-time τ. Hence equation (4.2) is augmented to give

$$\frac{du}{d\tau} + \int_{t^n}^{t^{n+1}} \left(\int_T \frac{du_j}{dt} - \vec{\lambda} \cdot \nabla u^h \mathrm{d}\Omega \right) \mathrm{d}t \ . \tag{4.11}$$

For equation (4.3), this basically means

$$\frac{(u^{m+1} - u_i^m)}{\Delta\tau} = -\frac{|T|}{3} \sum_{i \in T} (u_i^m - u_i^n) - \frac{\Delta t}{2} \sum_{i \in T} k_i (u_i^m + u_i^n) \ . \tag{4.12}$$

where m denotes the pseudo-time level (iteration number). At this point it should be noted that the idea of using subiteration is to converge the solution at each physical time-step. One of the advantages of using the dual time-stepping technique is the fact that, as long as the inner iteration converges, it is simple to use for solving the full system of equations. On the other hand, one must be careful when using the dual time-stepping technique, because there is no way of assessing accuracy unless the inner iterations are fully converged. Also, if a large number of iterations are required, the scheme becomes very expensive and could be very slow to converge.

4.5 The N scheme

The extension of the N scheme to the space-time framework in a consistent manner is essential for the construction of nonlinear limited schemes. One way of constructing this extension is to take the steady N scheme defined by the local nodal fluctuation [10]

$$\phi_i^N = k_i^+ (u_i - \widetilde{u}) \ , \tag{4.13}$$

where

$$\widetilde{u} = \left(\sum_{j \in T} k_j^- \right)^{-1} \left(\sum_{j \in T} k_j^- u_j \right) \ . \tag{4.14}$$

The multidimensional upwind parameters are

$$k_i^+ = \max(0, k_i) \qquad k_i^- = \min(0, k_i) \qquad \text{for } k_i = \frac{1}{2}\vec{\lambda} \cdot \vec{n}_i \ . \tag{4.15}$$

Note that $\sum_{j\in T} k_j = 0$, because $\sum_{j\in T} \vec{n}_j = 0$, and that $k_i = k_i^+ + k_i^-$. The N scheme nodal fluctuation (4.13) combined with the forward Euler time integration leads to an iterative update of the nodal solution values defined by

$$u_i^{n+1} = u_i^n - \frac{\Delta t}{S_i} \sum_T \phi_i^N \ . \tag{4.16}$$

Hence, by combining the above spatial discretisation of the N scheme with Crank-Nicolson time integration, the N scheme can be defined by the space-time local nodal fluctuation

$$\phi_{i_1}^N = \frac{|T|}{3}(u_{i_1}^{n+1} - u_{i_1}^n) + \frac{\Delta t}{2} k_{i_1}^+ (u_{i_1}^{n+1} - \widetilde{u}^{n+1}) + \frac{\Delta t}{2} k_{i_1}^+ (u_{i_1}^n - \widetilde{u}^n) \ , \tag{4.17}$$

which is positive as presented in [6]. Here, $\widetilde{u}^n$ and $\widetilde{u}^{n+1}$ are designed to satisfy the conservation relation (4.4), and $\widetilde{u}^{n+1}$ are defined by (4.14)

Equation (4.17) can also be written as

$$\phi_{i_1}^N = \frac{|T|}{3}(u_{i_1}^{n+1} - u_{i_1}^n) + \frac{\Delta t}{2} \sum_{j\in T} \left[k_{i_1}^+ N k_j^- (u_{i_1}^{n+1} - u_j^{n+1}) + k_{i_1}^+ N k_j^- (u_{i_1}^n - u_j^n) \right] \ , \tag{4.18}$$

where $N = \left(\sum_{j\in T} k_j^- \right)^{-1}$. Given that $M_{i_{1,\ldots,n}}$ are the mesh points, the final scheme as given by (4.7) reads as

$$\sum_{M_{i_1}\in T} \left[\frac{|T|}{3}(u_{i_1}^{n+1} - u_{i_1}^n) + \frac{\Delta t}{2} \sum_{j\in T} \left[k_{i_1}^+ N k_j^- (u_{i_1}^{n+1} - u_j^{n+1}) + k_{i_1}^+ N k_j^- (u_{i_1}^n - u_j^n) \right] \right] = 0 \ , \tag{4.19}$$

and leads to the system $Au^{n+1} = Bu^n$, where A and B are constant matrices given by

$$A_{i_1 i_1} = \sum_{M_{i_1}\in T} \left(\frac{|T|}{3} + \frac{\Delta t}{2} k_{i_1}^+ \right), \qquad A_{i_1 i_2} = \sum_{(M_{i_1}, M_{i_2})\in T} -\frac{\Delta t}{2} k_{i_1}^+ N k_{i_2}^- \ , \tag{4.20}$$

$$B_{i_1 i_1} = \sum_{M_{i_1}\in T} \left(\frac{|T|}{3} - \frac{\Delta t}{2} k_{i_1}^+ \right), \qquad B_{i_1 i_2} = \sum_{(M_{i_1}, M_{i_2})\in T} -\frac{\Delta t}{2} k_{i_1}^+ N k_{i_2}^- \ . \tag{4.21}$$

The proof that A is a matrix independent of Δt, and B is positive under the condition

$\Delta t \max_T \frac{\sum_{j\in T} k_j^+}{|T|} \leq 1$ is outlined in [6].

So far it has been possible to see how the N scheme formulation is obtained, by combining the spatial discretisation of the N scheme with Crank-Nicolson time integration. The dual time-stepping technique (see Section 4.4) is used to solve the linear system of equations using inner iterations which advance in pseudo-time τ.

4.6 The LDA scheme

Early attempts at using fluctuation splitting schemes for time dependent problems resorted to the analogy with the Petrov-Galerkin finite element method, which introduced a consistent mass matrix (4.9) [67]. For the linearity preserving LDA scheme this type of formulation was done in [56] and later in [6, 7, 58]. The way of extending the LDA scheme to the space-time framework, outlined in [6], gives the LDA fluctuation as

$$\begin{aligned}\phi_{i_1}^{LDA} &= \frac{|T|}{3}(-k_{i_1}^+ N + \frac{1}{6})(u_{i_1}^{n+1} - u_{i_1}^n) + \frac{|T|}{3}(-k_{i_1}^+ N - \frac{1}{12}) \sum_{M_j \neq M_{i_1}} (u_j^{n+1} - u_j^{n+1}) + \\ &\quad \frac{\Delta t}{2} k_{i_1}^+ N \sum_{M_j \in T} k_j (u_j^{n+1} + u_j^n) \, . \end{aligned} \tag{4.22}$$

This extension incorporates the consistent formulation (4.9) within a Crank-Nicolson time stepping for the time derivatives coupled with the standard LDA scheme. Combining the consistent formulation (4.9) with the standard LDA scheme can be expressed as

$$\sum_{M_i \in T} \sum_{M_j \in T} m_{ij}^T \frac{du_j}{dt} + \sum_{M_i \in T} (-k_i^+ N) \phi^{LDA}(u^h) = 0 \, . \tag{4.23}$$

where $u^h = \sum_{j\in T} u_j(t)\psi_j$. If Crank-Nicolson time stepping is considered for the time derivatives, one can write

$$\begin{aligned} &\sum_{M_i \in T} \sum_{M_j \in T} m_{ij}^T (u_j^{n+1} - u_j^n) + \frac{1}{2} \sum_{M_i \in T} (-k_i^+ N)(\phi^{LDA} u^{n+1} + \phi^{LDA} u^n) = 0 \, , \\ &\sum_{M_i \in T} \sum_{M_j \in T} m_{ij}^T (u_j^{n+1} - u_j^n) + \frac{1}{2} \sum_{M_i \in T} (-k_i^+ N) \left(\sum_{j \in T} k_j (u_j^{n+1} + u_j^n) \right) = 0 \, , \end{aligned} \tag{4.24}$$

and again leads to a system of the form $Au^{n+1} = Bu^n$. The dual time-stepping technique is used to solve the consistent formulation.

4.7 The PSI scheme

The space-time variant of the PSI scheme is constructed using the blended approach with a combination of the first order positive N scheme (4.19) and the second order linearity preserving LDA scheme (4.22). The fluctuations distributed to the nodes are defined by [30]

$$\phi_{i_1}^{PSI} = l\phi_{i_1}^{N} + (1-l)\phi_{i_1}^{LDA} \tag{4.25}$$

where $l = \max(\varphi(r_{i_1}), \varphi(r_{i_2}), \varphi(r_{i_3}))$ with

$$r_{i_1} = \frac{\phi_{i_1}^{LDA}}{\phi_{i_1}^{N}}, \qquad \varphi(x) = \begin{cases} \frac{x}{1-x} & \text{if } x < 0 \\ 0 & \text{otherwise .} \end{cases} \tag{4.26}$$

The same is done for nodes i_2 and i_3. The general scheme can be written as

$$\sum_{i \in T} (l\phi_i^N + (1-l)\phi_i^{LDA}) = 0 \, . \tag{4.27}$$

The blending parameter which was proposed by [30, 80] for steady state calculation and defined by

$$l = \frac{|\phi^T|}{\sum_{j \in T} |\phi_j^N|} \, , \tag{4.28}$$

does not satisfy the positivity requirements, but still works well [30]. Overall, the formulation of the space-time PSI scheme allows the construction of a second order scheme.

4.8 Multistep Fluctuation Splitting Schemes

This section is concerned with the construction of a high order (in space *and* time) fluctuation splitting scheme for two-dimensional unsteady scalar advection on triangular meshes. The method has been developed to extend the high order discretisation of the steady state by R.Abgrall and P.L.Roe [8], to the unsteady high order space-time discretisation of R.Abgrall, N.Andrianov and M.Mezine [3]. In Section 3.2, T_ξ denoted any of the sub-triangles within T and now the space-time fluctuation is computed over the prism, $\mathscr{P}_\xi = T_\xi \times [t^n, t^{n+1}]$, as shown in Figure 4.2. The fluctuation splitting scheme is defined by

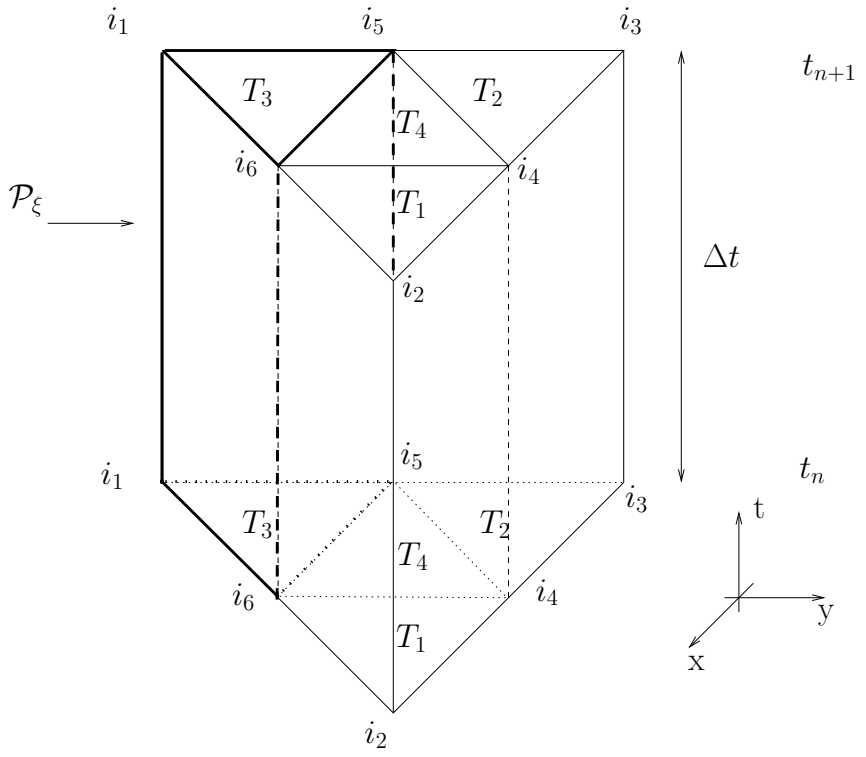

Figure 4.2: Space time mesh for prismatic element $\mathscr{P}_\xi$.

$$\sum_{\mathscr{P}\ni(\sigma,t^{n+1})} \phi^{\mathscr{P}}_{(\sigma,t^{n+1})} = 0 \,. \tag{4.29}$$

The construction of the high order accurate sub-fluctuations $\phi_\sigma^{T_\xi}$, can be summarised as follows.

1. Calculate the first order node contribution, using the N scheme (4.17), or Ricchiutto's version of the N scheme [67].

2. Calculate the high order cell fluctuation $\phi^{\mathscr{P}_\xi}$ with high accuracy, using high order interpolation in space-time over prism $\mathscr{P}_\xi$. Equation (4.2) can be adopted for computing the fluctuation over $\mathscr{P}_\xi$,

$$\phi^{\mathscr{P}_\xi} = \int_{t^n}^{t^{n+1}} \left(\int_T \frac{\partial u^h}{\partial t} + \vec{\lambda} \cdot \nabla u^h \mathrm{d}\Omega \right) \mathrm{d}t \,, \tag{4.30}$$

   and after a long calculation [3], the high order cell fluctuation $\phi^{\mathscr{P}_\xi}$ is obtained. For example, the third order (in space *and* time) fluctuation, $\mathscr{O}(h^{p+2}, \Delta t^4)$ for $p = 2$, takes the form

$$\phi^{\mathscr{P}_\xi} = \int_{T_\xi} (u^{n+1}(x) - u^n(x))\mathrm{d}\Omega \quad + \quad \frac{5\Delta t}{12}\int_{T_\xi} \vec{\lambda}\cdot\nabla u^{n+1}\mathrm{d}\Omega \qquad (4.31)$$
$$+ \quad \frac{2\Delta t}{3}\int_{T_\xi} \vec{\lambda}\cdot\nabla u^{n}\mathrm{d}\Omega - \frac{\Delta t}{12}\int_{T_\xi} \vec{\lambda}\cdot\nabla u^{n-1}\mathrm{d}\Omega$$

3. Calculate the high order node contributions,

$$\phi_{\sigma_i}^{\mathscr{P}_\xi} = \beta_{\sigma_i}^{\xi}\phi^{\mathscr{P}_\xi} \ , \qquad (4.32)$$

where

$$\beta_{\sigma_i}^{\xi} = \frac{\left((\phi_{\sigma_i}^{\xi})^N / \phi_{\xi}^{\mathscr{P}_\xi}\right)^+ + \varepsilon}{\sum_{\sigma_j\in T^\xi}\left((\phi_{\sigma_j}^{\xi})^N / \phi_{\xi}^{\mathscr{P}_\xi}\right)^+ + 3\varepsilon} \ , \qquad (4.33)$$

where $(\phi_{\sigma_i}^{\xi})^N$ is defined as (4.17) in which ξ expresses a generic sub-triangle and σ denotes one of the vertices of the original cell or the additional vertices introduced by the sub-triangulation. Now that the fluctuations at the vertices of the sub-triangles have been calculated, the overall fluctuation at the vertices are accumulated using

$$\phi_{(\sigma,t^{n+1})}^{\mathscr{P}} = \sum_{T_\xi,\sigma_i\in T_\xi} \phi_{\sigma_i}^{\mathscr{P}_\xi} \ . \qquad (4.34)$$

Again the dual time-stepping technique is chosen to solve the consistent formulation.

4.9 Multistage Fluctuation Splitting Schemes

This method has been developed as a complement to the high order discretisation of the steady state by R.Abgrall and P.L.Roe [8], and the unsteady high order space-time discretisation of R.Abgrall, N.Andrianov and M.Mezine [3]. The implementation of this technique was carried out by combining a positive Runge-Kutta time-stepping [79] for the time derivative with a continuous piecewise high order representation of the dependent variable, which together lead to a high order space-time fluctuation. A low order space-time fluctuation is used to assist in stabilising the solution by combining it with the high order fluctuation within each stage of the Runge-Kutta method to reduce the occurrence of unphysical oscillations. For simplicity, the dual time-stepping technique is chosen to solve the nonlinear system of equations which results from the consistent formulation required to reach a high order of accuracy for solving the unsteady prob-

lems. The performance of this method is illustrated using several standard test problems. Multistage fluctuation splitting schemes require the following stages.

1. Use a positive Runge-Kutta time-stepping for the time derivative, as proposed by C. Shu and S. Osher [79], in order to obtain a high order fluctuation splitting scheme by combining it with a continuous piecewise high order representation of the dependent variable. For example, a positive third-order Runge-Kutta method is given as

$$\begin{aligned} u^{(1)} &= u^{(0)} + \Delta t\, L(u^{(0)}) \\ u^{(2)} &= u^{(0)} + \frac{1}{4}\,\Delta t\, L(u^{(0)}) + \frac{1}{4}\,\Delta t\, L(u^{(1)}) \\ u^{(3)} &= u^{(0)} + \frac{1}{6}\,\Delta t\, L(u^{(0)}) + \frac{1}{6}\,\Delta t\, L(u^{(1)}) + \frac{2}{3}\,\Delta t\, L(u^{(2)})\ , \end{aligned} \tag{4.35}$$

   where L is a discrete operator and $u^{(0)} = u^n$, $u^{(m)} = u^{n+1}$ for $s = 1, 2, \ldots, m$, in which m is 3 for the above equation.

2. Calculate the high order representation in space with the Abgrall-Roe scheme, as outlined in the Section 3.2.

3. Calculate the low order fluctuation at each stage. The calculation of the first order node fluctuation follows the various stages of the positive Runge-Kutta method, hence the name multistage method. For example, for a third order positive Runge-Kutta method, the first N scheme Runge-Kutta nodal fluctuation at this stage is given as

$$(\phi_i^{\xi})^N = \frac{|T|}{3}(u_i^{(1)} - u_i^{(0)}) + \Delta t k_i^+ (u_i^{(0)} - \tilde{u}^{(0)})\ , \tag{4.36}$$

   where

$$\tilde{u}^{(0)} = \frac{\sum_{j\in\xi} k_j^- u_j^n}{\sum_{j\in\xi} k_j^-}\ . \tag{4.37}$$

   The second N scheme Runge-Kutta nodal fluctuation at this stage can be written as

$$(\phi_i^{\xi})^N = \frac{|T|}{3}(u_i^{(2)} - u_i^{(0)}) + \frac{\Delta t}{4}(k_i^+ (u_i^{(0)} - \tilde{u}^{(0)})) + \frac{\Delta t}{4}(k_i^+ (u_i^{(1)} - \tilde{u}^{(1)}))\ , \tag{4.38}$$

   and the third N-scheme Runge-Kutta nodal fluctuation at this stage is

$$(\phi_i^{\xi})^N = \frac{|T|}{3}(u_i^{(3)} - u_i^{(0)}) + \frac{\Delta t}{6}(k_i^+(u_i^{(0)} - \tilde{u}^{(0)})) + \frac{\Delta t}{6}(k_i^+(u_i^{(1)} - \tilde{u}^{(1)})) + \frac{2\Delta t}{3}(k_i^+(u_i^{(2)} - \tilde{u}^{(2)})) \; . \tag{4.39}$$

This low order space-time fluctuation is used to assist in stabilising the solution by combining it with the high order fluctuation within each stage of the Runge-Kutta method, so as to reduce the occurrence of unphysical oscillations.

4. Calculate the high order multistage cell fluctuation. As in the above, for the calculation of the first order node fluctuation, the high order cell fluctuation follows the various stages of the multistage methods. For the implementation of this technique using the third order positive Runge-Kutta method for the time derivative, and applied to the high order fluctuation splitting schemes, the first high order Runge-Kutta cell fluctuation at this stage becomes

$$(\phi^{T_\xi})^{HO} = \int_{T_\xi} (u^{(1)}(x) - u^{(0)}(x))\mathrm{d}\Omega + \Delta t \int_{T_\xi} \vec{\lambda} \cdot \nabla u^{(0)}(x)\mathrm{d}\Omega \; . \tag{4.40}$$

The second high order Runge-Kutta cell fluctuation at this stage is

$$(\phi^{T_\xi})^{HO} = \int_{T_\xi} (u^{(2)}(x) - u^{(0)}(x))\mathrm{d}\Omega + \frac{\Delta t}{4}\int_{T_\xi} \vec{\lambda} \cdot \nabla u^{(0)}(x)\mathrm{d}\Omega + \frac{\Delta t}{4}\int_{T_\xi} \vec{\lambda} \cdot \nabla u^{(1)}(x)\mathrm{d}\Omega \; . \tag{4.41}$$

Finally the third high order Runge-Kutta cell fluctuation at this becomes

$$(\phi^{T_\xi})^{HO} = \int_{T_\xi} (u^{(3)}(x) - u^{0}(x))\mathrm{d}\Omega + \frac{\Delta t}{6}\int_{T_\xi} \vec{\lambda} \cdot \nabla u^{(0)}(x)\mathrm{d}\Omega + \frac{\Delta t}{6}\int_{T_\xi} \vec{\lambda} \cdot \nabla u^{(1)}(x)\mathrm{d}\Omega + \frac{2\Delta t}{3}\int_{T_\xi} \vec{\lambda} \cdot \nabla u^{(2)}(x)\mathrm{d}\Omega \tag{4.42}$$

These high order space-time cell fluctuations will lead to a high order space-time fluctuation splitting scheme.

5. Calculate the high order node contributions at each Runge-Kutta stage

$$(\phi_{\sigma_i}^{T_\xi})^{HO} = \beta_{\sigma_i}^{\xi} \phi^{T_\xi} \tag{4.43}$$

where

$$\beta_{\sigma_i}^{\xi} = \frac{\left((\phi_{\sigma_i}^{\xi})^N/(\phi^{T_\xi})^{HO}\right)^+ + \varepsilon}{\sum_{\sigma_j \in T^\xi}\left((\phi_{\sigma_j}^{\xi})^N/(\phi^{T_\xi})^{HO}\right)^+ + 3\varepsilon} \,. \tag{4.44}$$

6. The overall fluctuations $(\phi_\sigma^T)^{HO}$ are accumulated from the different sub-fluctuations $(\phi_{\sigma_i}^{T_\xi})^{HO}$ at each Runge-Kutta stage using

$$(\phi_{\sigma,t^{n+1}}^T)^{HO} = \sum_{T_\xi, \sigma_i \in T_\xi} (\phi_{\sigma_i}^{T_\xi})^{HO} \,. \tag{4.45}$$

It is now possible to see that the implementation of this technique was undertaken systematically using Runge-Kutta discretisation for the time derivative, applied to the existing high order fluctuation splitting schemes. This is done by interpolating the solution in space, and using a multistage time-stepping method to approximate the time derivative. The calculation of the first order node fluctuations and the high order cell fluctuations follows the various stages of the multistage method. As before, the dual time-stepping technique is chosen to solve the nonlinear system of equations which results from the consistent formulation required to reach a high order of accuracy for solving unsteady problems.

4.10 Numerical Results

The rotating cosine hill

The rotating cosine hill is a popular test case for the unsteady linear advection equation. A cosine shape is transported by a circular advection field, with the initial solution given by

$$u(x,y) = \begin{cases} \cos^2(2\pi r) & \text{if } r \leq 0.25 \\ 0 & \text{otherwise} \end{cases} \tag{4.46}$$

where $r = \sqrt{(x-0.5)^2 + y^2}$, and $\vec{\lambda} = (y,-x)^T$. At each time step, the solution is set to zero at the inflow boundary. The initial profile should be advected in a circle without changing its shape until it returns to its original position when $t = 2\pi$. In the numerical experiments maintaining the ratio $\frac{\Delta t}{\Delta x} = 0.08$ (for all cases) gives a maximum CFL number of approximately 0.713. Uniform structured triangular meshes, shown in Figures 4.3 and 4.4, will be used for rotating cosine hill and rotating cylinder test cases the second of which will be outlined below. The accuracy

measures are also calculated using these structured triangular meshes, by repeatedly halving the background mesh size starting from coarser mesh, so that it is possible to see the rate at which the error will reduce as finer meshes are used. A sequence of four structured grids with 484, 1849, 7225 and 28561 vertices are used.

The visual examination of the accuracy of the scheme is done by plotting the solution, as shown in Figures 4.5 to 4.8, where all the schemes described in this chapter are shown. On the left of the figures the full data is plotted and on the right, contour plots of the solutions are shown. The N scheme, shown in Figures 4.5 and 4.7, is clearly the most diffusive, even though the solution is kept positive. Since the N scheme is not linearity preserving, it is not surprising to see the maximum value of the solution well below one, as outlined in Tables 4.1 and 4.2. The measured order of accuracy reported in Tables 4.3 and 4.4 and Figures 4.13 to 4.15 is roughly what was expected for the N scheme [58] and based on this, it is possible to see that they are first order accurate schemes. The results for the LDA scheme also shown in the same tables and figures. The peak value is much better than that of the N scheme, but it is also clear to see that the solution is not positive, as reported in Tables 4.1 and 4.2 as well. Moreover the schemes are not able to preserve the initial peak value, which is confirmed by the result on the left of the figures, and the measured order of accuracy is within the range of expected values given in [58]. The PSI scheme, also in Figures 4.5 and 4.7, shows the positive property by the complete absence of oscillations in the field. It is also less diffusive compared to the N scheme which can be confirmed by the plot on the right. The accuracy measure also confirms that the PSI scheme gives a better approximation of the solution compared to the N scheme.

The results for second order and third order multistep schemes are shown in Figures 4.6 and 4.8 respectively. Both schemes keep the solution above zero to some extent, but as outlined in Tables 4.1 and 4.2, since the underlying high order scheme is not positive [3] there are small oscillations which can be seen in the numbers in the table. It is worth noting that the result obtained with the third order multistep scheme has a maximum solution value that is a bit closer to the exact value than the value given by the second order multistep scheme.

What is interesting to note is that the second order multistep scheme shows a bit more of a dissipative character than the third order multistep scheme. This is clearly seen in the contour plots of the solution. The second order and third order multistage schemes are reported in Figures 4.6 and 4.8. These schemes are not positive, again

since the underling high order scheme is not positive. This is substantiated by the results as outlined in Tables 4.1 and 4.2. As with the multistep schemes, the more dissipative character of the second order multistage scheme compared to the third order multistage scheme can also be confirmed by the contour plot of the solution. Moreover the third order multistage scheme produces a peak value which is better than the third order multistep schemes described above. It is also possible to see the exact profile is closely preserved with little smearing compared to the rest of the schemes presented above.

A grid convergence study for the unsteady problems is outlined in Table 4.3 and Figures 4.13, 4.14 and 4.15, for L_1, L_2 and L_∞ norms. The third order multistage and third order multistep schemes have roughly the similar slope and the superior accuracy of these schemes are clearly demonstrated. All of the high order schemes produce a slope which is higher than 1.5 in L_1 and L_2 norms, and generally it is also possible to see the accuracy improve as the mesh is refined for L_∞. Overall the comparison between the accuracy measures produced using mesh type A and mesh type B have minimal difference, but mesh type B produces a slightly better accuracy than mesh type A, as the mesh connectivity is favourably inclined for this test case.

The rotating cylinder

The rotating cylinder test case differs from the rotating cosine hill test case only in the initial profile transported by the circular advection field, with the initial solution given by

$$u(x,y) = \begin{cases} 1 & \text{if } r \leq 0.25 \\ 0 & \text{otherwise .} \end{cases} \tag{4.47}$$

This is a discontinuous test case and, as in the previous test case, $r = \sqrt{(x-0.5)^2+y^2}$, and $\vec{\lambda} = (y,-x)^T$. The solutions are shown in Figures 4.9 to 4.12. The solutions obtained using the rotating cylinder test case exhibit similar properties to those of the rotating cosine hill solutions. As expected the LDA scheme, Figures 4.9 and 4.11, shows a spurious oscillation since it doesn't satisfy the positivity property. As usual the N scheme, shown in the same figures, is the most diffusive, even though the solution is kept positive again. The PSI scheme, also shown in the same figures, exhibits the positive property and produces a peak which preserves the exact profile better than the N scheme.

Schemes	rotating cylinder		rotating cosine hill
	min	max	max
N	0.0000	0.8763	0.1993
LDA	-0.0906	1.2250	0.7989
PSI	0.0000	0.9904	0.7782
Second order multistep	-0.0051	0.9999	0.7561
Third order multistep	-0.0003	1.0000	0.7825
Second order multistage	-0.0063	0.9999	0.7511
Third order multistage	-0.0007	1.0000	0.7982

Table 4.1: Minimum and maximum solutions for the rotating cosine hill and rotating cylinder test cases, using mesh type A.

Schemes	rotating cylinder		rotating cosine hill
	min	max	max
N	0.0000	0.8771	0.2003
LDA	-0.0911	1.2263	0.7992
PSI	0.0000	0.9917	0.7797
Second order multistep	-0.0057	0.9999	0.7576
Third order multistep	-0.0008	1.0000	0.7887
Second order multistage	-0.0051	0.9999	0.7537
Third order multistage	-0.0012	1.0000	0.8015

Table 4.2: Minimum and maximum solutions for the rotating cosine hill and rotating cylinder test cases, using mesh type B.

The second order and third order multistep schemes are shown in Figures 4.10 and 4.12. The third order multistep scheme maintains the initial peak better than the second order multistep scheme, even though the schemes are not positive as the underlying high order scheme is not positive. Moreover qualitatively the solutions exhibit similar properties as the corresponding rotating cones. The second order and third order multistage scheme, shown also in Figures 4.10 and 4.12, also doesn't keep the solution above zero and to a small extent it preserves the initial peak value better than the multistep schemes described in this chapter.

Schemes	L_1 order	L_2 order	L_∞ order
N	0.76	0.69	0.57
PSI	1.63	1.47	0.98
LDA	1.87	1.73	1.24
Second order multistep	1.67	1.51	1.21
Third order multistep	1.96	1.88	1.31
Second order multistage	1.71	1.58	1.26
Third order multistage	1.98	1.88	1.34

Table 4.3: Accuracy measures for rotating cosine hill, using mesh type A.

Schemes	L_1 order	L_2 order	L_∞ order
N	0.79	0.71	0.59
PSI	1.66	1.48	1.03
LDA	1.91	1.75	1.27
Second order multistep	1.69	1.55	1.23
Third order multistep	1.98	1.89	1.34
Second order multistage	1.74	1.60	1.28
Third order multistage	1.99	1.91	1.36

Table 4.4: Accuracy measures for rotating cosine hill, using mesh type B.

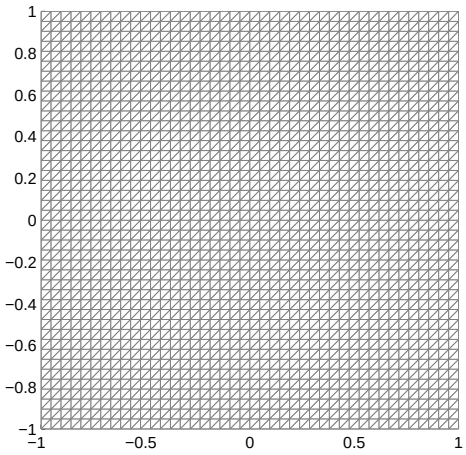

Figure 4.3: The mesh A, used for the rotating advection results.

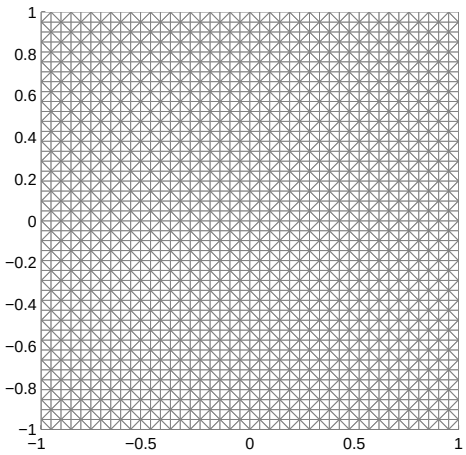

Figure 4.4: The mesh B, used for the rotating advection results.

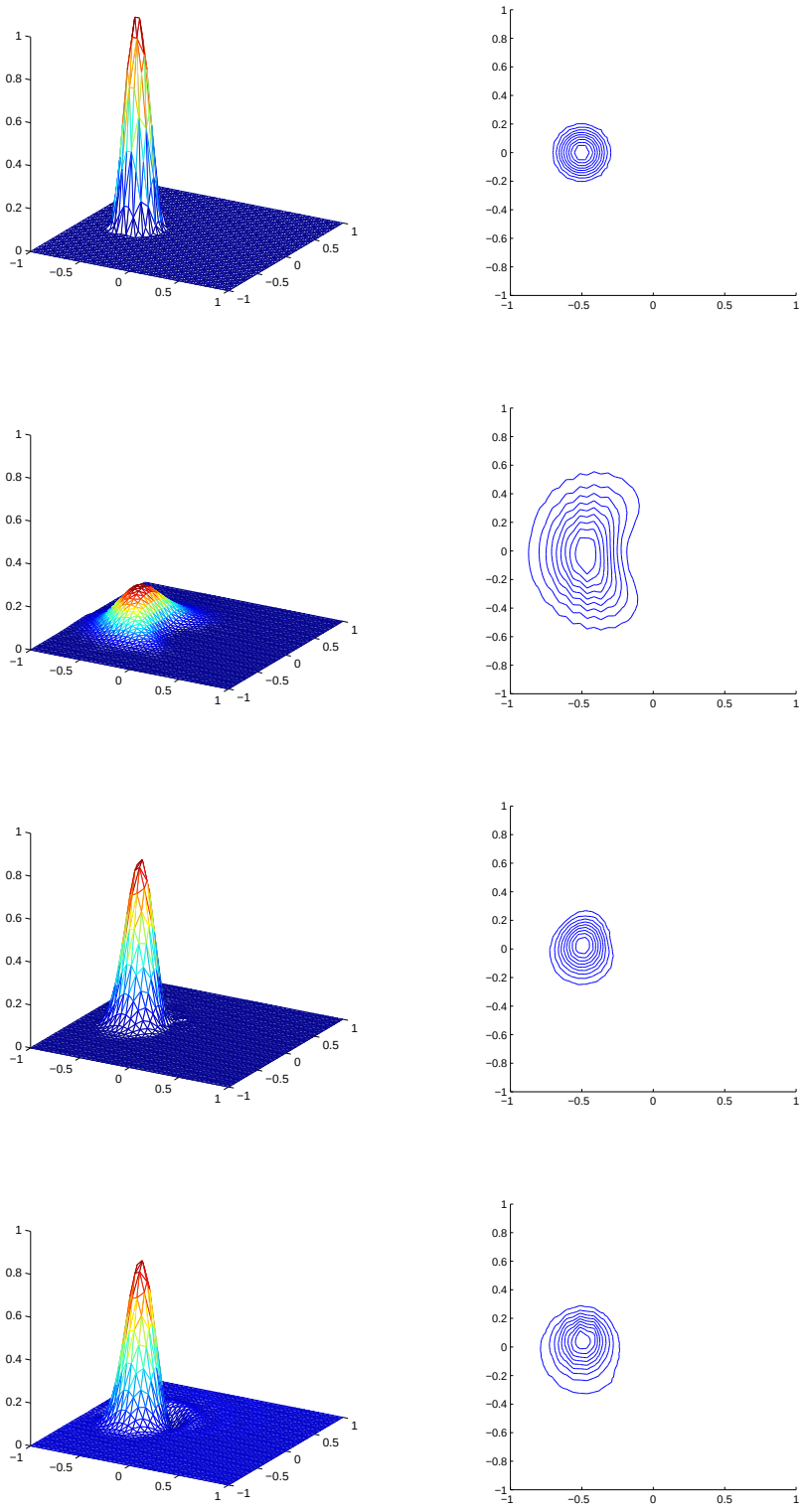

Figure 4.5: Solution for the rotating cosine hill after one revolution on mesh type A, for exact (top), N (second from top), PSI (third from top) and LDA (bottom) schemes.

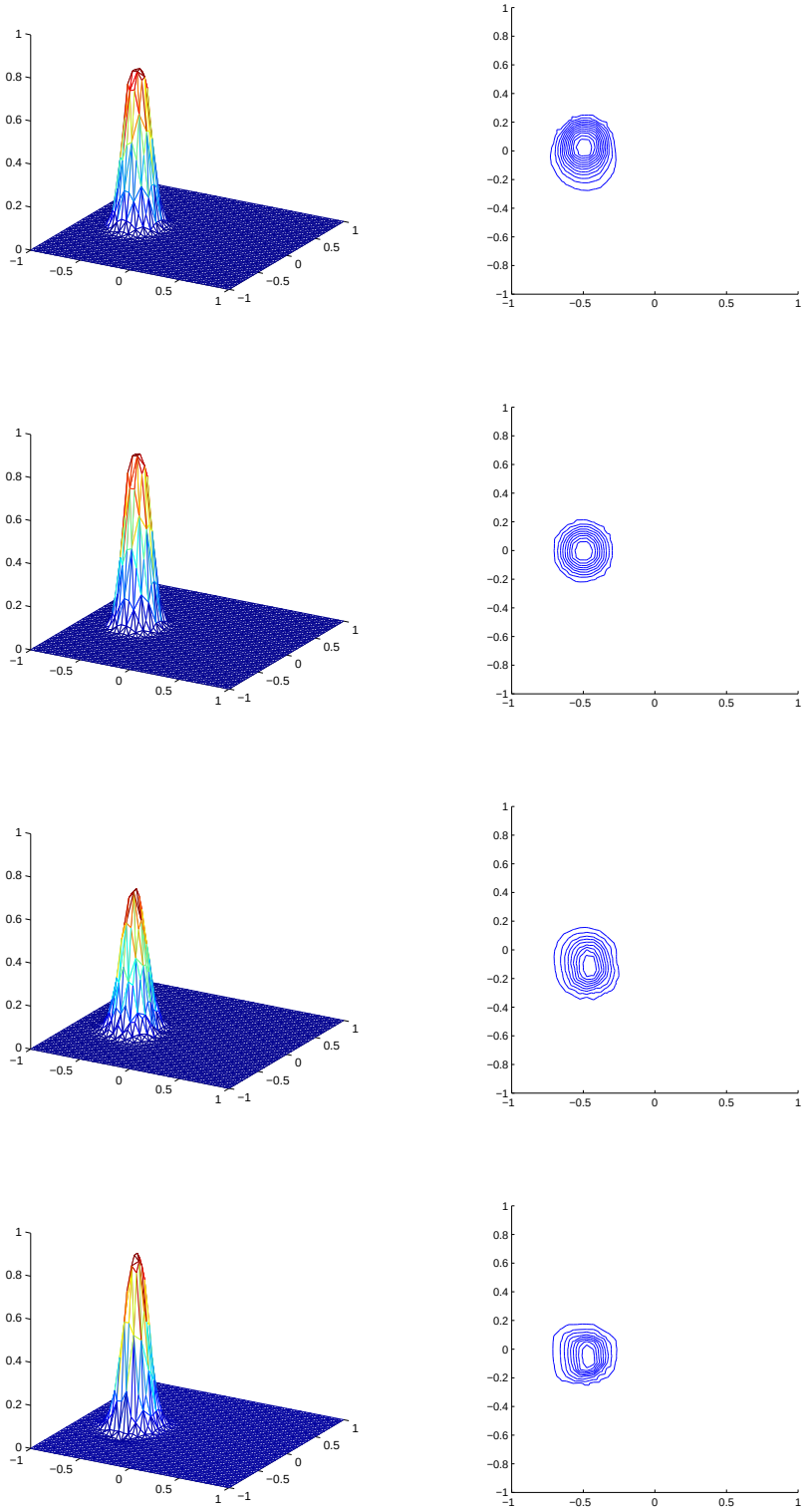

Figure 4.6: Solution for the rotating cosine hill after one revolution on mesh type A, for second order multistep (top), third order multistep (second from top), second order multistage (third from top) and third order multistage (bottom), schemes.

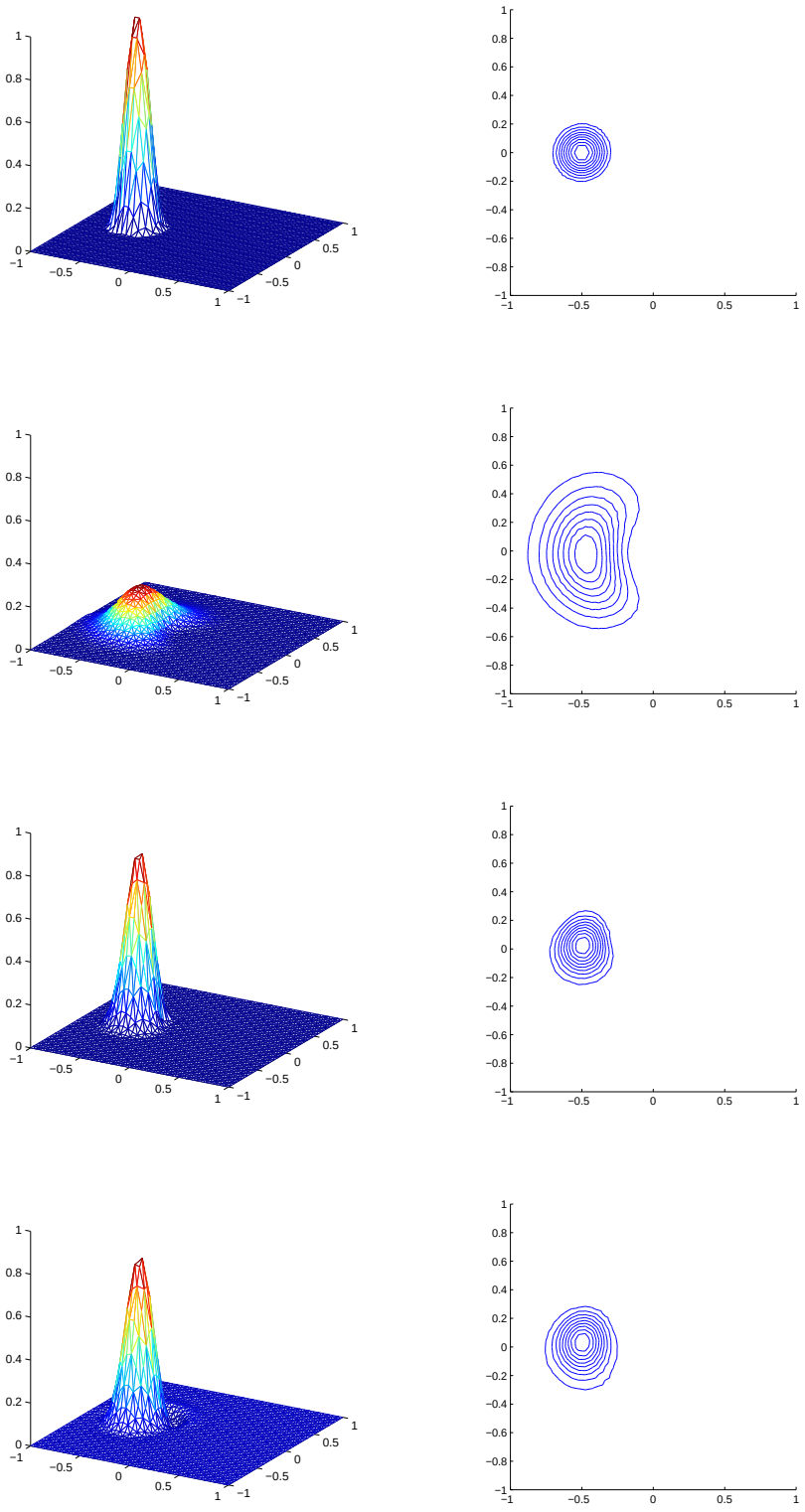

Figure 4.7: Solution for the rotating cosine hill after one revolution on mesh type B, for Exact (top), N (second from top), PSI (third from top) and LDA (bottom) schemes.

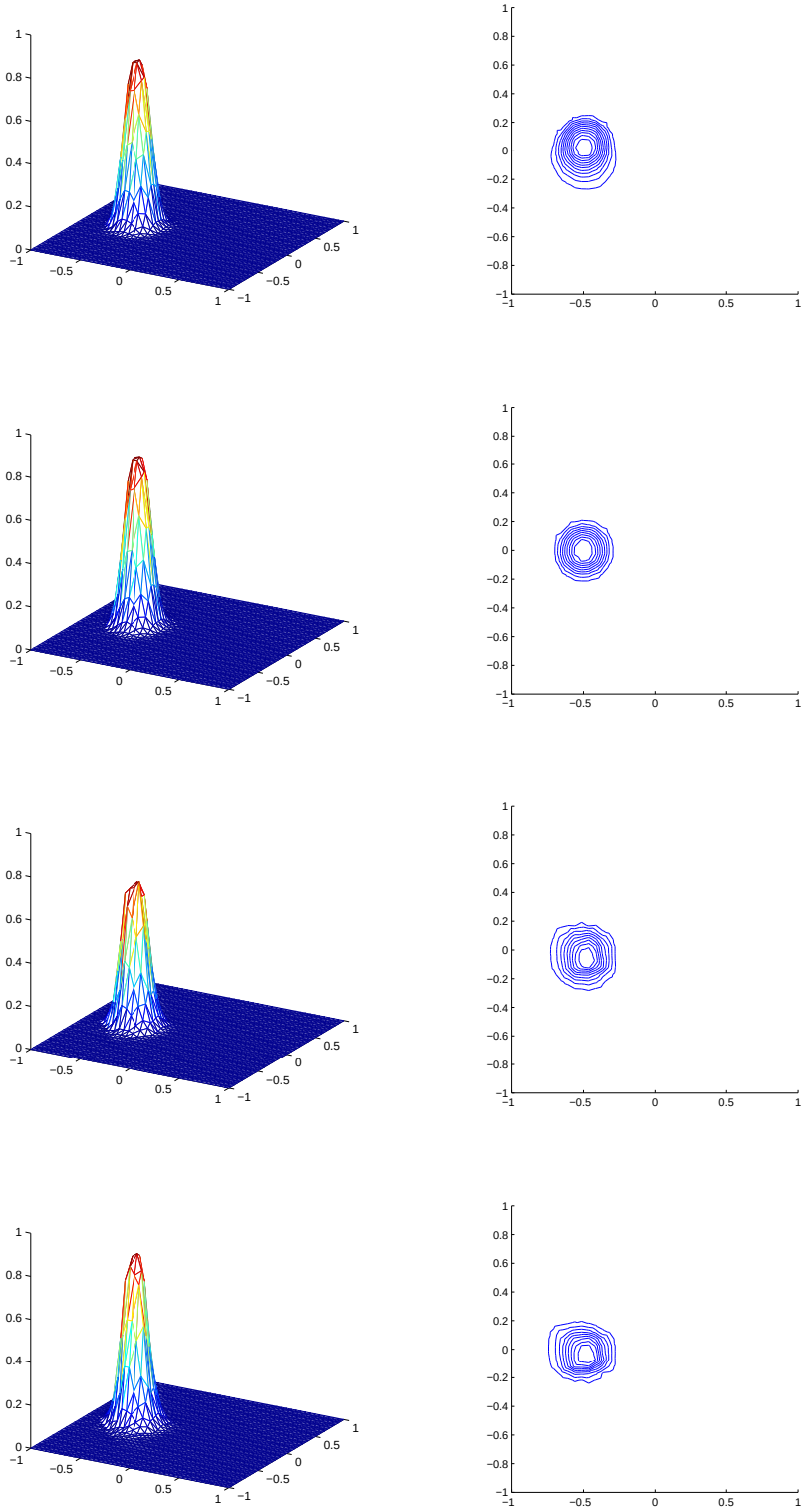

Figure 4.8: Solution for the rotating cosine hill after one revolution on mesh type B, for second order multistep (top), third order multistep (second from top), second order multistage (third from top) and third order multistage (bottom), schemes.

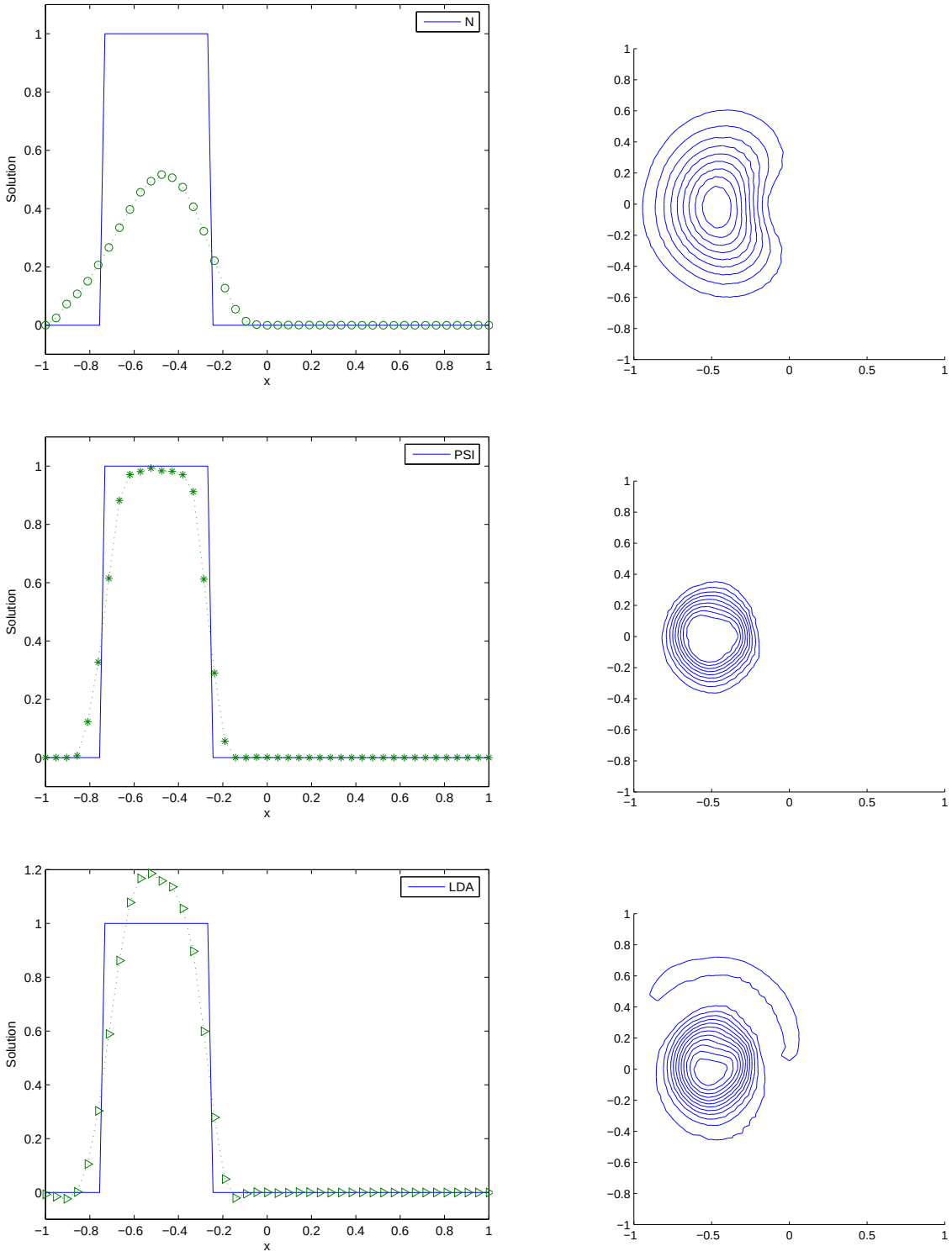

Figure 4.9: Solution for the rotating cylinder after one revolution on mesh type A, for N (top), PSI (middle) and LDA (bottom) schemes, where the solid line without a marker is the exact solution.

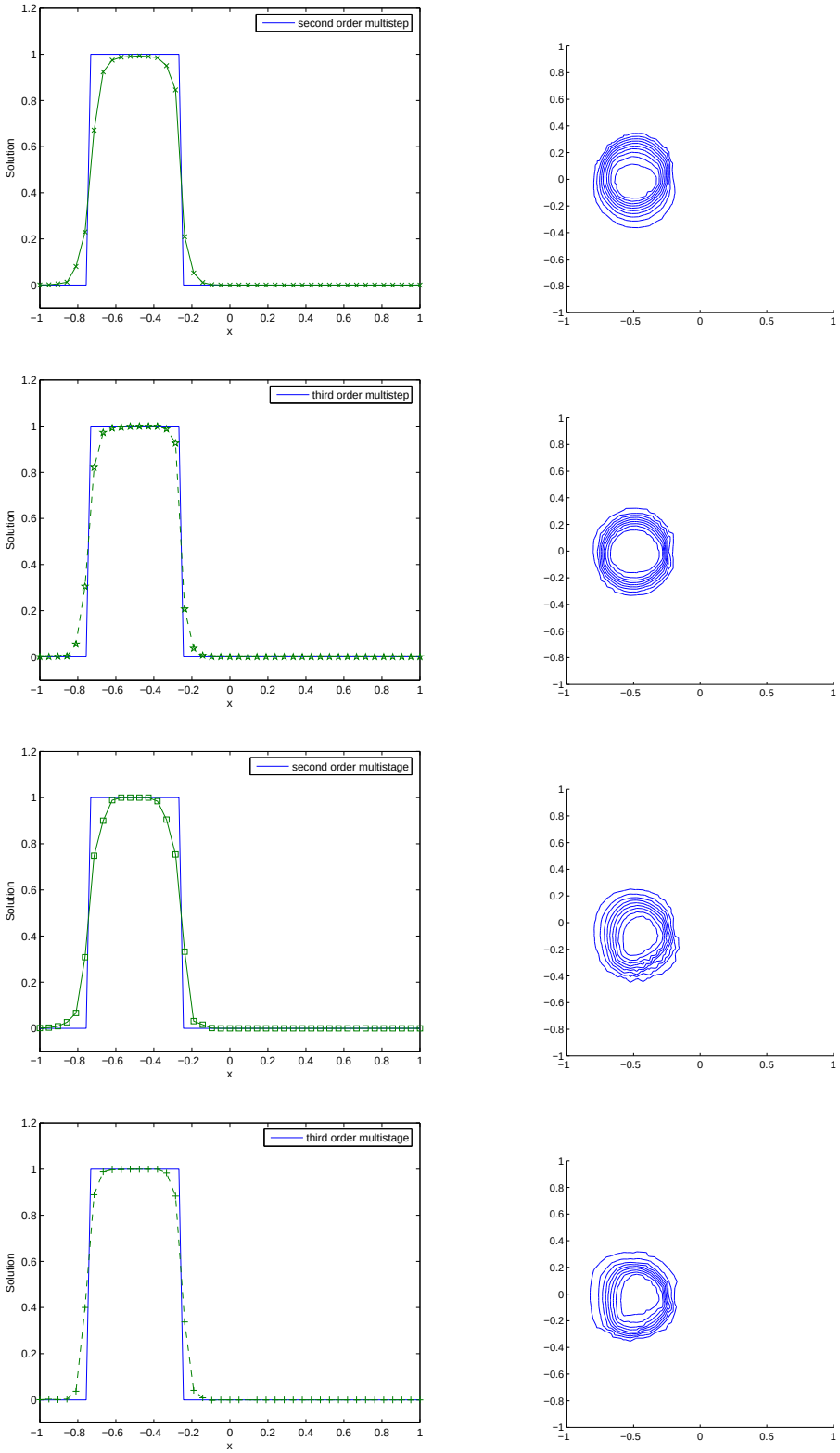

Figure 4.10: Solution for the rotating cylinder after one revolution on mesh type A, for second order multistep (top), third order multistep (second from top), second order multistage (third from top) and third order multistage (bottom), schemes. The solid line without a marker is the exact solution.

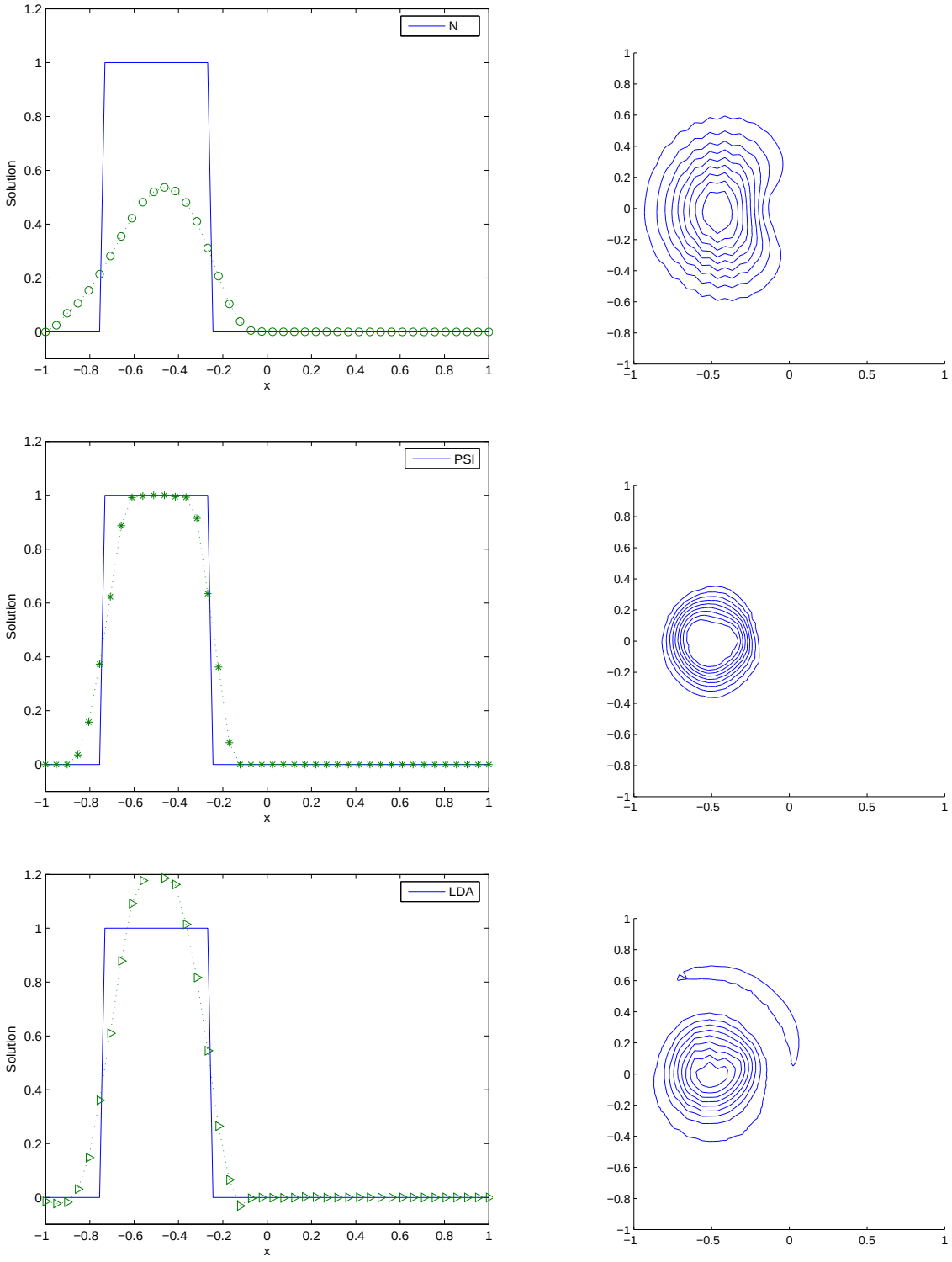

Figure 4.11: Solution for the rotating cylinder after one revolution on mesh type B, for N (top), PSI (middle) and LDA (bottom) schemes, where the solid line without a marker is the exact solution.

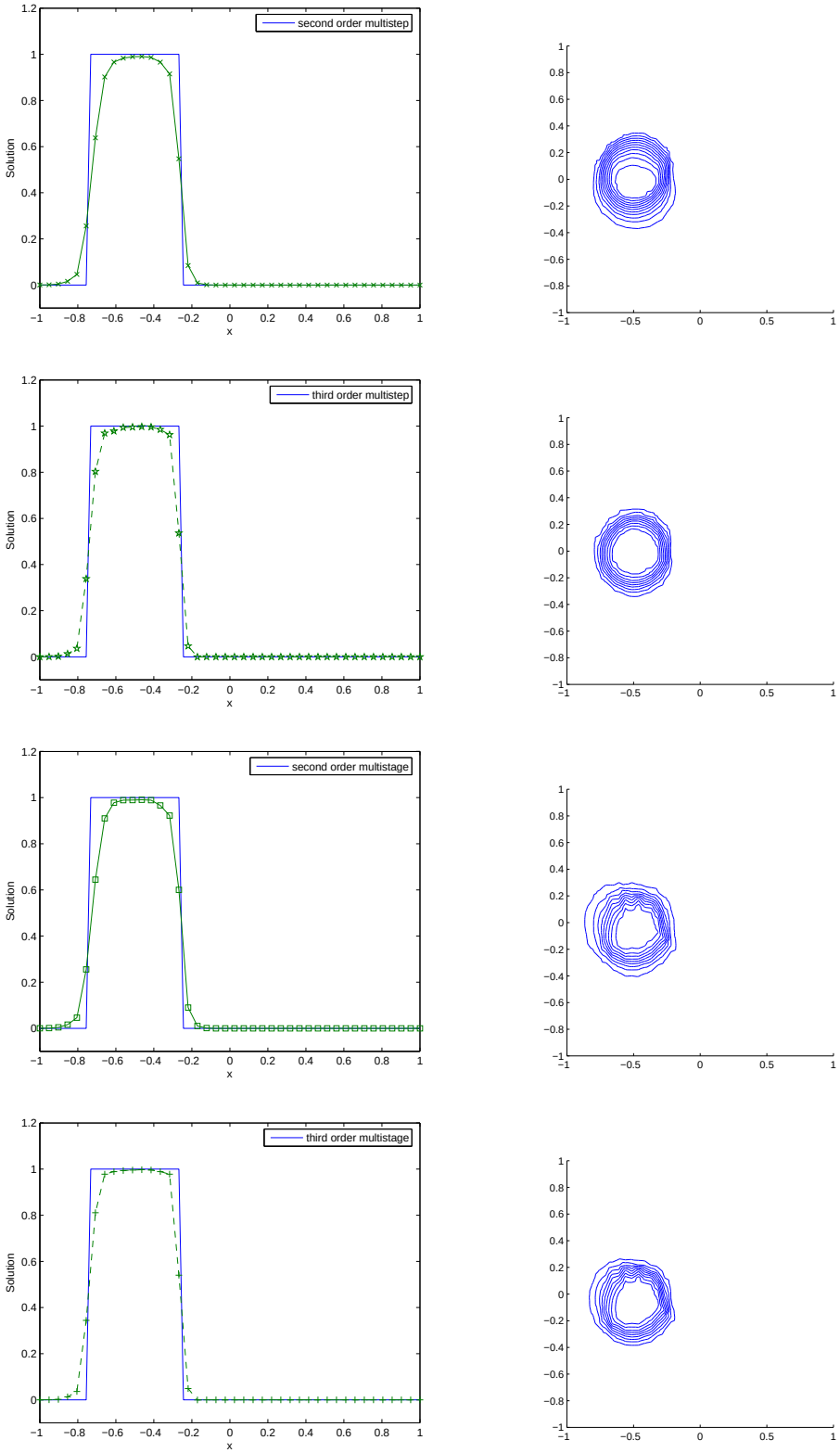

Figure 4.12: Solution for the rotating cylinder after one revolution on mesh type B, for second order multistep (top), third order multistep (second from top), second order multistage (third from top) and third order multistage (bottom), schemes. The solid line without a marker is the exact solution.

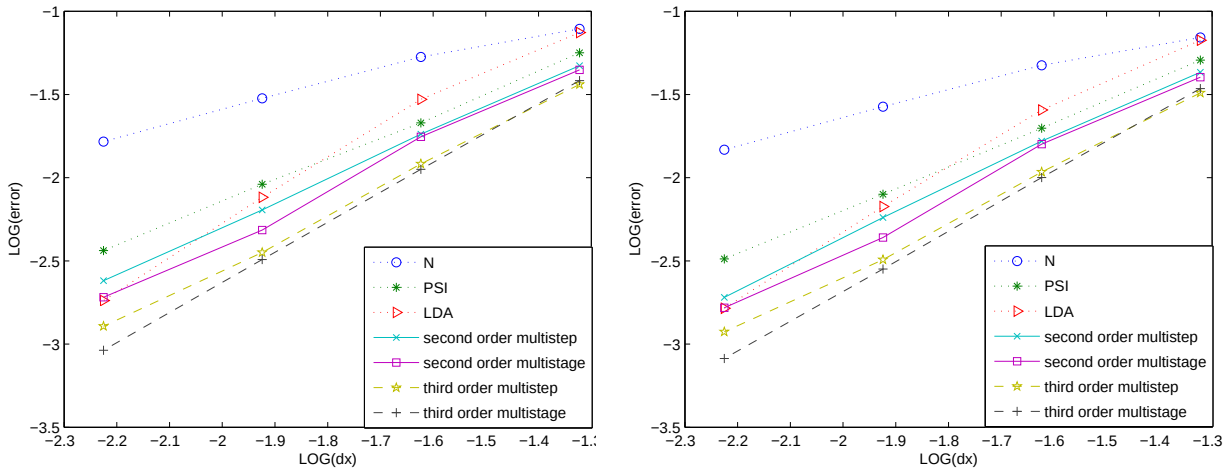

Figure 4.13: Numerical error for grid type A (top right), and for grid type B (top left) : for L_1 error.

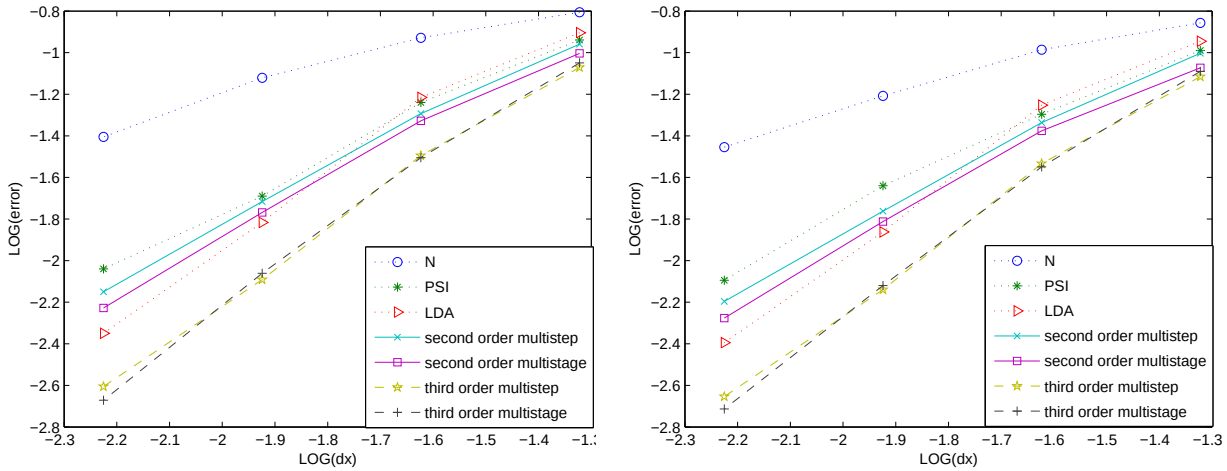

Figure 4.14: Numerical error for grid type A (top right), and for grid type B (top left) : for L_2 error.

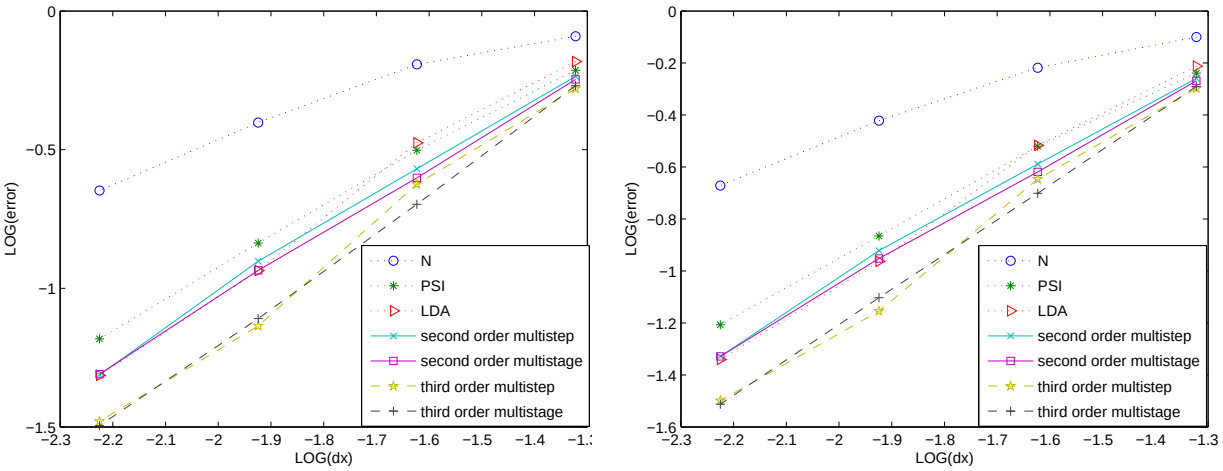

Figure 4.15: Numerical error for grid type A (top right), and for grid type B (top left) : for L_∞ error.

Chapter 5

Conclusions and Future Prospects

In this thesis the fluctuation splitting schemes which were the subject of this research have been examined and analysed in relation to their approximation of the linear advection equation and nonlinear Burgers' equation. This lays a foundation on which more complicated computational methods for complex fluid flows can be constructed. The motivational and theoretical bases for the construction of fluctuation splitting schemes were also outlined in order to illustrate some of the similarities of the fluctuation splitting schemes to finite volume and finite element methods, as well as their unique features.

The fluctuation splitting schemes that were considered for approximating the advection equation and Burgers' equation were analysed in the context of various properties. The first order accurate N scheme, also used in the distribution of the limited fluctuation of the positive high order fluctuation splitting schemes, is positive but also has a clear dissipative character. The non-positive linearity preserving LDA scheme, which was also used to distribute the fluctuation resulting from higher order interpolants for the construction of high order fluctuation splitting schemes at the price of spurious oscillation, was also outlined in Chapter 2. The PSI scheme was designed to satisfy all the properties defined in Chapter 2 and illustrated that a positive and linearity preserving property can be obtained by simply limiting the distribution coefficients of the N scheme.

The construction of fluctuation splitting schemes which have higher that second order accuracy was outlined in Chapter 3. However, it was shown that none of the high order schemes was inherently positive, and that it is impossible to guarantee positivity when the fluctuation corresponding to higher degree polynomial representation in a grid cell

is constrained so that it can only be distributed to its vertices. These findings led to the development of a technique which can impose positivity on any high order fluctuation splitting scheme.

It was then shown that applying a limiting procedure to all the high order schemes clearly removes the oscillations that were present, and this higher than second order accurate and positive fluctuation splitting scheme can be used to accurately approximate solutions of linear and nonlinear scalar conservation laws without creating any unphysical oscillations in the solution.

5.1 Achievements

In this thesis the development, examination and verification of a new form of higher than second order fluctuation splitting discretisation for the solution of steady conservation laws on unstructured grids was presented. It was shown that it is possible to develop a new type of higher than second order scheme, here called the additional neighbouring nodes (ANN) fluctuation splitting scheme, which uses information about the dependent variables stored at the neighbouring nodes in addition to the regular cell nodes. This is used to construct the polynomial interpolant of the dependent variable used to evaluate the fluctuation. Moreover, the implementation of a technique that removes unphysical oscillations (devised by Hubbard [41]) as part of the additional neighbouring nodes scheme was also shown. This achieves a positive and linearity preserving higher than second order fluctuation splitting scheme.

The performance of the new ANN PSI scheme was tested extensively, confirming that the scheme was positive and higher than second order accurate. The results for the advection test problems presented in Section 3.7 clearly showed that the modified ANN PSI scheme yields quite accurate and oscillation-free results, clearly implying that the scheme guarantees the positivity property. These results also verified that the positive very high order fluctuation splitting schemes presented in this thesis improve on the well-established second order PSI scheme in terms of accuracy, as the very high order schemes are able to reduce the unphysical errors due to the high accuracy of the schemes compensating for the more complicated operations needed to obtain the very high order approximation. The overall advantages of using the ANN fluctuation splitting scheme compared to the existing high order schemes were also outlined, as ANN scheme requires less storage over submesh reconstruction (Abgrall-Roe scheme) while it avoids the complexity involved in approximating solution gradients (Caraeni's scheme) to higher order accuracy on unstructured grids or highly distorted grids. Overall, like the existing high order schemes,

the ANN PSI scheme shows its effectiveness at removing unwanted oscillations without unduly affecting the underlying schemes accuracy.

A second original contribution was the construction of a multistage high order (in space *and* time) fluctuation splitting scheme for two-dimensional unsteady scalar advection on triangular meshes. This clearly demonstrated that high order accuracy can be achieved in both space and time.

A multistep high order (in space *and* time) fluctuation splitting scheme which is similar in philosophy to the multistage high order scheme, for the approximation of time-dependent hyperbolic conservation laws, was also presented. This was compared with the multistage high order method. From the numerical tests conducted on the various space-time low order fluctuation splitting schemes and the high-order space-time fluctuation splitting schemes, it is clearly evident that the high order space-time fluctuation splitting schemes produce consistently more accurate results. The accuracy comparison of the multistage high-order fluctuation splitting scheme to that of multistep high order fluctuation splitting scheme has illustrated that a slightly more accurate solution with better peak preservation can be achieved using the multistage method, as discussed in Section 4.10. Another advantage is that the multistage fluctuation splitting scheme does not require the storage of additional information at previous time levels, compared to the multistep fluctuation splitting scheme.

5.2 Future Prospects

There is plenty of further research to complete regarding the new developments presented in this thesis. The positive high order fluctuation splitting schemes have opened up various research avenues which should be further explored, and successfully addressing them will have a positive impact to this research area.

1. The new positive ANN fluctuation splitting scheme still requires an optimised way of choosing the appropriate nodes needed to construct the polynomial interpolant of the dependent variables for each grid cell, particularly for constructing a scheme which is higher than third order accurate.

2. The new positive ANN fluctuation splitting scheme needs to be applied to nonlinear systems of conservation laws, e.g. the Euler or shallow water equations. Because of the way the limiting procedure is constructed, there is a possibility of considering the fluctuation as contributions due to the linear variation and a high order correction (written as a difference). This difference can be treated in a similar manner to

the difference which occurs in flux difference splitting. This gives a fully conservative linearised form for the fluctuation within each grid cell. This fluctuation can then be distributed to the appropriate vertices of the cell as usual. However, one needs to bear in mind the complexity involved when dealing with a system of nonlinear conservation laws, as none of the nonlinear positive higher than second order schemes has yet been successfully applied to nonlinear systems of conservation laws.

3. The positive high order fluctuation splitting schemes can be extended to space-time fluctuation distribution, for imposing positivity on the time-dependent problems. Recent unpublished research conducted by Hubbard has shown that the limiting procedure can also be used to construct a fully consistent, positive, high order fluctuation splitting scheme for time-dependent situations. This extension could be applied in a similar manner to that of the ANN PSI scheme.

4. There are also areas the new positive high order fluctuation splitting schemes can be applied to, such as the dispersive third derivative terms which appear in the KdV equation and Boussinesq models of shallow water flow.

5.3 Applications

There are a multitude of interesting application areas for the high order fluctuation splitting schemes presented in this thesis. The simulation of flows using shallow water equations, such as flow through channels/rivers and around coastal structures is one particular interest. Simulation of realistic coastal engineering problems will require the discretisation of additional source terms, such as those modelling bed friction, variable topography, and a method for handling dry areas. However, difficulties arise in the discretisation of these source terms, which should be carried out in a manner which doesn't disturb the balance with the flux terms, and in the approximation of moving interface between wet and dry regions of the domain. In all cases the additional study of properties of nonlinear limited fluctuation splitting discretisation will be very beneficial.

Another very interesting application area is meteorology, where a shallow water model is often used as a first approximation to horizontal global atmospheric dynamics. Moreover, in order to model chemical transport, schemes which are accurate and efficient are continually being sought. However, the main challenge is applying the new methods to atmospheric models on the sphere. A method of approximating the scalar advection equation in curvilinear coordinate system would be sought first, which would then be extended

to the shallow water equations.

Bibliography

[1] R. Abgrall and T. J. Barth. Residual distributive schemes for conservation laws via adaptive quadrature. *J. Sci. Comp.*, 167(2):277-315, 2001.

[2] R. Abgrall, K. Mer. A Lax-Wendroff type theorem for residual schemes. *Innovative methods for numerical solutions of partial differential equations, World Scientific*, 243-266, 2002.

[3] R. Abgrall, N. Andrianov and M. Mezine. Toward very high order accurate schemes for unsteady convection problems on unstructured meshes. *Int. J. Numer. Meth. Fluids*, 47:679-691, 2004.

[4] R. Abgrall and M. Mezine. Construction of second order accurate monotone and stable residual distributive schemes: The steady case. *J. Comput. Phys.*, 195:474-507, 2004

[5] R. Abgrall and M. Mezine. Residual distributive schemes for steady problems. In *VKI LS 2003-05, Computational Fluid Dynamics*, 2003.

[6] R. Abgrall and M. Mezine. Construction of second order accurate monotone and stable residual distributive schemes: The unsteady case. *J. Comput. Phys.*, 188(1):16-55, 2003.

[7] R. Abgrall and M. Mezine. A consistent upwind residual scheme for scalar unsteady advection problems. Conference AMIF, Tuscany, Italy, 2000.

[8] R. Abgrall and P. L. Roe. High order fluctuation schemes on triangular meshes. *J. Sci. Comp.*, 19(3):3-36,2003.

[9] R. Abgrall. Toward the ultimate conservative scheme: Following the quest. *J. Comput. Phys.*, 169(2):277-315, 2001.

[10] R. Abgrall. Construction of high order residual distributive schemes for scalar problems. In *VKI LS 2006-01, Computational Fluid Dynamics*, 2006.

[11] T. J. Barth. Numerical methods for conservation laws on structured and unstructured meshes. In *VKI LS 2003-05, Computational Fluid Dynamics*, 2003.

[12] T. J. Barth. Aspects of unstructured grids and finite volume solvers for the Euler and Navier-Stokes equations. In *VKI LS 1994-05, Computational Fluid Dynamics*, 1994.

[13] T. J. Barth and H.Deconinck. High-order ENO and WENO schemes for computational fluid dynamics . Lecture Notes in Computational Science and Engineering, Volume 9, Springer-Verlag, Heidelberg, 1999.

[14] T. J. Barth and H.Deconinck. Error estimation and adaptive discretization methods in CFD. Lecture Notes in Computational Science and Engineering, Volume 25, Springer-Verlag, Heidelberg, 2003.

[15] T. J. Barth and D. C. Jespersen. The design and application of upwind schemes on unstructured meshes. AIAA paper 89-0355, 27th AIAA Aerospace Sciences Meeting, Reno, Nevada, 1989.

[16] T. J. Barth and M. Ohlberger. Finite volume methods: foundation and analysis. *Encyclopedia of Computational Mechanics*, John Wiley & Sons, Ltd., 2004.

[17] D. Caraeni and L. Fuchs. Compact third-order multidimensional upwind scheme for Navier Stokes simulations. In: Theoretical and Computational Fluid Dynamics, 15:373-401, 2002.

[18] D. Caraeni and L. Fuchs. A new compact high-order multidimensional upwind discretization. 4th CSCC conference, Vouliagmeni, Greece, July 2000.

[19] D. Caraeni and L. Fuchs. LES using a parallel multidimensional upwind solver. ICCFD, Kyoto, Japan, July 2000.

[20] D. Caraeni, M. Caraeni and L. Fuchs. A parallel multidimensional upwind algorithm for LES. AIAA paper 2001-2547, 15th AIAA Computational Fluid Dynamics Conference, Anaheim, 2001.

[21] D. Caraeni. A third order residual distribution method for steady/unsteady simulations: Formulation and 2D/3D benchmarking. In *VKI LS 2006-01, Computational Fluid Dynamics*, November, 2005.

[22] J. C. Carette, H. Deconinck, H. Paillère and P. L. Roe. Multidimensional upwinding: its relation to finite elements. *Int. J. Numer. Met. Fluids.*, 20:935-955, 1995.

[23] B. Cockburn. Discontinuous Galerkin methods for convection-dominated problems. Volume 9 of Lecture Notes in Computational Science and Engineering, pp. 69-224, Springer-Verlag, Heidelberg, 1999.

[24] À. Csìk and H. Deconinck. Space time residual distribution schemes for hyperbolic conservation laws on unstructured linear finite elements. In M.J. Baines, editor. ICFD Conference on Numerical Methods for Fluid Dynamics VII, pp. 557-564, Oxford, 2001.

[25] À. Csìk, H. Deconinck and S.Poedts. Performance comparison of multidimensional upwind residual distribution and dimensionally split finite volume Roe schemes on the steady solution of conservation laws. *Finite Volumes for Complex Applications III*, HERMES Science Publishing Ltd., 2002.

[26] À. Csìk, M.Ricchiuto and H. Deconinck. Space-time residual distribution schemes for hyperbolic conservation laws over linear and bilinear elements. In *VKI LS 2003-05, Computational Fluid Dynamics*, 2003.

[27] H. Deconinck and R. Abgrall. Introduction to residual distribution methods. In *VKI LS 2006-01, Computational Fluid Dynamics*, November, 2005.

[28] H. Deconinck and G. Degrez. Multidimensional upwind residual distribution schemes and applications. Finite Volumes for Complex Applications II. Hermes Science Publications, Paris, 1999.

[29] H. Deconinck and B. Koren. Euler and Navier-Stokes solvers using multidimensional upwind schemes and multigrid acceleration. Notes on Numerical Fluid Mechanics, Volume 57, Vieweg, 1997.

[30] H. Deconinck and K. Sermeus. Status of multidimensional upwind residual distribution schemes and application in aeronautics. Fluids 2000, Denver, USA, June 19-22, 2000 AIAA 2000-2328.

[31] H. Deconinck, R. Struijs, G. Bourgeois, P. Roe. Compact advection schemes on unstructured meshes. In *VKI LS 1993-04, Computational Fluid Dynamics*, 1993.

[32] H. Deconinck, R. Struijs, G. Bourgois and P. L. Roe. High resolution shock capturing cell vertex advection schemes on unstructured grids. In *VKI LS 1994-05, Computational Fluid Dynamics*, March, 1994.

[33] H. Deconinck, R. Struijs, and P. L. Roe. Compact advection scheme on unstructured grids. In *VKI LS 1993-04, Computational Fluid Dynamics*, 1993.

[34] H. Deconinck, M. Ricchiuto and K. Sermeus. Introduction to residual distribution schemes and stabilised finite elements. In *VKI LS 2003-05, Computational Fluid Dynamics*, 2003.

[35] G. Degrez and E. van der Weide. Upwind residual distribution schemes for chemical non-equilibrium flows, Norfolk, USA, 14th AIAA Computational Fluid Dynamics Conference, June 28- July 1, 1999.

[36] A. C. Galeao and E. G. Dutra do Carmo. A consistent approximation upwind Petrov-Galerkin method for convection dominated problems. *Comp. Meth. Appl. Mech. Engrg.*, 68:134-152, 1989.

[37] A. Godlewski and P. Raviart. Hyperbolic systems of conservation laws. Applied Mathematical Sciences, Springer-Verlag, 1995.

[38] S. K. Godunov. A finite difference method for the numerical computation of discontinuous solutions of the equations of fluid dynamics. *Mat. Sb.*, 47, pp. 271-306, 1959.

[39] G. H. Golub and C. F. van Loan. Matrix Computations, John Hopkins University Press, Baltimore, Maryland, 1983.

[40] C. Hirsch. Numerical computation of internal and external flows, Wiley-Interscience, 1989.

[41] M. E. Hubbard. Non-oscillatory third order fluctuation splitting schemes for steady scalar conservation laws. *J. Comput. Phys.*, 222(2):740-768, 2007.

[42] M. E. Hubbard. Non-oscillatory third order fluctuation splitting schemes, Finite Volumes for Complex Applications IV, pp 377-387, 2005

[43] M. E. Hubbard and M. J. Baines. Conservative multidimensional upwinding for steady two-dimensional shallow-water equation. *J. Comput. Phys.*, 138(1):419-448, 1997.

[44] M. E. Hubbard and A. L. Laird. Achieving high-order fluctuation splitting schemes by extending the stencil. *Comput. Fluids*, 34:443-459, 2005.

[45] M. E. Hubbard. Multidimensional upwind fluctuation distribution schemes for scalar time dependent problems. Project report, University of Reading, 1998

[46] M. E. Hubbard. Multidimensional upwinding and grid adaptation for conservation laws. PhD thesis, University of Reading, February 1996.

[47] T. J. R. Hughes and A. Brook. Streamline upwind Petrov-Galerkin formulations for convection dominated flows with particular emphasis on the incompressible Navier-Stokes equations. *Comp. Meth. Appl. Mech. Engrg.*, 32:199-259, 1982.

[48] T. J. R. Hughes and M. Mallet. A new finite element formulation for CFD: the generalised streamline operator for multidimensional advective-diffusive systems. *Comp. Meth. Appl. Mech. Engrg.*, 58:305-328, 1986.

[49] T. J. R. Hughes and M. Mallet. A new finite element formulation for CFD: a discontinuity-capturing operator for multidimensional advective-diffusive systems. *Comp. Meth. Appl. Mech. Engrg.*, 58:329-336, 1986.

[50] T. J. R. Hughes, M. Mallet and A. Mizukami. A new finite element formulation for CFD: beyond SUPG. *Comp. Meth. Appl. Mech. Engrg.*, 54:341-355,1986.

[51] A. Jameson. Time dependent calculations using multigrid with applications to unsteady flows past airfoils and wings. AIAA paper 91-1596, 1991.

[52] C. Johnson. Numerical solution of partial differential equations by the finite element method, Cambridge University Press, Cambridge, 1987.

[53] R. J. Leveque. Wave propagation algorithms for multi-dimensional hyperbolic systems. *J. Comput. Phys.*, 131:327-353, 1997.

[54] R. J. Leveque. Finite volume methods for hyperbolic problems, Cambridge University Press, 2002.

[55] R. J. Leveque. Numerical methods for conservation laws. Birkhäuser, 1992.

[56] J. Maerz and G. Degrez. Improving time accuracy for residual distribution schemes. Technical Report VKI-PR 96-17, June, 1996.

[57] M. Mezine and R. Abgrall. Upwind multidimensional residual schemes for steady and unsteady flows. In ICCFD2, pp. 165-170, Sydney, Australia, July 2002.

[58] M. Mezine, M.Ricchiuto, H.Deconinck and R. Abgrall. Monotone and stable residual distribution schemes on prismatic space-time elements for unsteady conservation laws. In *VKI LS 2003-05, Computational Fluid Dynamics*, 2003.

[59] R. H. Ni. A multiple grid scheme for solving the Euler equations. AIAA Journal, 20:1565-1571, 1981.

[60] H. Nishikawa, M. Rad, and P. Roe. A third-order fluctuation splitting scheme that preserves potential flow. AIAA paper 2001-2595, 15th AIAA Computational Fluid Dynamics Conference, Anaheim, 2001.

[61] H. Paillère, H. Deconinck, R. Struijs, P. L. Roe, L. M. Mesaros and J. D. Muller. Computations of inviscid compressible flows using fluctuation splitting on triangular meshes. AIAA paper 93-3301, 1993.

[62] H.Paillère. Multidimensional upwind residual discretization schemes for the Euler and Navier-Stokes equation on unstructured meshes. PhD thesis, Universit*acutee* Libre de Bruxelles, 1995.

[63] H.Paillère, J. C. Carette and H. Deconinck. Multidimensional upwind and SUPG methods for the solution of the compressible flow equations on unstructured grids. In *VKI LS 1994-05, Computational Fluid Dynamics*, 1995.

[64] H. Paillère, H. Deconinck and E. van der Wiede. Upwind residual distribution methods for compressible flow: an alternative to finite volume and finite element methods. In *VKI LS 1997-02, Computational Fluid Dynamics*, 1997.

[65] H. Paillère, E. van der Wiede and H. Deconinck. Multidimensional upwind methods for inviscid and viscous compressible flow. In *VKI LS 1995-02, Computational Fluid Dynamics*, 1995.

[66] H. Paillère and H. Deconinck. Compact cell-vertex convection schemes on unstructured meshes. *Int. J. Numer. Meth. Fluids*, 57:1-49, 1997.

[67] M. Ricchiuto, R. Abgrall, and H. Deconinck. Construction of very high order residual distribution schemes for unsteady advection: preliminary result. VKI LS 2003-05, 33^{rd} Computational Fluid Dynamics, Von Karman Institute for Fluid Dynamics, 2003.

[68] M. Ricchiuto, À. Csìk, and H. Deconinck, Residual distribution for general time-dependent conservation laws. *J. Comput. Phys.*, 209:249-289, 2005.

[69] P. L. Roe and D. Sidilkover. Optimum positive linear schemes for advection in two and three dimensions, *SIAM J. Numer. Anal.*, 29(6), 1542-1568, 1992.

[70] P. L. Roe. Approximate Riemann solvers, parameter vectors, and difference schemes. *J. Comput. Phys.*, 43:357-372, 1981.

[71] P. L. Roe. Linear advection schemes on triangular meshes. Technical Report CoA 8720, Cranfield Institute of Technology, 1987.

[72] P. L. Roe. A basis for upwind differencing of the two-dimensional unsteady Eurer equation. In K.W.Morton and M.J.Baines, editors, Numerical Methods for Fluid Dynamics, pages 55-80. Academic Press, 1986.

[73] P. L. Roe. "Optimum" upwind advection on a triangular mesh. Technical Report, ICASE, NASA Langley R.C.,1990.

[74] P. L. Roe. Discretizations that exploit the structure of the governing equations. VKI LS 2006-01, 33^{rd} Computational Fluid Dynamics course, Von Karman Institute for Fluid Dynamics, 2005.

[75] P. L. Roe. Fluctuation and signals - a framework for numerical evolution problems. In K.W.Morton and M.J.Baines, editors, Numerical Methods for Fluid Dynamics, pp. 219-257. Academic Press, 1982.

[76] B. Szabo. Introduction to finite element analysis. John Wiley and Sons, Inc, 1989.

[77] C. Shu. Essentially non-oscillatory and weighted essentially non-oscillatory schemes for hyperbolic conservation laws. Advanced Numerical Approximation of Nonlinear Hyperbolic Equations, Volume 1697, pages 325-432. Springer-Verlag, Heidelberg, 1998.

[78] C. Shu. High order methods for computational physics. In T.J.Barth and H.Deconinck, editors. Lecture Notes in Computational Science and Engineering, Volume 9, pages 439-582. Springer-Verlag, Heidelberg, 1999.

[79] C. Shu and S. Osher. Efficient implementation of essentially non-oscillatory shock-capturing schemes. *J. Comput. Phys.*, 77:439-471, 1988.

[80] E. van der Weide and H. Deconinck. Positive matrix distribution schemes for hyperbolic systems. In *Computational Fluid Dynamics*, pages, 747-753, Wiley, 1996.

[81] E. van der Weide. Compressible flow simulation on unstructured grids using multi-dimensional upwind schemes. PhD thesis, Delft University of Technology, Netherlands, November 12, 1998.

[82] N. Villedieu, M. Ricchiuto, and H. Deconinck. Study of a 3^{rd} order residual distributive scheme for advection-diffusion equations. In *VKI PR 04-24, Computational Fluid Dynamics*, 2004.

[83] B. van Leer. Progress in multidimensional upwinding. Tech. Rep. 92-43, ICASE, 1992.

[84] W. A. Wood and W. L. Kleb. Diffusion characteristics of finite volume and fluctuation splitting schemes. *J. Comput. Phys.*, 153:353-377, 1999.

[85] W. H. Press, S. A. Teukolsky, W. T. Vetterling and B. P. Flannery. Numerical Recipes in Fortran 77. Press Syndicate of the University of Cambridge, second edition, 1996.